Leveraging Nanomaterials for Measurements at the Quantum Limit

by

Jan Bartos

B.S., Rensselaer Polytechnic Institute, 2018

M.S., University of Colorado, Boulder, 2022

A thesis submitted to the

Faculty of the Graduate School of the

University of Colorado in partial fulfillment

of the requirements for the degree of

Doctor of Philosophy

Department of Electrical, Computer, and Energy Engineering

2025

Committee Members:

Shu-Wei Huang, Chair

Wounjhang Park

Robert McLeod

Greg Rieker

Samuel Oberdick

Bartos, Jan (Ph.D., Electrical Engineering)

Leveraging Nanomaterials for Measurements at the Quantum Limit

Thesis directed by Prof. Shu-Wei Huang

This dissertation reports on sensing enhancements enabled by nanomaterials, focusing on two areas: magnetic field sensing and imaging, and fluorescence microscopy. In both domains, we find that nanomaterials lead to sensors which outperform bulk and microscale materials.

Motivating the magnetic field sensing project, we observed that most existing magnetic field sensing techniques follow a trend where their magnetic field sensitivity is inversely proportional to sensor volume. This presents a challenge when attempting to perform high-sensitivity, spatially resolved magnetic field measurements.

The primary research question investigates whether this paradigm could be broken. Because the sensitivity of Faraday rotation magnetometry (FRM) depends on optical power rather than intensity, magnetic field sensitivity to be decoupled from spot size.

To leverage this benefit, two key improvements were required. First, we developed a new material to enhance sensitivity potential. Second, we optimized the sensing architecture to maximize performance using this newly developed transducer.

We discovered that a nanocomposite of terbium-doped magnetite nanoparticles embedded in a polymer host produced an extremely high Verdet constant while maintaining good optical clarity. However, the material exhibited a low optical damage threshold, which limited performance when tightly focused optical spots were used. Since magnetic field sensitivity can be improved by increasing optical power, this low optical damage threshold posed a problem.

To address this issue, we employed a non-common path heterodyne detection scheme. This approach allowed most of the light to bypass the sample, reducing illumination power while mixing the beams on the detector. This amplified the signal above the electronic noise floor, enabling shot-noise-limited measurements even with low optical illumination power. Using this method, we

achieved a sensitivity of 568 nT/$\sqrt{\text{Hz}}$ in our magnetometer.

Further exploration, inspired by polarization-sensitive optical coherence tomography, led us to propose an alternative and novel detection architecture called dual-balanced heterodyne detection (DBHD). This approach altered the power scaling of the measurement, providing additional signal amplification at low magnetic fields. This technique initially had potential to achieve pT/Hz sensitivity. A proof-of-concept device was implemented to validate the hypothesis. However, after extensive experimental work, I concluded that the sensitivity potential was not realizable due to nonlinear scaling of the noise. Though we explore some potential advantages of the technique.

The final part of this dissertation investigates the use of upconversion nanoparticles (UCNPs). These particles are employed in fluorescence microscopy, an imaging technique commonly used in biology to stain samples. UCNPs convert two low-energy photons into one higher-energy photon, enabling background-free measurements because the illumination light differs from the detection light. However, UCNPs are limited by their low photon absorption probability.

We hypothesized that the brightness of UCNPs could be increased using paired photons to enable instantaneous upconversion attempts. A rate-equation model was developed to simulate the dynamics of the nanoparticles. We found that the threshold for brightness enhancement between biphoton and conventional illumination depends on the lifetime of singly excited electrons. In our material, this lifetime is on the order of milliseconds. The threshold for enhancement was so low that it would produce fewer than one photon per second, rendering experimental pursuit impractical.

In summary, this dissertation examines two different systems, both with imaging applications, that leverage the properties of nanoparticles to enhance sensing. The magnetite nanoparticles enabled highly sensitive measurements when combined with a novel detection configuration. Meanwhile, the UCNP nanoparticles proved too efficient to justify the use of paired photon sources for illumination, as their performance could not be practically enhanced.

Dedication

I dedicate this thesis to my parents, for their unwavering love, support, and encouragement.

Acknowledgements

Graduate school has been the single greatest challenge of my life. It pushed me, exposed my weaknesses, and forced me to deal with failure while striving to improve the understanding of the world around us.

Such a challenge could not have been accomplished alone, and I would like to take this opportunity to thank those who supported me throughout this journey. First, I would like to thank my advisor, Shu-Wei. I could always count on you to provide clarity and guidance when everything felt uncertain. Next, I would like to thank my close collaborators over the years: Taleb Ba Tis, Conrad Corbella Bagot, Eric Rappeport, Jon Musgrave, and Bright Lu, for being wonderful scientists and friends to work with. I also want to thank all past and current members of the ultrafast photonics research group for their insightful conversations and technical support.

Looking outside of CU, I want to extend my deepest gratitude to everyone I had the privilege of sharing the outdoors with during graduate school—whether through running, skiing, or biking—while exploring our wonderful state.

I would also like to take a moment to express my appreciation to my Mom, Dad, and Brother for your love and support, even when I was stressed and working too much. You always had my back.

Lastly, I want to thank my partner, Liz, for your support, technical knowledge, and patience throughout my PhD. It is one of my greatest pleasures to not only share science with you but also to share our love for adventure.

Contents

Chapter

Tables

Table

Figures

Figure

Chapter 1

Introduction

During my time at the University of Colorado, Boulder, I have focused on enhancing measurement tools, specifically microscopes. My aim has been to make more sensitive measurements, enabling the detection of weaker signals and facilitating faster measurements. My research has centered on two discrete projects: magnetic field imaging and upconversion fluorescence microscopy. In both projects, nanoparticles serve as indicators for quantities of interest, measuring the magnetic field in the first case and converting probe light to a different wavelength for reduced-noise images in second case. These nanomaterials enable us to make more sensitive measurements compared to bulk or microscopic materials as their response to external factors is enhanced by the particle size. Yet, such materials are only recently being considered for measurements since they can be hard to fabricate, characterize, and work with. In this thesis, I show how nanoparticles can be leveraged in measurements which do not compromise imaging resolution for sensitivity in two different contexts. The work presented in this thesis is highly multidisciplinary, integrating elements of material science, physical chemistry, and optical and electrical engineering to make both diffraction and shot noise limited measurements. In other words, these measurements approach the classical limits for both the resolution and sensitivity, respectively. Broadly speaking this work falls under the umbrella of metrology.

1.1 Metrology

This dissertation is a multidisciplinary blend of physics and engineering, with a focus on metrology, the science of measurement. Metrology is intriguing because one rarely measures the desired quantity directly; instead, one often measures related quantities, such as voltage, which serve as an abstraction of what one aims to determine. Achieving accurate and consistent measurements requires careful calibration and thoughtful experimental design. Entire industries are built around metrology, including the National Institute of Standards and Technology (NIST), a key agency of the U.S. government dedicated to maintaining measurement standards.

In our case, for magnetic field sensing, though we want to measure magnetic field strength, we are actually measuring electrical power from a photodetector which is in turn produced by optical power, which is indirectly a function of the magnetic field. For fluorescence microscopy, the dyes serve as labels for specific biological components such as cells, thus enabling the quantification of biological processes such as disease.

Spatially resolved images have pixels whose value (or values) correspond to the quantity of interest at that location. In the case of magnetic field imaging, each pixel carries a measurement of the magnetic field strength. These measurements come from optically probing nanoparticles which increasingly rotate the polarization of the probe beam with increasing magnetic field strength. Changes in the light's polarization correspond directly to the magnetic field at the probe site. In the case of up-conversion fluorescence microscopy, each pixel carries a measurement of the concentration of nanoparticles within it. These measurements come from contrast agents which convert infrared probe light into visible fluoresced light. Since the probe wavelength is different from the detected wavelength, the two can be easily separated and the resulting image is of high quality without illumination light contamination. The size of the pixels relates directly to the diffraction limit which dictates, given the optical system design and the wavelength of the probe beam. Thus, achieving the diffraction limit can be accomplished through careful optical design and lens selection. Once these parameters are set, an image can be acquired by moving the sample

relative to the probe beam and measuring different pixels one-by-one.

The fidelity of a measurement within a pixel is referred to as its sensitivity. The fundamental limit of sensitivity as measured in the signal-to-noise ratio (SNR) is given by the shot noise of the measurement. Shot noise represents the classical limit for sensitivity that arises from quantization statistics of both electrons and photons. This noise is the quantum limit of sensitivity and cannot be beaten except through use of exotic light sources. We use nanoparticles to make it easier to get to the shot noise limit as well as increasing the response of measurements that are already shot noise limited.

1.2 Motivation for Laser Based Sensing

In conducting highly-sensitive and high-resolution measurements, we require a tool with both high temporal and spatial stability. For this, we turn to the laser and leverage the spatial and temporal coherences of the beams it creates. Coherence refers to the fixed phase relationship between light waves, both spatially and temporally. Broadly speaking, coherence enables precision measurements in fields such as interferometry and holography, where the engineered system stability highlights minuscule changes in distance or phase. This enables interaction directly with underlying quantum effects such an electron spin. In optical communication, coherent beams of light ensure efficient information transfer by maintaining signal integrity over long distances. Added benefits that arise from coherence relate to detection strategies which minimize noise and limit signal degradation, where the signal beam can be detected directly or can be interfered with a local oscillator beam. Additionally, the tight-focusing nature of coherent light enables optical fiber communication, the backbone of the modern internet, by enabling coupling between light emitted in free space and waveguides with small modes such as optical fibers. Lasers also have applications in medical imaging, such as retina imaging via optical coherence tomography (OCT) which leverages coherence to produce high-resolution, cross-sectional images of biological tissues. Additionally, coherence plays a vital role in the emerging quantum space, where lasers are used to manipulate and probe quantum states with exceptional precision, preserving quantum information.

Imaging applications can leverage the spatial coherence which creates a tightly focused coherent laser spot. The size of the laser spot will define the spatial resolution. Since the energy of a cross-section of a beam remains constant no matter the size of the beam, a tightly focused spot can also contain locally high optical intensities. This is critical to can drive fluorescence as seen in upconversion nanoparticles and other nonlinear processes.

A key property of temporal coherence is the stability of the optical carrier frequency. This enables us to perform optical mixing and leverage the coherent gain of mixing two coherent optical beams together. This gain amplifies our signal over other noise sources bring us to the shot noise limit.

1.3 Microscopy

Microscopy, or the study of things smaller than the resolution of the naked human eye, has been a cornerstone of science since the invention of the microscope in the late 16th century. With added complexity, modern materials and fabrication techniques are increasing the performance to the current state of the art. It is important to consider a few parameters that define the performance and application for a microscope

For much of the history of microscopy, scientists have centered their work on directly imaging cells using the visible spectrum to understand life. Tools like dyes are often used to artificially enhance contrast between different structures, allowing them to be imaged and quantified. Advances in microscope resolution have enabled researchers to observe increasingly smaller structures. Exploring wavelengths beyond the visible spectrum has opened up new realms of imaging possibilities.

The imaging in this dissertation primarily employs a confocal technique. Instead of using an image sensor, we use a single-point detector and scan the sample with a focused laser beam. As we will demonstrate later, this approach offers the advantage of increasing local intensity increasing the brightness of the fluorescence, as well as enhancing magnetic field sensitivity.

1.4 Limits of Sensing

Any real-life measurement will be contaminated with noise. They key challenge of this dissertation have been understanding and achieving the limits of sensitivity. The ratio between the desired signal and the noise level is known as the signal-to-noise ratio (SNR). Whereas some types of noise can be mitigated or reduced with careful engineering, optical shot noise serves as the quantum limit and cannot be overcome except through the use of exotic, non-classical light sources. In this dissertation, I will present shot noise limited measurements of magnetic fields and the work taken to achieve that level of sensitivity.

1.5 Dissertation Outline

This dissertation covers work on improving the performance of imaging magnetometers as well as modeling non-classical illumination of upconversion nanoparticles. Chapter 2 reviews critical background information surrounding the optical measurements of magnetic fields. It also provides a review of key literature preceding my work. Chapter 3 discusses the enhancement of organic thin film Faraday rotators. Chapter 4 covers a novel method of heterodyne detection of magnetically induced polarization rotation. Chapter 5 covers background and simulation work relating to non-classical illumination of upconversion nanoparticles. Chapter 6 summarizes the work of this dissertation and proposes directions for future work.

Chapter 2

Background

2.1 Road Map

This chapter provides background regarding the underlying physics and previous results found in the literature.

First, in Sec. 2.2 I cover the basic physics underlying magnetism to motivate a discussion in Sec. 2.3 about the magneto-optic Faraday effect, the magnetic field detection method I use in this work. The magneto-optic Faraday effect is one of many strategies for magnetic field detection, I review several other detection strategies and discuss their advantages and limitations in Sec. 2.4. A key reason why I chose to use Faraday rotation magnetometery because it has a sensitivity potential that is not limited by the spatial resolution, which I discuss in Sec 2.16. Next, in Sec. 2.5 I discuss magnetic field imaging. In Sec. 2.6, I review some applications and implementations of magnetic field imaging.

In Sec. 2.7, I delve into a quantitative comparison of existing magnetic field imaging techniques. I find that magnetic field sensing techniques trade sensitivity (as measured in $\mathrm{nT}/\sqrt{\mathrm{Hz}}$) for imaging resolution (as measured in μm). When comparing various techniques along these axes, I identified a gap in sensitivity and imaging resolution which I target in my magnetometer chapter.

To achieve the desired magnetic field sensitivity, we needed to make an improvement to the material that forms the sensing medium. We did so through the use of nanomaterials. Thus leveraging the unique physical, chemical, and mechanical properties. In Sec. 2.8, I describe how optical sensing benefits from interaction with this class of materials. In particular, I focus on magnetic

nanoparticles (MNPs, see Sec. 2.8.1) and upconversion nanoparticles (UCNPs, see Sec. 2.8.2).

Lastly, in Sec. 2.9 I will quickly discuss fluorescence microscopy as it applies to upconversion nanoparticles. The interaction of non-classical light sources with upconversion fluorescent nanoparticles form the last technical chapter of my thesis are tied to story of my thesis through the use of nanomaterials.

2.2 Magnetism

In attempting to create a magnetic field imaging system we first need to describe what is being measured. Magnetic fields are one of the primary physical fields. These fields can arise from moving charges or unpaired electron spins. Maxwell's equations govern their behavior and allow us to work through some key properties. We first, consider the Ampere-Maxwell Law:

$$\nabla \times B = \mu_0 \left(J + \epsilon_0 \frac{\partial E}{\partial t} \right), \tag{2.1}$$

where B is the magnetic field, μ_0 is the vacuum permeability, J is the current density, ϵ_0 is the vacuum permittivity, and E is the electric field. This law defines how an electric field produces an orthogonal magnetic field. This gives us a means to generate magnetic fields by using current passing thought a coil of wire known as a solenoid. This law also hints at why measuring magnetic fields is interesting for imaging applications. The magnetic field depends on the vacuum permeability μ_0, which is a physical constant of vacuum. When considering magnetic fields within a material, we need to consider the material permeability μ. Critically, in non-magnetic materials (glasses, polymers, tissue, and some metals), $\mu_0 = \mu$. This means that magnetic fields are not diverted or scattered by interactions with non-magnetic materials. The same cannot be said for the physical constant that governs electric fields ϵ_0. ϵ_0 is highly dependent on material properties and will create scattering and attenuation in those same materials that did not impact the magnetic field. Magnetic fields have the potential for operating in environments where where electric field cannot. This has already been leveraged by current technologies such as MRI which conveniently avoids

the scattering properties of tissue by measuring the magnetic fields [2]. Next, considering Gauss's law of magnetism:

$$\nabla \cdot B = 0. \tag{2.2}$$

The law states that the divergence of any magnetic field is zero. This has the implication that magnetic field lines must form closed loops as seen in Fig. 2.1(a). This has the implication for magnetic field imaging because each magnet will have a region of positive and negative field. This is show in Fig. 2.1(b). Each labeled cell has a red (positive), and a blue (negative) region. This unique impulse response increases measurement confidence with imaging, with the potential for performing super resolution techniques [3].

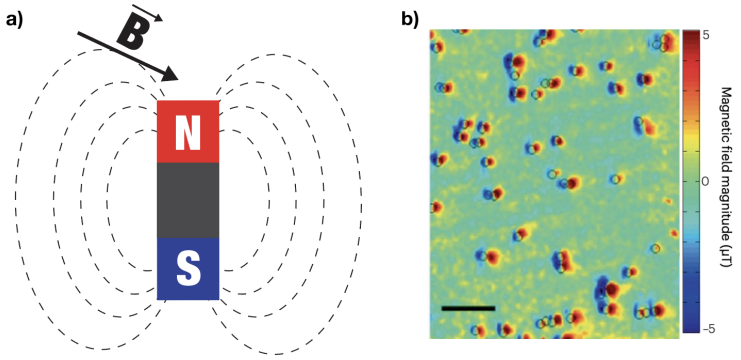

Figure 2.1: a) Magnetic field induced by a permanent magnet. b) Example magnetic field imaging demonstrating unique impulse response of magnetic fields, modified from [4]

2.2.1 Electron Spins

Maxwell's laws explain how moving charges produce magnetic fields as well as the formation of permanent magnetic fields. To fully understand the concept we need to introduce the concept of electron spin. I will provide an intuitive description as that is all that is needed to understand interactions presented in this dissertation. A mathematically rigorous description can be found in any physics textbook. From our simplified perspective, electrons can be considered as little magnets orbiting an atomic nucleus as seen in Fig. 2.2. In non-magnetic materials, each electron orbital can

be occupied by two electrons of opposite spin. This dynamic is governed by the Pauli exclusion principle. When the electrons in an orbital are paired there is no net magnetic moment $\vec{m}$ A net magnetic moment is created in certain materials, such as iron that have many unpaired electrons as seen in Fig. 2.2. This makes iron magnetic.

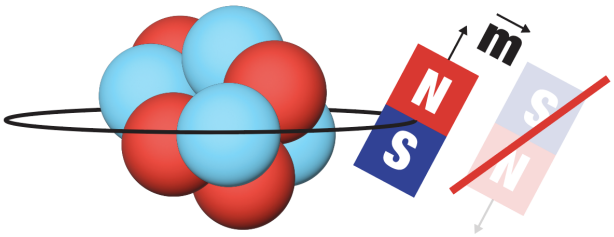

Figure 2.2: Cartoon visualization of unpaired electron spin visualizing an electron as a small permanent magnet.

The magnetic moment is a vector, which implies that it has a direction. To visualize this, imagine the tiny magnetic dipole associated with the electron orbiting the nucleus, which is free to pivot in any direction. We can think of the spin as pointing in the direction of the north pole of this effective magnet. In the presence of an external magnetic field, the magnetic moment experiences a torque that causes it to precess around the field direction. The system is intrinsically dynamic: thermal energy and interactions with the environment drive depolarization over time, and for small ensembles of spins, the degree of polarization fluctuates due to statistical variations, analogous to shot noise. Manipulating spin states and measuring spin polarization is common in physics and forms the operating principle of MRI [2].

Summarizing the generation of magnetic fields, they can either be formed by moving charges as seen in electric currents or from unpaired spins in permanent magnets. We must review how magnetic sensing is conducted in the literature to understand the work presented in this dissertation. It is important to note that the amount of "wobble" is a function of temperature, which is why many magnetic field sensing techniques work much better at cryogenic temperatures, this will be discussed further in the next section.

A quick note on normalization: magnetic field sensitivity is presented in units of $T/\sqrt{Hz}$

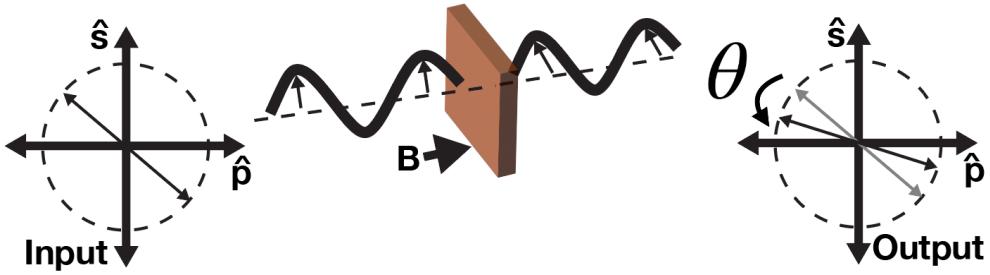

Figure 2.3: Faraday active materials rotate the polarization of light when subjected to a magnetic field. Here, linearly polarized light is rotated by angle θ after passing through the Faraday active material under a magnetic field.

which serves to normalize for integration time. This is key to understanding how much averaging is needed to reach a desired sensitivity.

2.3 Magneto-optic Faraday Effect

In my work on magnetic field sensing, we use the Magneto-optic Faraday effect. In this section I will describe the underlying physics of how external magnetization can affect the polarization of light.

Discovered in the mid 19th century, the Faraday effect describes how the polarization of light is modified by an applied magnetic field [5]. Specifically, the Faraday effect induces a rotation of the polarization axis in a linearly polarized beam as seen in Fig. 2.3. Here is it is possible to see how the polarization has been rotated after passing through the Faraday active material. This has been experimentally validated and is commonly quantified using the Verdet constant, which measures the degree of rotation for a given magnetic field [6].

When subjected to magnetic fields, certain atomic energy states undergo bifurcation from their degenerate configurations. In this process, electrons with different spin orientations either gain or lose momentum due to the influence of the external field. This phenomenon, referred to as Zeeman splitting, describes the dynamic separation of energy levels. The energy difference between these split levels is linearly proportional to the strength of the applied magnetic field.

The position of specific energy levels directly affects the refractive index experienced by

an optical probe. This occurs because Zeeman splitting shifts the atomic energy levels, thereby modifying both the absorption characteristics and the refractive index for a given wavelength and polarization state of light. Notably, this effect alters the refractive index differently for the two circular polarization eigenstates of light, resulting in a phenomenon known as circular birefringence.

The degree of Zeeman splitting, and consequently the magnitude of circular birefringence, is determined by the strength of the applied magnetic field. This relationship also influences the extent of polarization rotation observed in the light [6].

The polarization rotation is dependent on the handedness of the circular polarization, where one polarization couples to the higher Zeeman level and the other to the lower Zeeman level. As a result, a linearly polarized beam experiences a rotation proportional to the magnetic field strength. The governing expression is commonly expressed as follows:

$$\theta = VBL, \tag{2.3}$$

where θ is the amount of polarization rotation, V is the Verdet constant, an empirically derived constant measure of how much polarization rotation is produced for a given field, B is the magnetic field parallel to the optical axis, and L is path length inside the material [6].

While many materials exhibit Faraday activity, certain specialized materials are required for highly effective measurements with high Verdet constants. The ideal material candidates have high Verdet constants, high transparency and a linear response to external magnetic fields. Verdet and loss are materials characteristics that are at odds with each other because Faraday rotation is created by optical absorption features [6].

These materials include terbium-doped gallium garnet (TGG), thin organic films, and some semiconductors. A potential limitation of the technique is that Faraday rotation occurs within an absorption feature, leading to high losses in many materials. However, research has shown that materials such as terbium exhibit highly Faraday-active transitions in the ultraviolet range, which are detectable in the visible or near-infrared spectrum [6, 7]. This enables the material to exhibit

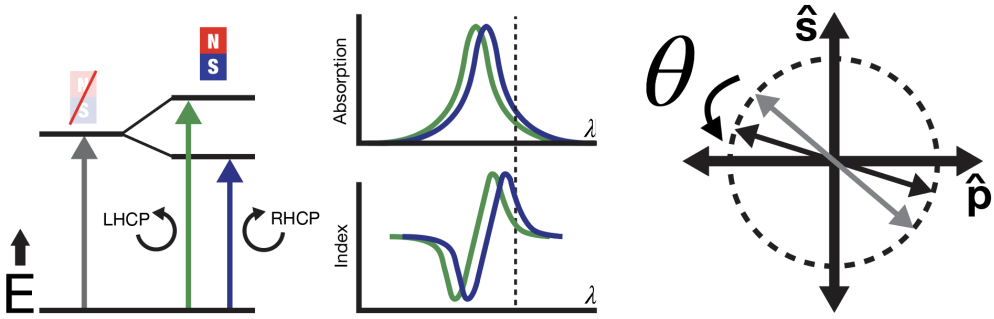

Figure 2.4: Graphical description of how Zeeman splitting produces circular polarization birefringence which produces a polarization rotation of linear polarization. Under no magnetic field, the allowed energy level is a fixed level. However, when the material is subjected to a magnetic field, two bifurcated allowed energy states emerge. One of these new allowed energy states is slightly lower in energy than the original state and the other is slightly higher in energy than the original state. Each energy state interacts with a specific direction of circular polarization (left hand circular polarization, LHCP, and right hand circular polarization, RHCP). The absorption and index as functions of wavelength are offset from each other. This gives rise to magnetically induced circular birefringence in the material.

Faraday rotation without being strongly attenuating.

To produce Faraday rotation, our material needs to become magnetically polarized to an external field. The dynamics of magnetic polarization are controlled by the atomic composition of the material as well as the nano-scale (crystal structure) and micro-scale (bulk material properties). We can broadly characterize magnetic materials as being paramagnetic or ferromagnetic, which will change the magnetic polarization dynamics.

2.3.1 Paramagnetic Faraday Active Materials

We need a material to react to an external magnetic field for it to produce Faraday rotation. How the material reacts is defined by what kind of magnetism the material experiences. As discussed in the previous section, magnetism is observed in materials with unpaired electrons, where the individual atomic or molecular magnetic moments align parallel to an external magnetic field. This alignment occurs because the magnetic dipoles, arising from the intrinsic spin and orbital angular momentum of electrons, experience a torque in the presence of the field, resulting in a net magnetization in the direction of the field.

Paramagnetism is the case where the magnetization in the material is weak and dissipates when the external field is removed, as thermal motion randomizes the orientations of the dipoles [8]. Most materials with unpaired electrons are weakly paramagnetic. The exception is some iron based materials which can be strongly ferromagnetic.

Paramagnetic materials are characterized by their non-hysteretic magnetization response to applied magnetic fields, Here, $m(H)$ represents the scalar projection of the vector magnetization along the magnetic field direction h. When the applied magnetic field is close to zero ($H = 0$), changes in H result in linear changes in m. Saturation of m occurs under large H. This is shown in Fig. 2.5 a. When probed within the linear regime, the response of these materials is ideal for magnetic field sensing since changes in H translate directly to changes in m.

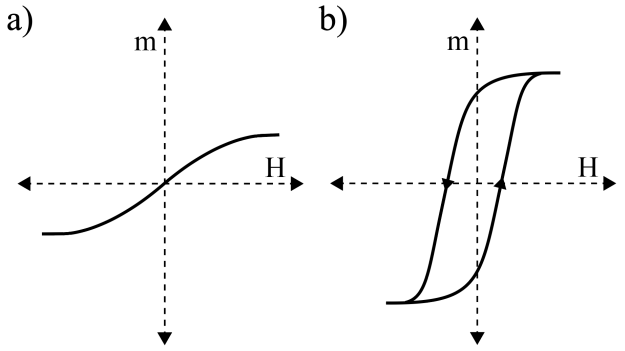

Figure 2.5: Magnetization scalar (m) as a function of applied external field (H) comparison between a) paramagnetic and b) ferromagnetic materials. Paramagnetic materials have a shallow response relative to ferromagnetic materials; however, paramagnetic materials lack the hysteresis displayed by ferromagnetic materials. The nanoparticles used in this study leverage the strong response of a ferromagnetic material without the hysteresis due to what is known as the superparamagnetic response.

2.3.2 Ferromagnetic Faraday Active Materials

Ferromagnetism is a different and much stronger form of magnetism compared to paramagnetism, characterized by the continued alignment of magnetic moments even in the absence of an external magnetic field. This phenomenon arises from quantum mechanical exchange interactions between adjacent atomic magnetic moments, which energetically favor parallel alignment, creating regions of uniform magnetization called domains. When exposed to an external magnetic field, ferromagnetic materials exhibit a dramatic enhancement in magnetization, which persists even after the field is removed, due to the retention of domain alignment [8].

Looking at Fig. 2.5b we find that a hysteresis loop is formed, and the magnetization takes a different path depending on whether it returns from the positive or negative saturation regime. The remanent magnetization is defined as the value of m when $H = 0$. Demonstrates how the material remains magnetic after it has been magnetized. In transition, the flipping of the domains happens very rapidly leading to the significantly steeper response slope when compared to paramagnetic materials.

These materials are more challenging to use for magnetic field sensing because it is not possible to operate in the small signal regime, oscillating back and forth on the steep part of

the curve. The magnetization follows this path only when returning from saturation, and the hysteresis loop becomes smaller if saturation is not reached. As such, defining a Verdet constant is not practical.

To detect magnetic fields with ferromagnetic materials, work in the literature has shown how the hysteresis curve shifts left and right as was shown in [9] (Using Magneto-optic Kerr effect instead of Magneto-optic Faraday effect). However, it is generally challenging to obtain quantitative measurements of the magnetic field.

Ferromagnetic materials can be fabricated into smaller particles with smaller domain sizes either, as thin films or nanoparticles, to produce a paramagnetic like response [10, 11]. This can be combined with other materials to form a more complex nanocomposite. We take this a step further and fabricate ferromagnetic material into nanoparticles, which act in the superparamagnetic regime and react to external fields with the strength of a ferromagnetic material but with the linear response of a paramagnetic material. This will be further discussed in the section on nanomaterials, Sec. 2.8.

Having introduced paramagnetic and ferromagnetic behavior, we can now see how these materials are used in practice to produce Faraday rotation.

2.3.3 Relevant Faraday Active Materials

In making a quantitative review of Faraday active materials I make a distinction between bulk and thin film materials. In our case thin-films operate at thicknesses much thinner than 1 mm, whereas bulk materials are often on the order of or thicker than 1 mm. The thickness will determine the material choice as well as the application.

Bulk materials have historically been the most commonly used Faraday active materials and are formed of glasses or crystals. These devices have low Verdet constants but high transparency. Making the ideally suited for devices such as optical isolators. However, because the Verdet constant is low, long interaction lengths are needed to induce the desired rotation. As such these devices would not be suitable for magnetic field imaging. Additionally, the crystals are challenging to grow

increasing the potential system cost [12].

Vojna et al. provide an excellent comprehensive characterization of bulk Faraday rotation materials [13]. I summarize the performance of a few key materials in the table below.

Material	V **(633nm)**	V **(1064nm)**	α(**633nm**)	α(**1064nm**)	**Source**
BK7	235	-	0.0024	0.0012	[14]
TGG	7,484	2,148	0.23	0.20	[13, 15]
CE:TAG	11,759	3,638	2.1	2.1	[13, 16]
Tb_2O_3	24,189	7,334	1.7	1.7	[13, 17]

Table 2.1: Verdet constants (V) and absorption coefficients (α) for various materials. Verdet constants are expressed in deg /(T $\cdot$ m) and absorption is expressed in units of 1/cm. An exhaustive list can be found at [13].

The table outlines the properties of key Faraday rotation materials, which are most commonly used in optical isolators and circulators. To provide a reference to un-engineered materials we first consider BK7, which is an common glass widely used in optics without considerable magnetic response. The Verdet constant is low at 235 deg /(T$\cdot$m) for a wavelength of 633 nm, it has negligent absorption [14].

TGG (Terbium Gallium Garnet) is the most common magneto-optical crystal renowned for its high transparency. Though the Verdet constant is relatively low compared to other materials. The transparency makes TGG an ideal material for high-performance Faraday rotators and isolators, especially in laser systems [13, 15].

CE:TAG (Cerium-doped Terbium Aluminum Garnet) is another crystal that has been doped with the rare-earth (RE) ion cerium. This is a common method to enhance the Verdet constant of materials [13]. We will even implement it in our own work. There is a modest enhancement over TGG with a significant loss of transparency [13, 16].

Lastly I will review, Tb_2O_3 (Terbium Oxide) which has been sintered using a complex process into a high quality optical ceramic material [17]. This once again leverages the high Faraday rotation of RE-ions to enhance the Faraday rotation. This material has the highest performance of bulk materials that I have found in the literature, with even better loss performance when compared to

the other materials [13, 17].

Across the materials that I reviewed, the optical absorption feature 2.4 that causes Faraday rotation is found in the UV. This means that the performance gets better when operated at shorter wavelengths closer to that absorption feature [13]. Theoretically, the absorption should also increase at shorter wavelengths but in the transmission curves that I have seen in the literature the change is minimal [15–17]. We have made the conscious decision to consider our materials in the near-infrared (NIR) range (780-1550 nm) to leverage access to commercial single frequency lasers which will better enable heterodyne detection. As such we do take a significant penalty in Verdet constant. There is a lot of interest in bulk materials due to the needs of the telecommunication and high power laser industries for high performance optical isolators [13]. These have produced highly transparent materials. However, these materials are not ideal for imaging because of the material thickness which would wash out any near-field magnetic signal of interest. We need to consider the slightly more niche field of thin-film materials. Here we find materials with significantly higher Verdet constants. This comes at the penalty of higher optical loss, limiting the thickness of the materials. Thin-film materials excel in situations where thickness is the primary constraint. This is true for magnetic field imaging because it is desirable to compress the sensor density as close to the near-field magnetic source to optimize sensitivity. I summarize some key results from literature in Table 2.2.

Material	**V(NIR)**	α**(NIR)**	**Source**	**Type**
Tb:Fe_3O_4	560,000	178	[18]	NPs
Fe_3O_4	111,000	74	[19]	NPs
Co:Fe_3O_4	12,000	25	[20]	NPs
FePt	53,000	19	[21]	NPs
Co	580,000	1,000	[22]	NPs
Organics	330,000	7.1×10^4	[7, 23]	Org.
Bi:YIG	200	1.5	[24]	NPs
CE:YIG	1,500,000*	4.5×10^5	[10]	Crystal

Table 2.2: Properties of various thin-film materials in the near-infrared (NIR) range. * Performance extrapolated to 1064 nm.

Thin-film materials are available in a wide variety of forms, with a comprehensive review of

the literature provided in [7]. Unlike bulk materials, thin films generally lack broad wavelength characterization, necessitating the simplification of the results' table for clarity. Thin films for Faraday rotation applications can be categorized into three primary groups based on their composition and performance characteristics.

The first group includes thin films composed of nanoparticles (NPs) embedded within polymer matrices, which encompasses our own work as well [18–22, 24]. These materials are composites in which the nanoparticles, sized to be highly responsive to external magnetic fields, are dispersed within a polymer host. This design combines the high Verdet constants of the nanoparticles with manageable optical losses, making these nanocomposites the state-of-the-art material for magnetic field sensing [7, 18].

The second group consists of pure organic polymer thin films, pioneered by the Swager Group at MIT [6, 23]. These materials leverage complex organic molecules to achieve tunable Faraday rotation. While they exhibit extremely high Verdet constants, their performance is ultimately constrained by significant optical losses, which limit their practical applications.

The third group consists of crystalline yttrium iron garnet (YIG) thin films, typically less than 300 nm in thickness, which exhibit a quasi-paramagnetic response [10, 25]. These materials are known for their exceptionally high Verdet constants, making them a cornerstone of magnetic field imaging applications. However, their practical utility is significantly limited by high optical losses and constraints on maximum film thickness. Consequently, research in this field has largely shifted focus toward nanocomposite films, which offer a more favorable balance between Verdet constant and optical loss [7]. I included a comparison to work on YIG NPs where the performance does not match other materials [24]. Generally since the thickness of the YIG film is limited, the NP based methods are better. Considering a more common 80 nm YIG Film [10] compared to a high performance 35 nm thick NP film (like the one we made) [18] we see 85 times more Faraday rotation for a given magnetic field.

When comparing thin films to their bulk counterparts the best-performing thin films exhibit Verdet constants that are typically two orders of magnitude higher than those of bulk materials.

Similarly, their absorption coefficients are also two orders of magnitude greater. These enhanced properties allow thin films to achieve equivalent performance with much shorter interaction lengths.

Before delving into FRM as our chosen method for measuring magnetic fields, it is essential to first examine alternative techniques. A thorough review of these methods, along with a comparison of their respective advantages and limitations, will provide a clearer context for selecting FRM as the optimal approach.

2.4 Magnetic Field Sensing Review

For our application, it is absolutely critical to consider the operating conditions of the sensors. We require that the sensors are able to function at room temperature, and without shield from the earths native magnetic field. This enables us to use devices in the field without needing to package them or operate in carefully shielded enclosures.

We first look to overview the some of the methods for magnetic field sensing. From these methods we will then refine the list to consider methods that are more relevant to imaging. We can coarsely categorize magnetic field sensing techniques into Inductive sensing and Zeeman effect sensing. Inductive sensing relies on the ability for magnetic fields to induce currents, while the Zeeman effect sensing relies on sensing the bifurcation of atomic transition energy as a function of an external magnetic field that is read out with an optical signal.

2.4.1 Inductive Sensing

Inductive type sensors are probably the most ubiquitous sensors operating in the world. They range from commodity grade electronic chips to highly specialized devices with appropriate. Numerous techniques exist for magnetic field detection; however, we focus on three commonly used methods with potential imaging applications: fluxgate sensors, Hall effect sensors, and superconducting quantum interference devices (SQUIDs). Although the Hall effect is not strictly inductive, the sensor's operational principles are functionally similar to inductive techniques. State of the art fluxgate magnetometers are able to reach to the 0.3 $\mathrm{pT}/\sqrt{\mathrm{Hz}}$ regime [26–28]. Though

high-performance fluxgate transducers are a few centimeter in size, making them not practical for imaging [26].

The highest performance Hall sensors have worse sensitivity when compared to fluxgate sensors, some demonstrating as good as 50 $\text{nT}\sqrt{\text{Hz}}$ [29]. Hall sensors are well tailored to nanofabrication enabling transducer sizes well below 1 μm with 0.87 $\mu\text{T}/\sqrt{\text{Hz}}$ sensitivity [30]. The small transducer size produces high resolution images, but the sensitivity limits the potential applications.

The final category of inductive sensors discussed here exploits novel and sophisticated physical principles. Superconductivity has been shown to enhance the detection of currents induced by external magnetic fields, enabling the development of exceptionally sensitive magnetometers [28]. With state-of-the-art SQUIDs, sensitivities as low as 1 $\text{fT}/\sqrt{\text{Hz}}$ have been achieved [31]. SQUIDs have also shown potential as micro-fabricated devices [32], greatly reducing sensor size. SQUID magnetometers are considered highly effective for imaging; however, their dependence on superconductivity requires cooling with liquid helium, which limits their practicality. We chose not to compare our performance to SQUID due to the operational temperature requirements.

2.4.2 Zeeman Effect Sensing

Various methods for detecting magnetic fields can be broadly classified based on leveraging the Zeeman effect. In particular, we examine the behavior of materials under an applied magnetic field. When closely analyzing material properties, we observe that atoms can occupy well-defined positions corresponding to electron orbitals. These energy levels are determined by the material's chemical composition and crystal lattice structure, as well as other influencing factors. It has been determined that some of these levels experience a bifurcation first described by Zeeman. A greatly simplified example can be seen in Fig. 2.6. This demonstrates how energy levels can split into two distinct states as a function of an applied magnetic field. As the magnetic field strength increases, the energy level splitting becomes more pronounced. Depending on the target atom or molecule, the transitions can be highly complex and have hyperfine line-widths, enabling highly sensitive magnetometers.

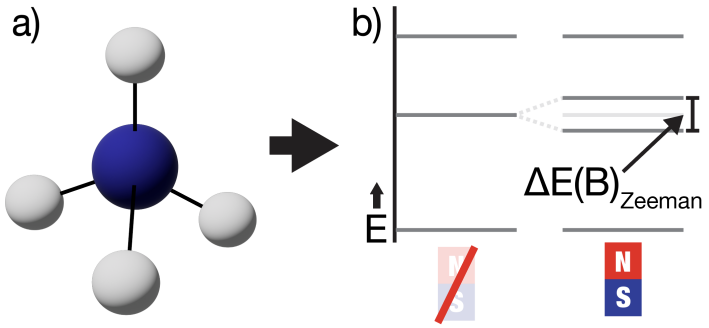

Figure 2.6: a) Cartoon example molecule with bonds and atoms that could define the define energy structure greatly simplified. b) Example energy level diagram for an imaginary atom that experiences Zeeman splitting on one of the levels when an external magnetic field is applied.

This class of magnetometers seeks to measure the positions of these energy levels to deduce the magnetic field strength. Some materials exhibit hyperfine transitions, which have been shown to provide extremely sensitive measurements by probing these levels to quantify Zeeman splitting. This sensitivity has been applied in other domains, such as atomic clocks, where hyperfine transitions serve as highly precise frequency references. These references are now being extended to magnetic field sensing, allowing for highly controlled and sensitive measurements, with access to extremely stable levels.

This opens new possibilities for exploring the physics underlying magnetic field detection and finding innovative methods to measure these transitions using well-established physical principles. We will focus on three primary techniques for magnetic field detection: optically pumped magnetometers (OPMs), nitrogen vacancy (NV) centers in diamonds, and Faraday rotation magnetometry.

2.4.2.1 Optically Pumped Magnetometers (OPMs)

OPMs involve interactions between light and heated alkali vapors, such as cesium or rubidium. One method is direct detection, where microwave transitions are monitored via optical pumping with a laser. As Zeeman splitting occurs, the laser is no longer resonant, and the material's optical transparency decreases, enabling detection of optical intensity as a function of the magnetic field

as seen in Fig. 2.7(left). Recent developments have expanded this technique to more complex physics, including the spin-exchange relaxation-free (SERF) regime. This method leverages atomic collisions to maintain spin polarization even under zero external magnetic field conditions. By utilizing these collisions, the resulting signal is exceptionally pure, allowing for sensitivities below 1 fT/$\sqrt{\text{Hz}}$, outperforming the highest-performing superconducting quantum interference devices (SQUIDs).

However, a key challenge with this method is the requirement to heat alkali gases to temperatures exceeding 150 °C. This necessitates thermal shielding to protect potential samples and careful magnetic shielding to ensure that the system operates within the physical regime where spin-exchange relaxation can occur. The need for such shielding increases system complexity and transducer size. Even so, an example of the current state-of-the-art can be seen in Fig. 2.7, where the miniaturized sensor head is 7.3 mm wide [34].

2.4.2.2 Nitrogen Vacancy (NV) Centers in Diamond

The second technique involves nitrogen vacancy (NV) centers in diamond, where vacancies in the diamond's carbon lattice adjacent to nitrogen inclusions trap electrons with spins that are highly sensitive to external magnetic fields. By understanding the spin dynamics of these trapped electrons, we can extract valuable information about the magnetic field. Like OPMs, NV centers probe hyperfine energy level structures, but they operate using a green laser to excite electrons to higher energy levels, while a radio frequency (RF) field drives transitions between the spin sublevels of the ground state. The ground state of the NV center is a spin triplet, where the application of an RF field resonant with the energy splitting between spin states allows coherent control and manipulation of the population distribution among these levels. The Microwave frequency is then tuned the excitation energy corresponding to the Zeeman splitting frequency which enables direct readout of the magnetic field [35–38].

By carefully controlling the energy level into which electrons decay, researchers can use optical measurement as a function of the microwave excitation frequency. This creates a dip in the

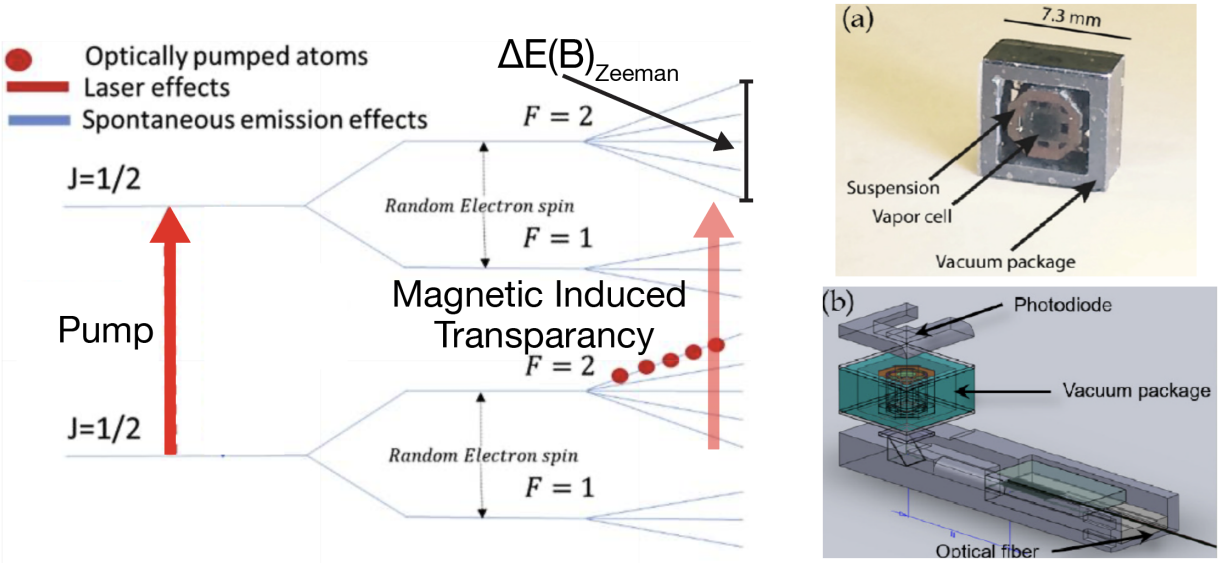

Figure 2.7: left) Electron energy level diagram of Rubidium atoms demonstrating the bifurcation of various hyperfine transitions, figure modified from [33]. right,a) example miniaturized gas cell used in OPM sensing with scale. right,b) Full assembly of OPM sensor head containing the above gas cell and all required hardware for sensing, figure modified from [34].

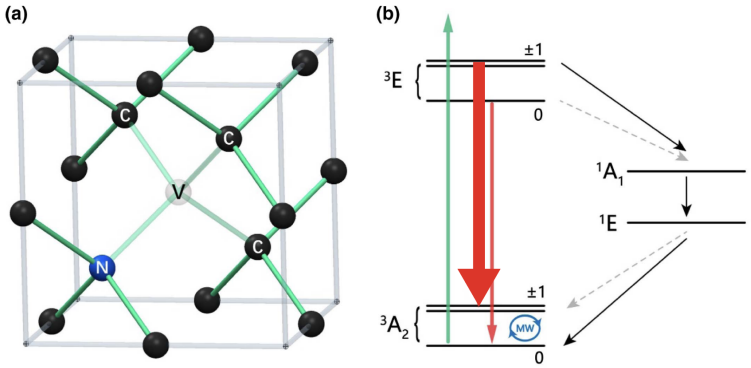

Figure 2.8: a) Diagram of Nitrogen vacancy within a diamond crystal lattice b) Electron energy diagram demonstrating the quantum dynamics which enable NV-center magnetic field sensing through a combination of optical and electrical excitation, figure modified from [35]. Whereas carbon atoms can form four bonds, Nitrogen atoms can only form three. When a Nitrogen atom is placed within a diamond, the void resulting from the crystal defect provides a location for an electron whose spin can be easily manipulated by external fields. A multi-state energy system enables a sensing mechanism wherein microwave electric field biasing can be used to directly probe the Zeeman splitting energies as a function of fluorescent light output.

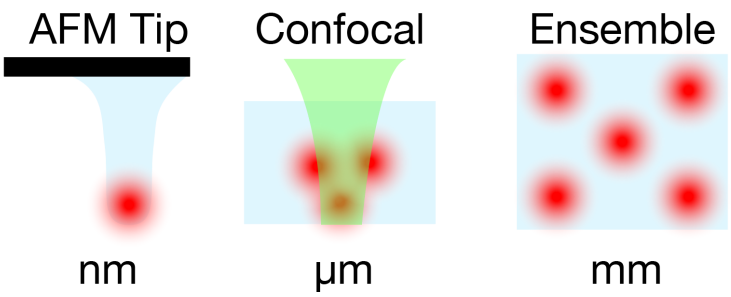

Figure 2.9: Nitrogen vacancy (NV) center microscopy can be conducted across many length scales. At the nanometer length scale, ultra-small atomic force microscope (AFM) tip probe single NV centers. At the micron scale, confocal microscopy probes several NV centers. At the millimeter length scale, ensembles of NV centers are illuminated. When NV vacancies are too close to each other within the diamond, electrons in NV vacancies couple with each other and other impurities [36]. This degrades the sensitivity.

fluorescence efficiency of the atom, which corresponds to the observed Zeeman splitting, yielding highly effective magnetic field measurements. These measurements can be made at various scales, from single NV defects, which have demonstrated sensitivities of DC measurements in the $3 - 10\ \mu\mathrm{T}/\sqrt{\mathrm{Hz}}$ range, to larger ensemble measurements, which offer highly sensitive readings in the tens of picotesla range as seen in Fig. 2.8 [35].

The key question for NV centers is why sensitivity is limited by the number of illuminated NV centers. Increasing the density of NV centers can degrade performance because adjacent centers couple together, reducing their sensitivity to external fields [35–37]. Thus, the sensitivity of the technique is linked to the transducer size. To note: the relationship between size and sensitivity follows across most techniques and is discussed in Section: 2.7.

2.4.2.3 Faraday Rotation Magnetometry (FRM)

Faraday rotation magnetometry (FRM), which leverages the Faraday effect, described earlier, is a direct result of Zeeman splitting. We can use the relationship established in Eqn. 2.3. After measuring the polarization rotation we can extract the applied magnetic field on the sample. This has been done through a variety of materials, ranging from thin and bulk crystals to doped fibers and more recently organic thin-film materials. In this section I will review previous results.

The ferromagnetic YIG has dominated the FRM space since the 1980s because of the high potential Verdet constants [39]. Verdet results can be hard to come by because most measurements are made as the specific Faraday rotation, defined as the difference between polarization rotation at positive and negative saturation [40]. This enables the researchers to ignore the hysteresis and just consider the maximum amount of rotation that a sample generates. As is common practice with many magnetic materials, doping was found to be an effective means of increasing the magnetization and subsequently the Verdet constant of the material, resulting in modest enhancements, typically a factor of around 2x for bulk materials [10, 24, 41–43]. There are two ways that researchers have made quantitative measurements using optical readout of YIG. Most commonly, thin-film YIG materials are created < 100 nm which have a single magnetic domain. These act linearly and have measured Verdet constants to $3,000,000\ ^\circ/(\mathrm{m}\cdot\mathrm{T})$, measured for an 80 nm thick film at 780 nm illumination [10].

A large laser beam can also be used to illuminate multiple domains of all different magnetic domain orientations, averaging the response and producing a linear curve. This reduces the effective Verdet in exchange for linearity [43,44]. Thick GA:YIG crystals have been found to exhibit Verdet constants of 200,000 $^\circ/(\mathrm{m}\cdot\mathrm{T})$ [10], effectively sacrificing an order of magnitude in sensitivity while maintaining similar optical loss. This is also not suitable for magnetic field imaging because the transducer is too thick to spatially resolve any magnetic structures.

YIG based optical magnetometers with 100 $\mathrm{pT}/\sqrt{Hz}$ without magnetic field amplification [43, 45]. These works were done with thick, high loss crystals on the order of 3 mm to produce the required rotation. Thin film results have achieved up to 365 $\mathrm{pT}/\sqrt{\mathrm{Hz}}$ results using complex magnetization schemes [46]. The YIG field has mostly turned to creating electronically (as opposed to optically) read out YIG magnetometers which has produced impressive results down to the $\mathrm{fT}/\sqrt{\mathrm{Hz}}$ [47].

The focus in recent years has shifted away from YIG-based materials toward nanoparticle based thin films. Most advancements have been concentrated in the realm of material development, with relatively limited progress in designing magnetometers utilizing polymer nanocomposites,

despite their significant performance potential.

One notable result in this area involves the use of cobalt ferrite nanoparticles, which achieved a sensitivity of approximately 1 $\mu\text{T}/\sqrt{\text{Hz}}$ [20]. While the authors claim higher sensitivity, this was accomplished through the use of flux concentrators rather than inherent improvements in the material or sensor design.

I have completed my own review specifically to room-temperature unshielded magnetometers in Sec. 2.7. I found an excellent source reviewing the matter more specifically for aerospace applications [48]. I have included a key figure from their work in Fig. 2.10. The key dynamic that I am interested in studying is how does sensor size impact the sensitivity performance. We find that as the sensors get smaller, the performance gets worse. For aerospace applications the size is an important because space and weight is a significant concern. In our case the size effects the potential for imaging resolution.[1]

This opens up my primary research question: is there a magnetic field detection technique that is not limited by the trade-off between size and sensitivity. This is especially important for magnetic field imaging, which is motivated below.

2.5 Magnetic Field Imaging

To begin exploring magnetic field imaging, we must first review prior work and clarify distinctions among the various techniques. A critical factor in magnetic field imaging involves balancing sensitivity with resolution, a trade-off that drives much of the decision-making throughout this dissertation. Key performance specifications include the strength of the magnetic field, the minimum detectable magnetic field, and the achievable imaging resolution of a given device.

Resolution, unlike sensitivity, is determined specifically by transducer size. It is a core performance specification that influences the measurement applications for a given magnetic field imaging technique. Generally, both high sensitivity and high resolution are desirable, but improvements in

[1] Here, we define imaging resolution as the fundamental minimum size of the transducer, with the expectation that the readout optics and electronics can be further miniaturized in a commercial setting.

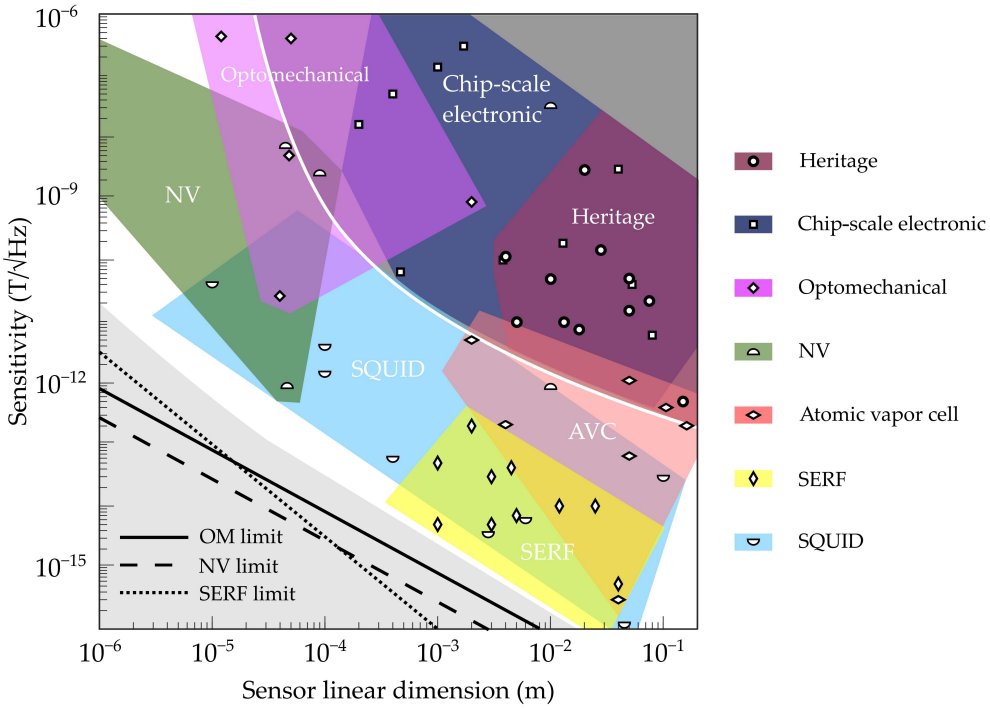

Figure 2.10: Review of magnetometers for space applications as a function of sensor size. Image reproduced from [48]. Here we can see how the size of the device negatively effects the sensitivity. Exceptionally good NV-center results were achieved with some form of flux concentration which locally concentrates the magnetic field on the transducer, amplifying the signal thus achieving lower sensitivity. This is not relevant for imaging.

one often come at the expense of the other.

Another important distinction is between near-field and far-field measurements. This distinction is crucial when considering the magnetic elements that can be imaged. For example, magnetic dipole strength decreases with the cube of the distance from the source ($1/r^3$) for radius r. Therefore, one must either operate close to the sample to capture accurate data or use extremely sensitive devices at greater distances.

Near-field techniques operate at nanometer to sub-micron distances, directly probing the magnetic effects within close proximity to the source. These techniques offer ultra-high resolution, particularly when using atomic force microscopy (AFM) devices, which can achieve resolutions on the order of millimeters. However, to support such resolution, the sensor head must have a very small volume, which limits sensitivity to measurements in the microtesla range.

In contrast, far-field measurements occur at millimeter distances or beyond, where the $1/r^3$ fall-off of magnetic dipole strength becomes more pronounced. To counter this, far-field devices must have ultrahigh sensitivity, often capable of detecting magnetic fields in the femtotesla range. However, this increase in offset distance tends to reduce the achievable imaging resolution unless careful design considerations are implemented.

In far-field imaging, OPMs are the most commonly employed devices. For near-field applications, scanning Hall probes, single nitrogen vacancy (NV) center diamond magnetometry, and ensemble NV diamond magnetometry are preferred. There is an intermediate regime, known as the confocal regime, where imaging resolution is limited by the optical diffraction limit. Faraday rotation magnetometry (FRM) and NV center magnetometry fall within this category. These techniques offer lower resolution than near-field methods but higher sensitivity, and they can operate at micron-scale standoff distances.

A further distinction among imaging techniques involves the difference between single-point raster scanning and full-field imaging also known as widefield imaging (Fig. 2.11). In full-field imaging, a camera captures the entire image at once, collecting data from all points simultaneously. While this approach reduces sensitivity, it is easier to implement and has seen some commercial

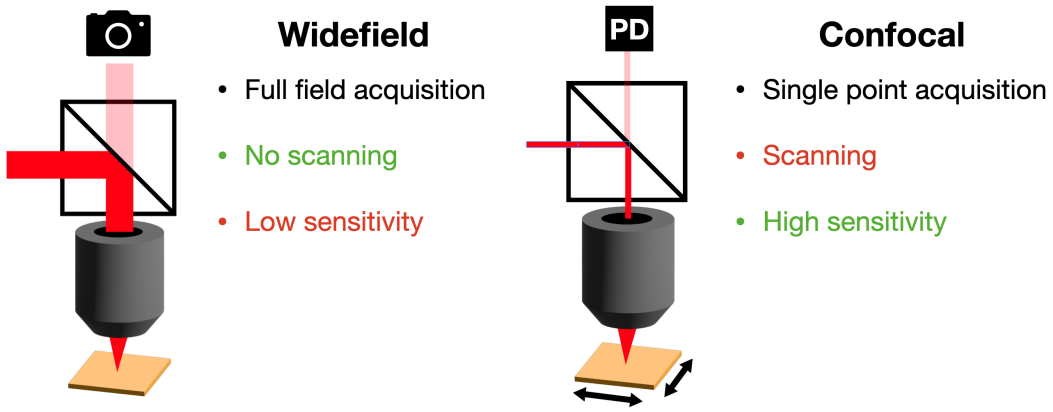

Figure 2.11: Comparison between widefield and confocal magnetic field imaging.

applications. In contrast, for greater sensitivity, single-point raster scanning is used, where the sensor scans the sample one point at a time to produce an image. Although this method increases sensitivity, it also lengthens imaging time and adds complexity to the process.

A key challenge in imaging systems is that sensitivity affects speed: the better the sensitivity, the less integration time is required. This is important because the number of points needed for imaging scales with the square of the number of pixels, which in turn scales with the square of one axis of the image. As we continue, we will consider the various methods and applications of magnetic field imaging techniques as discussed in the literature.

Microscope resolution, on the other hand is defined as the ability to distinguish two closely spaced objects as separate entities, and it is fundamentally limited by the wavelength of light (λ) and the numerical aperture (NA) of the imaging system. According to the Abbe diffraction limit, the resolution is given by

$$d = \frac{\lambda}{2\,\mathrm{NA}} = \frac{\lambda}{2n\sin(\theta)},$$

where n is the refractive index of the medium, and θ is the half-angle of the maximum cone of light collected by the objective lens. Shorter λ and a NA both help to improve resolution, enabling observation of finer details. This relationship underscores the importance of optimizing both the wavelength of illumination and the design of the objective lens to achieve high-resolution imaging

in microscopy.

2.6 Applications

Magnetic field imaging has emerged as a versatile and impactful tool across a wide range of scientific, medical, and industrial disciplines. By enabling the non-invasive visualization and characterization of magnetic fields, this technique provides valuable insights into complex systems and processes. From probing fundamental physical phenomena to advancing real-world technologies, magnetic field imaging addresses critical challenges in areas such as neuroscience, materials science, geophysics, and biomedical diagnostics. The following sections highlight key applications:

2.6.1 Biology and Medicine

Magnetic imaging has found applications in biology and medicine. Considering our sensitivity and resolution performance, one application we are interested in histology. Histology is the study of the microscopic structure of tissues and cells, providing insights into the organization, function, and pathology of biological organisms. This is conventionally done by examining thin tissue sections under an optical microscope. We can expand that though to measure the magnetic field of the same samples. Moreover, histology can provide valuable information for understanding normal physiology and for diagnosing a wide range of conditions, including infections and cancers.

In histology, we aim to image cells stained with magnetic materials, such as nanoparticles [4, 49]. This approach offers several advantages. First, external magnets can be used to manipulate or localize the magnetic contrast agents [50]. Second, since tissue has no intrinsic magnetic activity, this method enables background-free imaging, a significant advantage over most optical imaging techniques.

A few key studies illustrate these benefits. In Ref. [4] (see Fig. 2.12a), diamond NV centers were used to image cells selectively targeted with magnetic nanoparticles. These tagged cells produced magnetic fields in the microtesla range, making them easily distinguishable from untagged cells. Certain cell types, such as those infected by the malaria parasite, exhibit intrinsic magnetism.

These cells were imaged without the need for contrast agents [51] (Fig. 2.12b).

Another notable application is presented in [49] (Fig. 2.12c). In this study, cells were tagged with magnetic nanoparticles, and their hysteresis loop was measured under an external magnetic field. The shape of the hysteresis loop was influenced by the local environment of the nanoparticles, enabling measurements of nanoparticle density and the surrounding liquid characteristics [49].

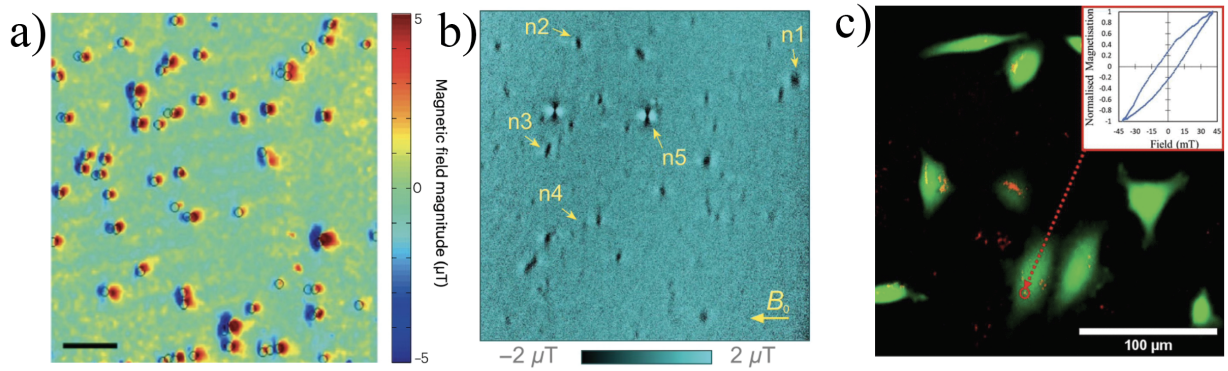

Figure 2.12: Biological applications of magnetic field imaging. a) Cells tagged with nanoparticles [4], b) intrinsically magnetic malarial cells [51], measurement of hysteric loops in magnetically tagged cells [49].

Beyond histology, magnetic field imaging has promising applications in medicine. One potential use of in-vivo magnetic nanoparticles is in tissue heating [52]. This phenomenon is driven by the process of magnetostriction, where magnetic nanoparticles generate heat in surrounding tissue, causing localized cell death. This approach has significant therapeutic potential, particularly when nanoparticles are selectively attached to tumors [52]. The heating effect is demonstrated in Fig. 2.13a. Magnetic field imaging could play a crucial role in measuring the effectiveness of nanoparticle distribution within tumors, providing valuable insights to optimize this therapeutic technique.

An intriguing medical application of magnetic field imaging is the measurement of iron nanoparticle accumulation in the brain. This accumulation has been linked to neurodegenerative diseases. Magnetic field imaging offers a direct and non-invasive method to measure the concentration of these nanoparticles, facilitating a deeper understanding of their role in disease progression

and informing preventative or therapeutic strategies.

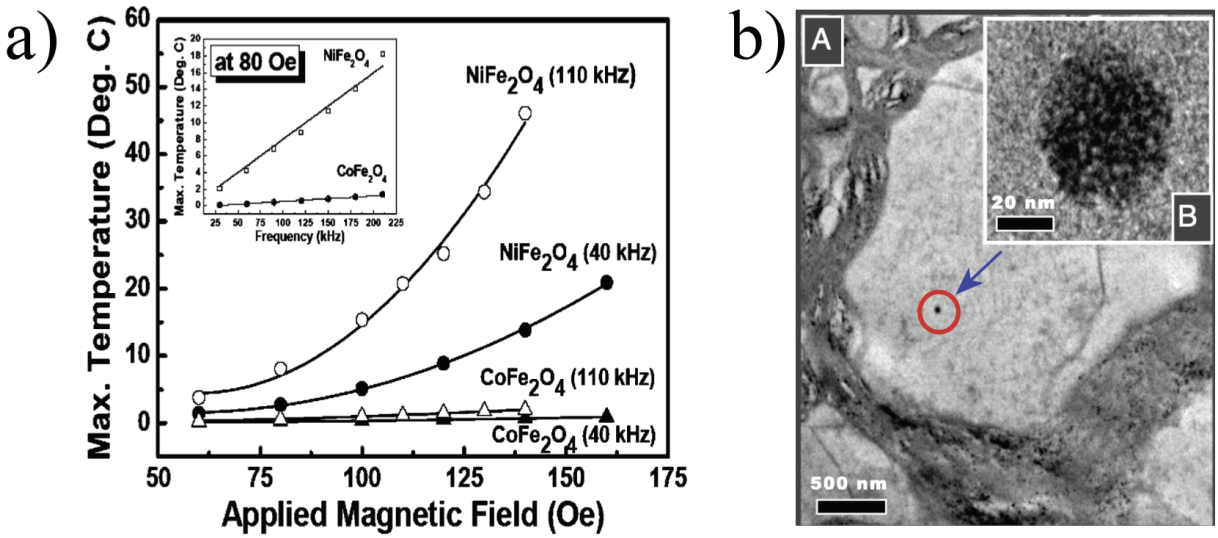

Figure 2.13: Potential medical applications of magnetic field imaging. a) Magnetic induction induce heating of tissue using magnetic nanoparticles [52], b) Electron microscope image of pollution induced magnetite nanoparticles found in the brain [53]

2.6.2 Current Sensing

Another compelling application of magnetic field imaging is the non-invasive measurement of electric currents, as illustrated in Fig. 2.14a. In this example, an NV-center magnetometer was employed to image the currents flowing through a 555-timer chip [54]. Non-invasive current measurements are valuable for electrical characterization, enabling detailed analysis of circuit behavior without physical interference. Additionally, this technique has significant security implications, as it can be used to detect hardware trojans, circuits placed nefariously in hardware which may compromise device security [54, 55].

2.6.3 Physically Unclonable Functions

In the realm of security, there is a growing need for verification stamps that are resistant to counterfeiting. These are referred to as physically unclonable functions (PUFs) [56], which enable robust and unique verification. Nickel micro-magnets offer an intriguing implementation of

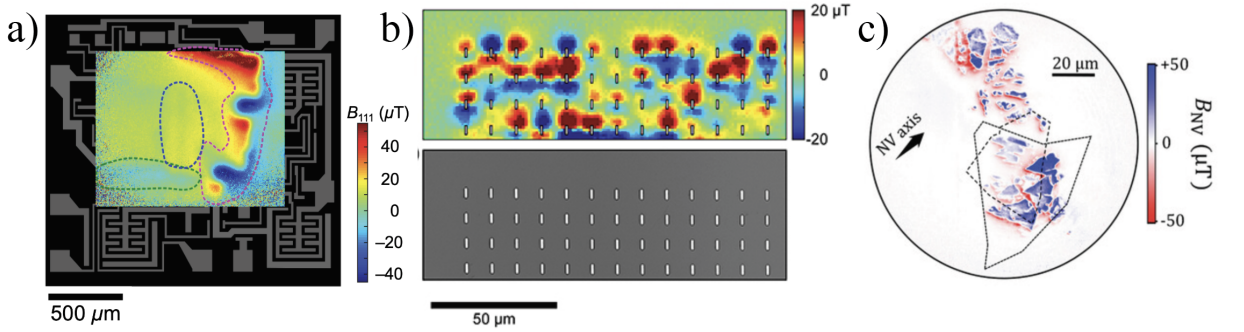

Figure 2.14: More application of magnetic field imaging. a) Current sensing with 555 timer chip using NV-center imaging magnetometer [54], b) physically unclonable function using nickel micro-magnets [56], c) measurement of stray magnetic fields from vanadium tri-iodide crystals [57].

a PUF, leveraging a fabrication process that inherently produces a system that cannot be replicated. During fabrication, each micro-magnet randomly adopts one of two magnetic orientations—North-to-South or South-to-North—as illustrated in Fig. 2.14. This random selection creates a unique grid of magnetic orientations that can be read out as a signature function.

What makes this system unclonable is the impossibility of fabricating an exact copy where every magnetic orientation is replicated identically. Magnetic field imaging plays a critical role in this application, serving as a non-invasive method to accurately read the magnetic orientations of the micro-magnets and verify their authenticity [56]. This approach highlights the potential of magnetic field imaging in enhancing security and authentication technologies.

2.6.4 Condensed Matter Physics

Understanding spin interactions and magnetic fields is foundational in condensed matter physics, a field with immense depth and complexity. While most measurements in this domain are conducted at cryogenic temperatures—outside the scope of my dissertation - they provide valuable insights into validating theoretical physics models through experimental data. As an illustrative example, I will review the specific measurement of magnetic field in vanadium tri-iodide crystals as seen in Fig. 2.14c. This example demonstrates how magnetic field characterization can play a crucial role in probing quantum systems and verifying our understanding of spin dynamics and

material properties. [57]. A more thorough review of application can be found at [35, 58].

2.6.5 Applications-based System Requirements

We sought to broadly discuss the operational regime chosen for our system. Since we aim to perform confocal-style imaging, the first requirement imposed on our system is operation at room temperature. OPMs must operate at elevated temperatures to maintain the alkali metals in a gaseous state [33,34,59]. This necessitates shielding any temperature-sensitive materials from the heat, which increases the standoff distance to the millimeter scale. Which presents a challenge in maintaining micron scale resolution.

Conversely, magnetic field measurements generally achieve higher sensitivity at cryogenic temperatures. At these lower temperatures, electrons exhibit reduced thermal motion, making them more easily polarized. This behavior is also reflected in the temperature dependence of the Verdet constant in Faraday rotation materials where the value of the Verdet constant increases with decreasing temperature [7]. Achieving such conditions would require either cooling the sample to cryogenic temperatures or shielding it from the probe head, which would increase measurement complexity and standoff distance, respectively.

The second requirement for our system is achieving magnetic field saturation above tens (μT). This allows us to treat the Earth's native magnetic field as a fixed bias, thereby eliminating the need for magnetic shielding. Avoiding magnetic shielding is advantageous, as such shielding is often bulky and can complicate measurements.

As such we decided to pursue FRM as the method to move forward with because it satisfies the requirements for saturation and room temperature operation. With the potential for high performance imaging with confocal techniques not being fully realized in the literature.

2.6.6 Faraday Rotation Imaging Results

We broadly reviewed Faraday rotation magnetometers in Sec. 2.4.2.3, and we now focus more specifically on imaging results that have leveraged FRM. I will briefly note that in the imaging space,

the magneto-optic Kerr effect (MOKE) appears to dominate in terms of the number of publications. The underlying physics are nearly identical to the Faraday effect, except that MOKE operates via the rotation of light upon reflection rather than transmission. However, we are ultimately uninterested in MOKE because it is rarely used for quantitative magnetic field measurements [60]. This limitation arises because MOKE signals are strongly dependent on surface properties, such as roughness and magnetic domain structures, which complicate the extraction of absolute field values. Furthermore, calibration of MOKE measurements is challenging, as the Kerr rotation angle depends on both the magneto-optical constants of the material and the optical geometry, making it better suited for qualitative imaging of magnetic domain patterns rather than precise field quantification.

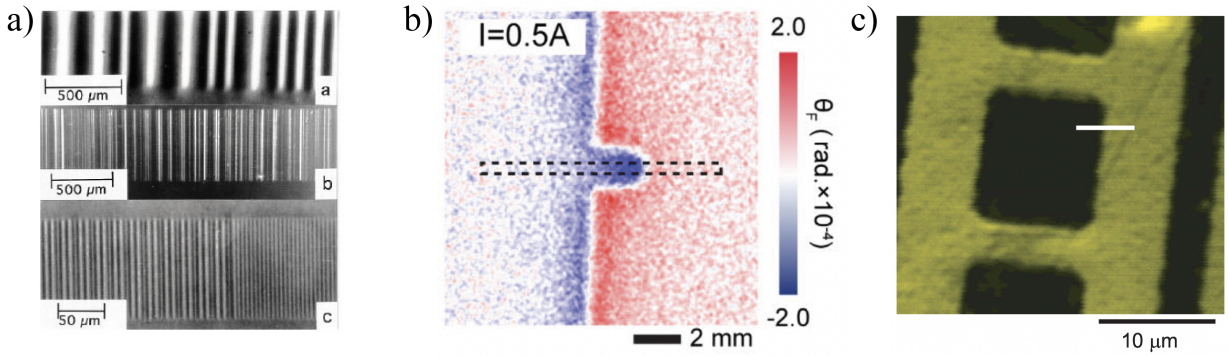

Figure 2.15: Magnetic field images produced by a variety of Faraday rotation magnetometry (FRM) systems. a) Widefield YIG-based FRM of: credit card, audio tape, and floppy disk (top to bottom) [61], b) Widefield FRM image of current in a wire [62], c) Scanning FRM image of engineered domains in YBCO superconductor [63]

In the FRM space, most systems are implemented with a wide-field CCD detector and RE-doped YIG indicator film. Results from such works were summarized in the review paper [61] and I have included one interesting figure in Fig. 2.15a. For example, the magnetic domains of magnetic storage media, such as floppy disks, are clearly visible. The resolution in these cases is limited by the imaging optics which have not been designed for large magnification. In YIG sensing the only thing that can limit the imaging resolution is the domain size, which can be mitigated using very thin films [64]. That result used a thick YIG film with hysteresis to achieve a sensitivity of 10 nT/$\sqrt{\text{Hz}}$ at a single point, and was expanded to utilize a CCD for imaging; however, it was

not calibrated for the measured field [64] and achieved only 300 μm resolution due to the domain size. Another high performance wide-field device was able to achieve 5 $\mu\mathrm{T}/\sqrt{\mathrm{Hz}}$ with micron-scale resolution, though the indicator film and sample were cryogenically cooled [65]. Another key wide-field result reported a sensitivity of 10 μT (with no integration time specified) at approximately 100 μm resolution. In this study, the authors imaged both DC and AC signals in a wire, with the DC result shown in Fig. 2.15b.

Though most of the results were performed in a wide-field fashion, the confocal configuration should produce higher sensitivity as the optical power is concentrated on one spot. I found one high quality scanning FRM result that was able to produce μT sensitivity (no integration time listed) with a 250 nm spatial resolution (visible illumination). This result produced very high quality images as seen in Fig. 2.15c. The only caveat with this result is that the indicator film was cryogenically cooled [63].

To summarize the results of FRM imaging magnetometers, most high-performance work has been achieved using YIG films, as they were the only readily available materials with sufficiently high Verdet constants. While the majority of imaging studies have not prioritized achieving high spatial resolution, a few efforts have approached the diffraction limit for their respective illumination wavelengths [63, 65]. The typical sensitivity achieved in these systems is in the range of $\mu\mathrm{T}/\sqrt{\mathrm{Hz}}$.

I have found no existing work suggesting an inherent advantage of FRM over other imaging techniques. However, in this dissertation, I hypothesize that the ability to concentrate all optical power into a small, diffraction-limited spot size provides a potential advantage compared to other methods that cannot achieve such scaling. This hypothesis forms one of the central research questions of this work, focusing on the interplay between sensitivity and resolution in FRM.

2.7 Sensitivity Resolution Trade-off

Most of the applications that I have reviewed required μT sensitivity to enable measurements. However, further increasing the sensitivity of would enable the possibility of other measurements with further standoff distances, smaller electrical currents or interesting dynamics such as spin

waves [66]. We can look to the field and summarize the results of imaging magnetometers as seen in Fig. 2.16. There is a clear linear relationship between the sensitivity of a technique and the resolution.

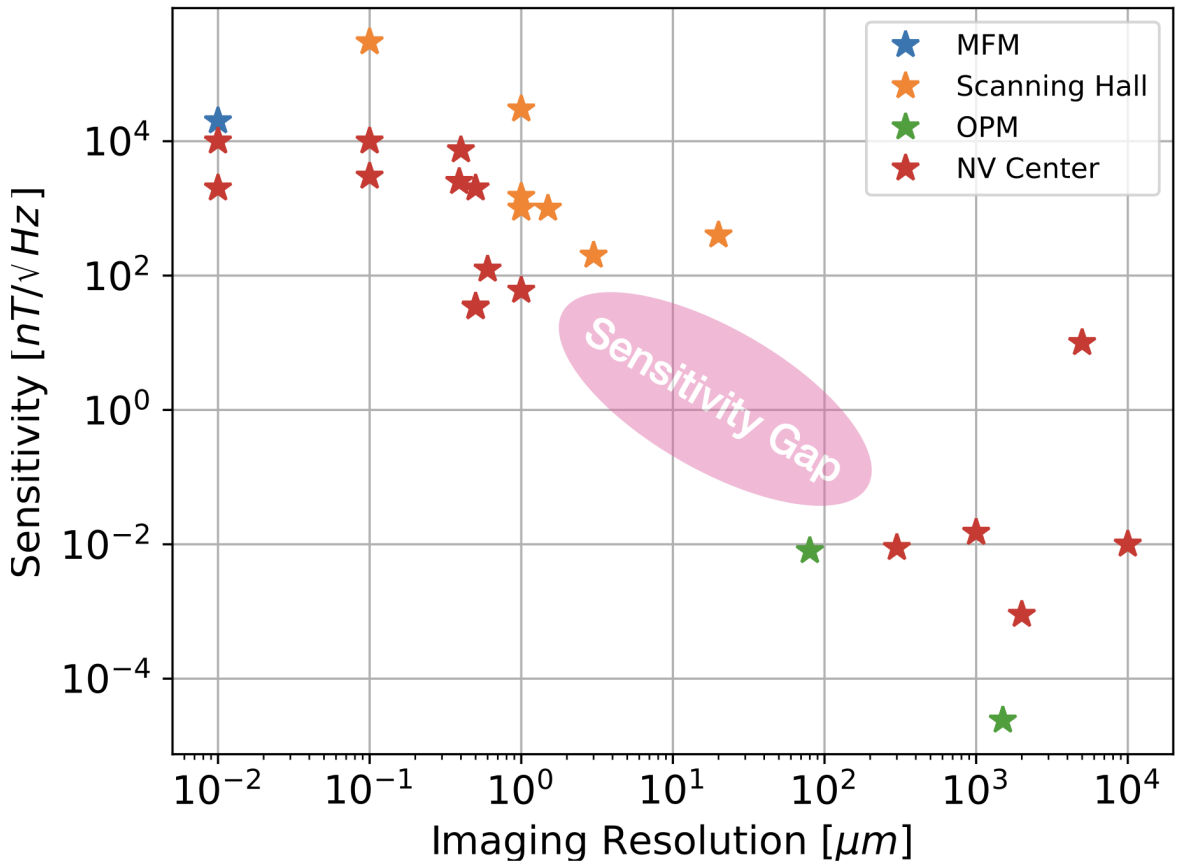

Figure 2.16: Sensitivity-resolution trade-off of room-temperature magnetic field imaging techniques in the literature, with the sensitivity gap we target in our studies identified in pink [34,35,37,38,67–79]. MFM: magnetic force microscopy, OPM: optical pumped magnetometry, NV Center: nitrogen vacancy center magnetometry.

We will unpack this figure further in Chapter 4, but it is important to note that diamond NV-centers represent the state-of-the-art magnetic field imaging techniques across a wide range of resolutions because there are three ways to perform magnetic field imaging as seen in Fig. 2.9.

The sensitivity of NV-center magnetometry is fundamentally determined by the number of NV-centers that are illuminated. In high-resolution configurations, a single NV-center is illuminated, resulting in the lowest sensitivity. In confocal setups, a greater number of NV-centers are

illuminated, while in ensemble configurations, many NV-centers can be utilized simultaneously [35].

However, the density of NV-centers is inherently limited. At higher densities, NV-centers begin to interact with one another and with defects in the host material, which degrades the effective sensitivity [36]. This constraint directly links the sensitivity of NV-center magnetometers to the size of the transducer, highlighting a trade-off between resolution and sensitivity.

2.8 Nanomaterials

One overarching theme of this thesis is the use of nanomaterials to make sensitive measurements. Nanomaterials are materials with structural features at the nanometer scale (typically less than 100 nanometers) that also happen to exhibit unique physical, chemical, and mechanical properties not found in their bulk counterparts. These materials include nanoparticles, nanowires, nanotubes, and nanosheets, which can be composed of metals, ceramics, polymers, or composites. Their reduced size and high surface area enable exceptional behaviors, such as quantum confinement, enhanced catalytic activity, and increased mechanical strength, making them invaluable in various fields, from electronics and energy storage to medicine and environmental remediation.

We can use nanomaterals to create macroscopic metamaterials, also known as nanocomposites. These materials engineered materials designed to exhibit properties not typically found in nature. By introducing the unique characteristics of nanomaterials, we can construct metamaterials with precisely tuned electromagnetic and optical responses that enable us to make more sensitive measurements that would otherwise not be possible with materials on the micron scale and larger.

In our case we consider two different applications that are united through the use of nanoparticles. The first application is the use of magnetite nanoparticles to sense magnetic fields through Faraday rotation. The second application is the use of upconversion florescence to perform nonlinear microscopy.

Observing 2.17 we can find the benefits of using nanoparticles for sensing. Arguably the most important factor of using nanoparticles is the property that the atoms within the nanoparticles

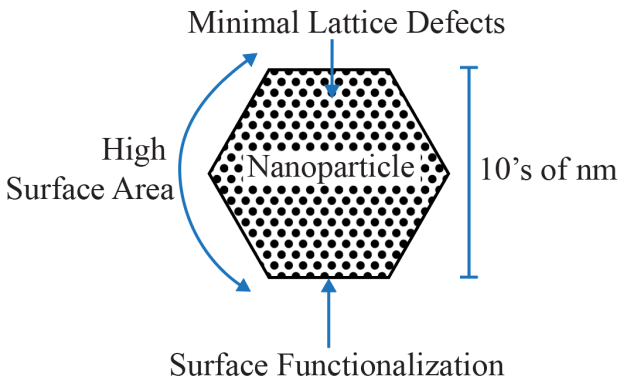

Figure 2.17: Single nanoparticles serve as convenient sensing targets since they are small enough to have minimal lattice defects, yet they are large enough to have high surface areas and can have functionalized surfaces.

form a low defect crystal lattice [80]. This well-formed lattice enables them to be very effective quantum sensors. In the fluorescent imaging case there, low defects enable long florescent lifetimes, increasing upconversion fluorescent efficiency. For magnetic field sensing the lack of defects removes spin trapping sites (areas that limit free movement of spin polarization) and along with the size, enable the nanoparticles to behave in the superparamagnetic regime [11], more easily polarizing to external fields increasing the response. In addition, size of nanoparticles enable them to have exceptionally high surface area to volume ratio. This is useful in chemistry and sensing because they can be highly reactive if needed. This also enables nanoparticles to effectively have ligand molecules attached to the surface. These molecules reach off of the surface and can "functionalize" the nanoparticles by enabling them to feel the surrounding environment. One way sensing is enabled is through surface ligands that preferentially bind to specific cells or cellular structures. The ligand molecules have also been shown to change the properties of the fluorescent light to, for example sense pH or force [81–84]. The surface functionalization can aid in nanocomposite self-assembly or our magnetic indicator films as will be shown in Ch. 3. Lastly the size of the nanoparticles enables them to not affect the imaging resolution. In bio applications the size also allows the nanoparticles to slide in and out of cells to potentially image and measure biological processes [85].

2.8.1 Magnetic Nanoparticles (MNPs)

The fabrication and characterization magnetic nanoparticles will be more comprehensively discussed in Chapter 3. Here we introduce why we chose to work with MNPs in magnetic sensing. To induce Faraday rotation we are looking to polarize the internal spins of a material to an external magnetic field as we saw looking back to 2.5. Expanding this idea, we find that not just the materials, but also the domain size will affect the magnetic performance response [11]. Magnetization (M) is a vector quantity that represents the density of magnetic moments within a material, indicating the degree to which the material is magnetized in response to an external magnetic field. Magnetization reflects the alignment of microscopic magnetic dipoles, and can vary depending on the type of material and the strength of the applied magnetic field. To predict the Faraday rotation

performance we are interested in both how strongly a material is magnetized to an external field and how linear the response is. This will enable us to actually make quantitative magnetic field measurements. Considering Fig. 2.18 we find there are 3 size regimes where the magnetic field behaves differently [11].

Materials with particle size above a certain threshold, (85 nm for magnetite) can be considered to be equivalent to bulk materials. Here we find that the material is large enough to contain multiple crystal lattice domains, each with its respective preferred spin direction. Multi domain material will also have defects between crystal regions that can pin the spin orientations which can reduce a materials' ability to react to an external magnetic field. The impact of this is producing a material with a ferrimagnetic or ferromagnetic response depending on the material. Bulk materials exhibit distinct responses to external magnetic fields due to differences in their magnetic domain structures and the alignment of magnetic moments. The magnetic moments of the atoms will align parallel to each other within the crystal domains, resulting in a strong net magnetization even in the absence of an external field. When an external magnetic field is applied, these domains grow and reorient in the direction of the field, leading to a significant increase in magnetization, which can remain even after the external field is removed — a phenomenon known as hysteresis. This is shown by the open loop of the magnetization curve in Fig. 2.18. Tracking the loop from a positive applied H-field to zero we find that the material still has a some magnetization (m). These materials are useful for permanent magnets but more challenging to use in magnetic field sensing as there is no linear correlation between the applied field and the amount of magnetization.

If the particles are shrunk below 85 nm we consider them to be in the single domain paramagnetic region, which will exists even for intrinsically ferromagnetic materials like magnetite. With a single domain we no longer see any hysteresis or remanent magnetization. The response is linear before it reaches saturation, which better enables magnetic field sensing. This would be the optimal operational regime if not for the behavior under 25 nm in diameter for magnetite [11].

In the final size regime, under 25 nm the particles begin to exhibit what is known as a superparamagnetic response. Superparamagnetic behavior occurs in materials composed of very

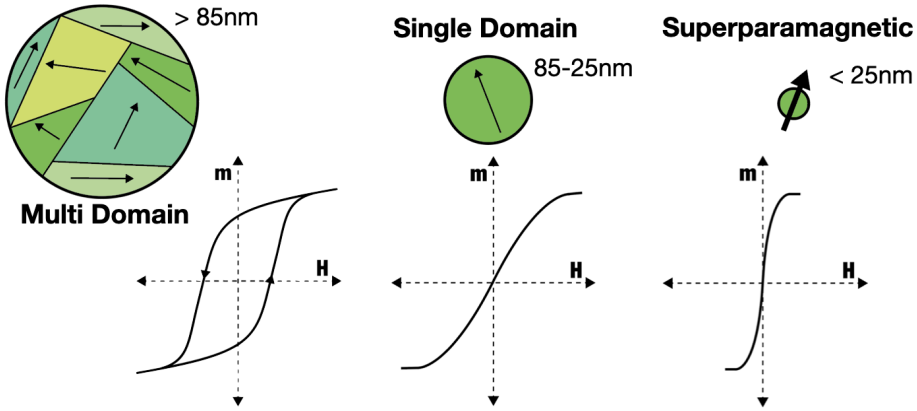

Figure 2.18: Material size dependence on the magnetic field polarization (magnetization) for magnetite-based nanoparticles. In a multi domain crystal, each crystal has a preferred orientation that is self reinforcing and difficult to change. This resistance to change gives rise to hysteresis. Single domain and superparamagnetic systems do not display this hysteresis. Relative to single domain systems, superparamagnetic systems have a stronger magnetization response because their internal magnetic moment are smaller relative to the thermally induced spin fluctuations. Arrows within material sketches represent preferred spin orientation of crystal lattice domains. Three size categories listed with example magnetization curves show below. Size thresholds are different for other materials [11]

small, single-domain magnetic nanoparticles. In these materials, thermal energy is sufficient to randomly flip the magnetic moments, similar to the behavior observed in paramagnetic systems. The key difference is that the magnetic susceptibility is much higher, so the slope of the response is much higher. This greatly enhances our ability to measure small fields as superparamagnetic materials have a much higher Verdet constant. In out case we leverage 17 nm nanoparticles in the superparamgnetic regime to make measurements [11]. These nanoparticles have been broadly considered for magnetic field sensing [6, 7].

2.8.2 Upconversion Nanoparticles (UCNPs)

Nanoparticles are not just use for magnetic field measurements, we also use them for fluorescent imaging. It felt more reasonable to place the necessary background for the UCNP project into Chapter 6, but I will lightly review the concept to contextualize against the MNPs used for magnetic field sensing.

Fluorescence is an atomic absorption mechanism where photons are absorbed and subsequently released at a different wavelength [86]. This has been shown to be useful in a variety of fields ranging from biology to metrology and spectroscopy. The process can be best described using quantum energy level diagrams such a Fig. 2.19 where the ground state (level 0) references the lowest available electron energy state. The absorption of photons will cause electrons to climb to into high energy states where they will decay back to the ground state randomly. As photons decay back to lower energy levels they can release photons corresponding to the change in electron energy [80, 84, 86].

The most simple mechanism is described in Fig. 2.19 where a higher energy (Blue) photon is absorbed by an atom into a level that doesn't perfectly align with given quantum state for that atom, the electron will enter a so-called virtual state. This quantum state is extremely short-lived, and the electron will quickly decay down to a real state with the assistance of a phonon. This is referred to as a non-radiative transition as a phonon is heat instead of light. The electron, now in an intermediate state can then decay radiatively with a lower energy (red/stokes-shifted) photon

compared to the illumination. Since the emitted photons correspond to the atomic states this has found great use in describing the specific quantum energy levels of atomic systems. One can think of this process as entropy assisted, and can be quite efficient, depending on how likely the atomic system is to absorb incoming photons. In the field of biological imaging, limitation were found in penetration depth and background removal when using downconversion. This lead to the development of anti-stokes or upconversion fluorescence materials and processes [87].

A more complicated process is referred to as up-conversion fluorescence. Where two photons are used to doubly excite an electron into an even higher energy state [84]. Producing an (anti-stokes) blue shifted photon and seen in 2.19. This process can either happen through a virtual state absorption which requires simultaneous absorption of two photons [87] or two-step fluorescence which happens through a real transition and is more efficient. However, both processes are less efficient than down-conversion because they are not entropy assisted.

We choose specifically to use rare earth doped sodium yttrium fluoride nanoparticles because they are efficient fluorophores. This is due to the high purity of the crystal lattice, reducing the amount of sites where excitation can decay non-radiatively as heat. This has the effect of increasing the florescent efficiency. The nanoparticles are also able to be surface functionalized with antigens enabling use as contrast agents in histology [81, 82]. Their size enables easy penetration in cells, and the high surface area enables them to bond efficiently with targets. My work with UCNPs is regarding increasing the upconversion florescent efficiency using bi-photon squeezed light in UCNPs. This will be completely discussed in Chapter 6.

2.9 Fluorescence Microscopy

We consider using UCNPs to perform fluorescence microscopy. This is a powerful imaging technique that leverages the principles of fluorescence to visualize and study the structure and function of biological samples. This enables the detection of molecular and cellular details with high specificity and sensitivity. Fluorescence microscopy is widely used in fields such as cell biology, neuroscience, and biochemistry to investigate dynamic processes, spatial organization, and

molecular interactions within living or fixed specimens.

Fluorescence microscopy is a well established field, where researchers are developing novel flourophores to increase imaging depth and potential for specific bonding to biological structures and compounds [87–90]. One novel compound is the UCNPs described above [88–90].

2.9.1 Fluorescence Microscope

Fig. 2.20 illustrates the optical layout of a fluorescence microscopy system. The light is directed into an inverted microscope via a dichroic mirror, which transmits the laser excitation beam towards the specimen through the objective lens. Emitted fluorescence from the sample is separated from the excitation light using dichroic and long-pass blocking filters, ensuring only fluorescence signals reach the detectors. Adjustable mirrors and confocal irises spatially gate the light, enabling confocal depth resolution. The system includes a set of photomultiplier tubes (PMTs) for multi-channel detection, allowing the simultaneous capture of fluorescence signals from different emission wavelengths [86].

A similar schematic can be used for upconversion and downconversion fluorescence. The illumination source and the dichroic mirrors and filters pass bands need to be adjusted to the match the imaging target.

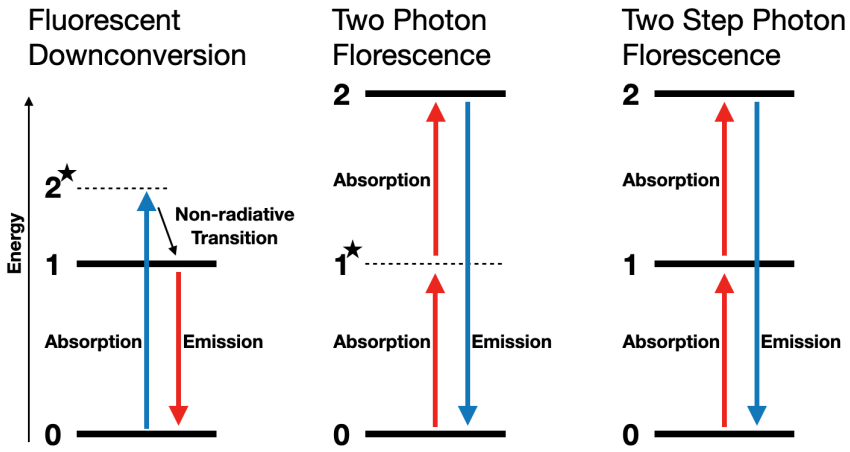

Figure 2.19: Fluorescence mechanisms sketched on energy diagrams. Blue and red arrows represent photon electron transitions; black arrow labeled non-radiative transition represents phonon transition. Energy levels denoted with a star and dashed lines are virtual. In fluorescent downconversion, a photon is absorbed into a real state through a phonon-mediated downconversion and then emitted at a lower frequency. In two photon fluorescence, two photons are simultaneously absorbed and enable a higher frequency emission. In two step photon fluorescence, a single photon absorption raises the electron to an elevated state, and a second photon absorption raises the electron to a higher yet energy state from which a photon is emitted.

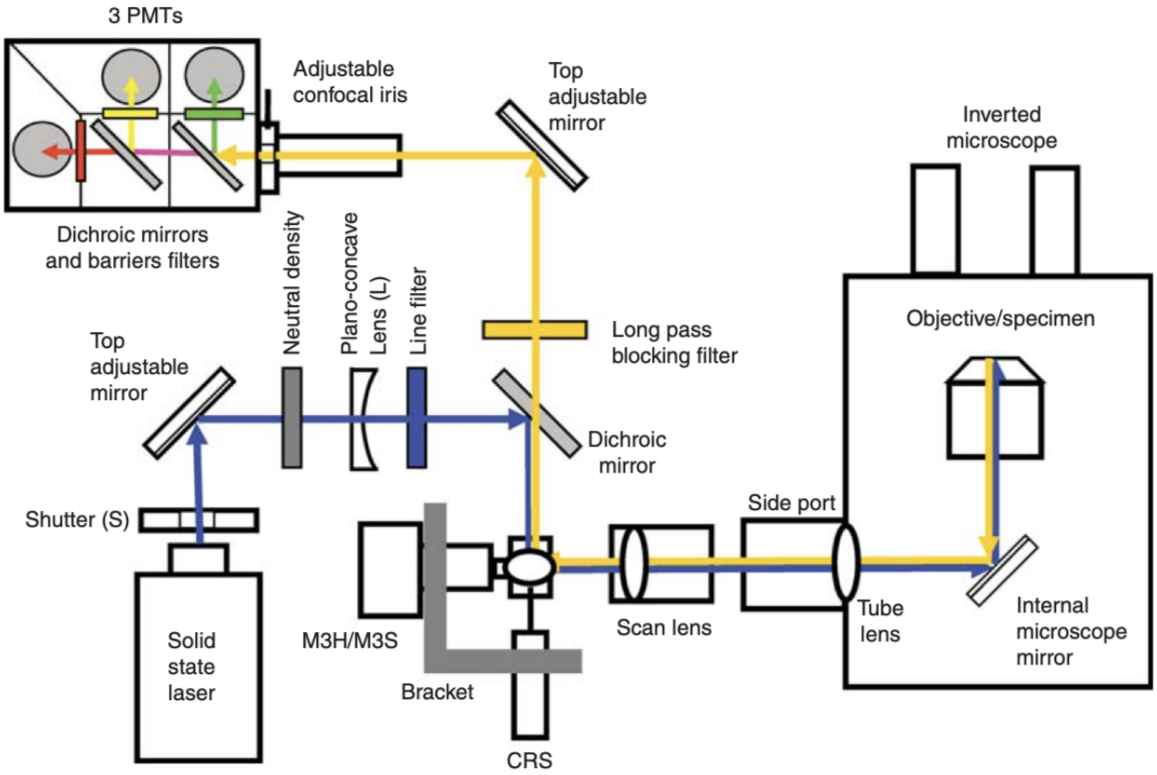

Figure 2.20: Example of a fluorescence microscope schematic from Ref. [86]. Monochromatic light probes a sample which fluoresces. This fluoresced light is collected on a series of wavelength-sensitive detectors. PMT: photomultiplier tube. M3H,CRS: Galvonometers.

Chapter 3

High-Verdet Constant and Low-Optical Loss Tb^{3+} Doped Magnetite Nanoparticles

3.1 Abstract

We have demonstrated that Faraday Rotation Measurement (FRM) is a promising approach for high-performance magnetic field sensing and imaging. However, the material response of even the most effective Faraday-active materials remains relatively low, and any improvement in this response directly translates to enhanced magnetic sensitivity. Recognizing this limitation, we identified an opportunity to advance performance through the development of improved materials.[1]

Nanocomposite thin films, which incorporate Faraday-active nanoparticles within a polymer host matrix, have shown highly competitive Verdet constants while maintaining excellent optical clarity. Our investigation revealed that magnetite-based nanoparticles alone exhibit moderate performance in terms of both Verdet constants and optical loss. However, we discovered that doping these nanoparticles with terbium (Tb^{3+}) ions significantly enhances the Verdet constant without increasing optical loss. This improvement can be quantified using the magneto-optic figure-of-merit (FOM), defined as the ratio of the Verdet constant to optical loss.

By doping magnetite (Fe_3O_4) nanoparticles with Tb^{3+} ions, we introduce a novel strategy for enhancing the Verdet constant while preserving low optical loss. The resulting Fe_3O_4:Tb^{3+}

[1] This chapter was adapted from J. Bartos, et al.: "High-Verdet constant and low-optical loss Tb^{3+} doped Magnetite Nanoparticles" [91]

nanocomposite achieves a state-of-the-art Verdet constant of 5.6×10^5 °/(T·m) and a leading FOM of 31 °/T in the near-infrared region.

3.2 Introduction

The Faraday effect has been used in a wide range of applications in lasers, telecommunications, materials science, quantum computing, and remote sensing [92–95]. It describes the polarization rotation that linearly polarized light undergoes when passing through a magneto-optical (MO) medium [96,97]. Traditionally, MO garnet crystals such as terbium gallium garnet (TGG), terbium aluminum garnets (TAG), yttrium iron garnet (YIG), and rare-earth doped glasses have used Faraday rotators due to their high transparency [94, 95]. To compensate for the rather weak to moderate Faraday effect, these materials are commonly used in bulk configuration with mm to cm thicknesses including optical fiber materials [98, 99]. In recent years, MO polymer nanocomposites have been introduced as alternatives to the conventional MO crystal [94,100–106]. Thanks to their magnetic nanoparticle content, these polymer nanocomposites exhibit ultrahigh MO responsivities and thus can achieve large Faraday rotation with sub-mm interaction lengths. Additionally, they are more flexible for fabrication and processing compared to single crystals [94,107,108], enabling MO polymer nanocomposite thin film that can be integrated with microfabricated devices for various photonic and magnetic applications.

The major drawback of MO polymer nanocomposites is their increased optical loss when compared to MO crystals stemming from nanoparticle's intrinsic material absorption and aggregation induced scattering [94, 100, 104]. The trade-off between MO responsivity and optical loss can be quantified by defining a MO figure-of-merit: FOM= V/α where V is a measure of the MO responsivity known as the Verdet constant and α is the attenuation coefficient [106]. While the Verdet constant is a useful parameter quantifying MO device performance in a power-abundant regime, FOM is a better metric for applications in the power-starved regime when the device insertion loss cannot be tolerated.

To mitigate the scattering losses, the nanoparticles are often coated with polymerizable lig-

ands which allow them to be anchored to the polymer matrix during the polymerization reaction, and thus maintain their spatial dispersion [100, 109, 110]. Other strategies to reduce the scattering loss also include lowering nanoparticle concentration [100], using block copolymers [106], and employing multi-step spin-coating methods with intervening spacer layers [100, 104]. These strategies have been proven very effective, leaving the fundamental trade-off between the MO responsivity and absorption coefficient the remaining challenge to be addressed [97].

In this work, we report a new strategy to enhance both the Verdet constant and FOM of magnetite (Fe_3O_4) nanoparticles via doping with terbium (Tb^{3+}) ions. To induce a strong MO response far away from absorption peaks, it has been suggested that materials containing ions with a C-term Faraday response, which arises from the Zeeman splitting of ground state due to external magnetic field, should be used [97]. Tb^{3+} ions present an ideal candidate for examining this hypothesis. They possess a high magnetic moment, strong spin-orbit coupling, and have allowed optical transitions far from the near-infrared (NIR) region [111]. Earlier studies have investigated the impact of Tb^{3+} and other rare-earth dopants on the magnetic properties of magnetite nanoparticles such as saturation magnetization, coercivity, magnetic moment, and relaxivity [112–117]. The few articles that discussed the effect of rare-earth doping on the magneto-optical properties were either limited in their scope, analysis, and data presentation or have been carried out on other ferrite systems such as cobalt ferrite [118, 119]. Thus, the effect that Tb^{3+} and other rare ions doping might have on the Faraday effect of magnetite nanoparticles remains largely unexplored.

By embedding Fe_3O_4:Tb^{3+} nanoparticles in a polymethylmethacrylate (PMMA) matrix, the Verdet constants and FOM at 980 nm were characterized as a function of the Tb^{3+} doping. We show that an optimal Tb^{3+} doping density of 1.12 mol% results in a 3-fold enhancement of both the Verdet constant and the FOM compared to undoped nanoparticles. The PMMA-Fe_3O_4:Tb^{3+} nanocomposite is a unique material that simultaneously achieves high Verdet constant of 5.6×10^5 °/(T·m) and high FOM of 31 °/T in the NIR, benefiting all applications in either the power-abundant or the power-starved regimes.

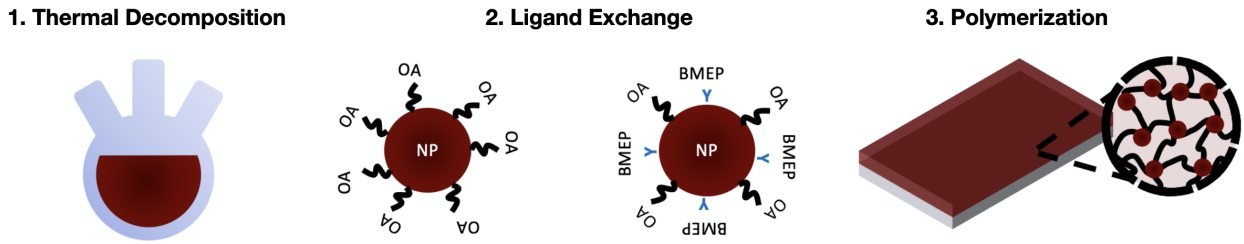

Figure 3.1: Magnetite nanoparticle synthesis process, first the precursor materials undergo thermal decomposition which leads to seed mediated growth during cooling. The surface is first covered in oleic acid (OA) to stop growth. Next some of the OA is exchanged from bis(2- methacryloyloxy)ethylphosphate which is a precursor that enables integration into a polymer matrix in the last step, this prevents particle aggregation.

3.3 Nanoparticle Synthesis

Material fabrication and chemical characterization was performed by my collaborator Dr. Taleb Ba Tis. An excellent comprehensive description can be found in his thesis. [120]. It is necessary to include some details to maintain the completeness of this thesis.

A summary of the process can be found in Fig. 3.1. First the material undergoes a thermal decompensation stage where the precursor materials are dissolved at high temperatures. Next, through the process of nucleation, tiny crystals will form these make up the seed core of the nanoparticles. The process is repeated with fresh precursor materials to continue growth of the nanocrystals. Once the desired size is reached, the particles are coated in oleic acid (OA) to stop further growth. We wish to evenly distribute the particles in a thin film material so the OA is exchanged for a precursor that enables the nanoparticles to be evenly embedded in a polymer matrix. The coated nanoparticles are then transferred to a monomer solution in a solvent and are then polymerized to form a high quality optical thin-film.

Let us look at the process more specifically. The Fe_3O_4 nanoparticle synthesis was carried out using the thermal decomposition protocol with some modifications [112, 121]. Briefly, 2 mmol of iron (III) acetylacetonate, $Fe(acac)_3$, was added to a three-neck round-bottom flask along with 10 mmol of 1,2-hexadecanediol, 9 mmol of oleic acid, 3 mmol of oleylamine, and 20 mL of benzyl ether. The temperature of flask was raised then from room temperature to 110 °C while the reagents

were vigorously mixed using a magnetic stir bar. At 110 °C, the flask was kept under argon for 5 minutes followed by 5 minutes of vacuum purge. The argon/vacuum step was repeated two more times before the temperature was raised again to 180 °C under argon gas. The reaction was kept at this temperature for 2 hours before it was raised again to 298 °C. Once one hour had passed at 298 °C, the reaction was allowed to cool down to room temperature. To synthesize Tb-doped nanoparticles, some of the $Fe(acac)_3$ was replaced by terbium (III) acetylacetonate, $Tb(acac)_3$, while keeping the overall inorganic precursor content fixed at 2 mmol. For instance, 0.01 mmol of $Tb(acac)_3$ was used along with 1.99 mmol of $Fe(acac)_3$ to synthesize $TbFe_3O_4$ (1) nanoparticles. In a similar fashion, $Tb(acac)_3$ amounts of 0.02, 0.05, 0.1, and 0.4 mmol were used to synthesize the $TbFe_3O_4$ (2)-(5) samples, respectively. Following the synthesis, the nanoparticles were centrifuged three times using a mixture of ethanol, methanol, and acetone at 8000 RPM for 20 minutes. After that, the nanoparticles were dispersed in a hexane solution.

Larger nanoparticles were then grown using the seed-mediated growth protocol. Briefly, 80 mg of the core nanoparticles were added to the reaction mixture that was used in their core synthesis. All the other steps were kept the same with the slight modification of 1 hour at 180 °C and 1.5 hours at 298 °C. This seed-mediated growth step was repeated once more using the core/shell nanoparticles as seeds. Following the washing step, the final core/shell/shell nanoparticles were dispersed in chloroform and stored in a desiccator until future use. The exact Tb^{3+} content was confirmed via ICP-MS analysis as shown in Fig. 3.2. The Tb^{3+} molar percentage is calculated as follows: Tb(mol%) = Tb(mol)/(Fe(mol) + Tb(mol)).

One the nanoparticles were grown, there was a need to characterize the material properties to confirm that fabrication had gone as planned. We are interested in the size, chemical composition.

In the experiment, six nanoparticle batches were prepared with increasing amounts of Tb^{3+} using the process described below. As shown in Fig. 3.2 (A-G), the nanoparticles were roughly 14-16 nm in size with standard deviations around 2 nm. Previous reports on the size dependence of the Faraday effect have shown that larger nanoparticles tend to exhibit stronger MO response [105,122,123]. The gain in MO responsivity can, however, be undermined by the propensity of larger

nanoparticle to aggregate due to their strong magnetic interactions [101, 124]. Thus, there is an optimal size where the MO responsivity can be maximized without causing severe aggregation. We opted for 14-16 nm sized nanoparticles because that is the range where both the Verdet constant and FOM were maximized for our system. The Tb^{3+} doping density in the nanoparticles was determined via Inductively Coupled Plasma Mass Spectrometry (ICP-MS) analysis as shown in Fig. 3.2 (H) and further discussed in Sec. 3.4.

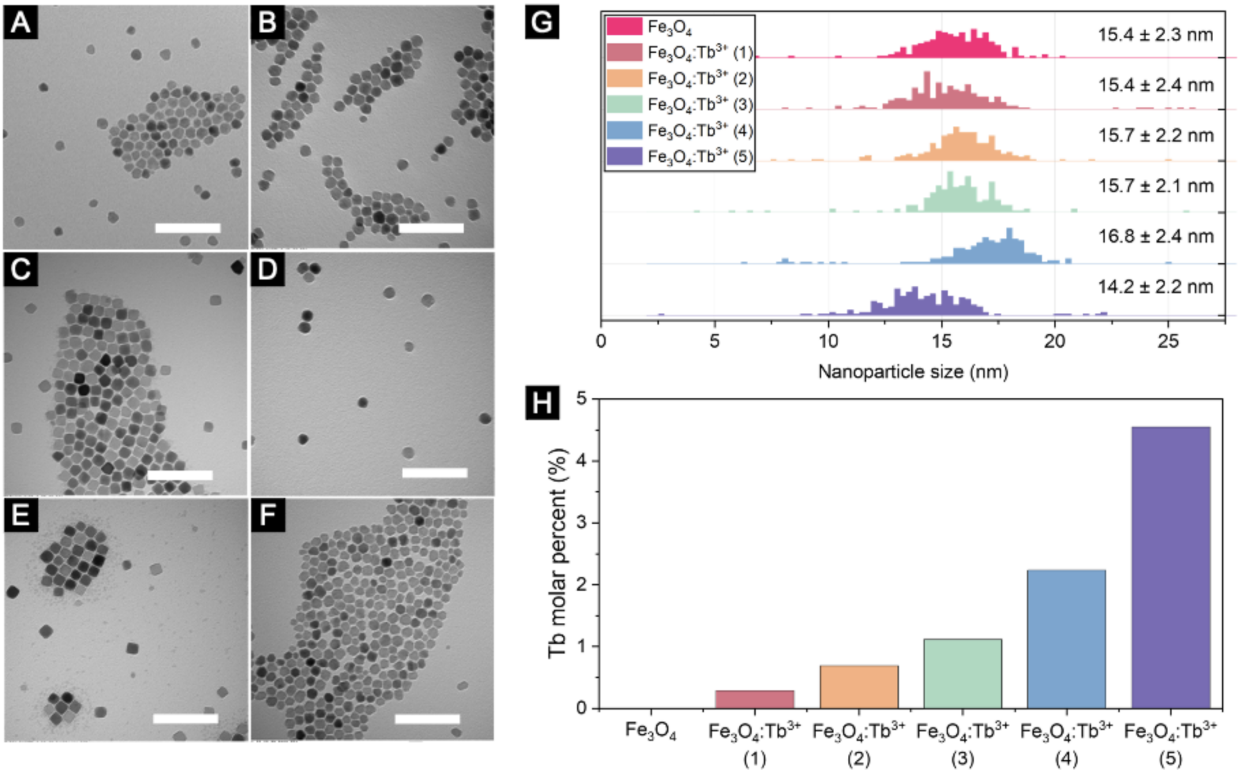

Figure 3.2: Representative TEM images of (A) undoped and (B-F) Tb^{3+} doped magnetite nanoparticles after synthesis. Scale bar is 100 nm. (G) Size distribution of the nanoparticles as calculated from TEM images using the software package ImageJ. (H) Tb^{3+} doping density in the nanoparticles as characterized by ICP-MS analysis.

Once the nanoparticles had been characterized we needed to turn them into a nanocomposite. This was done to spatially separate the nanoparticles to prevent them from magnetically interacting with each other. This was done by first modifying the surface to enable the nanoparticles to become embedded in the polymer matrix. Next raw monomers were added, and the whole mixture was

polimerized into one solid.

To prepare the surface, the native oleic-acid coating of the as-synthesized nanoparticles was replaced using the ligand exchange process with some modifications [110]. Briefly, a 10mg/mL stock solution of bis (2-methacryloxy) ethyl phosphate (BMEP) in chloroform was prepared and stored at 4 °C until use. In a separate vial, 10 mg of nanoparticles were added and dispersed in 0.7 mL chloroform via sonication. After that, 0.3 mL of the BMEP stock solution was added dropwise to the nanoparticle solution. The nanoparticle solution was then nutated overnight to complete the ligand exchange reaction. After the reaction was completed, the chloroform was dried off under vacuum, the nanoparticles were washed once with methanol, and finally collected with a magnet. To the BMEP-coated nanoparticles, another 0.3 mL of BMEP stock solution was added along with 0.7 mL chloroform to maintain the nanoparticles' stability during the polymerization reaction.

To induce polarization, the polymer nanocomposite was fabricated using the in-situ free-radical polymerization reaction of PMMA with some modification [125]. Briefly, 240 mg of methyl methacrylate (MMA) was added to the 10 mg BMEP-coated nanoparticles prepared in the previous step. The solution was mixed thoroughly via sonication. After that, 2.5 mg of azobisisobutyronitrile (AIBN) was added to the MMA/nanoparticle solution and sonicated until fully dissolved. The reaction vial was then partially sealed to allow the chloroform to evaporate during the polymerization reaction which was carried out at 70 °C for 2.5 hours. After that, the vial was placed under vacuum to evaporate any remaining solvent or unreacted MMA. Once fully dry, the weight of the polymer nanocomposite was measured, and the nanoparticle loading was determined by dividing the weight of added nanoparticles by the overall weight of the polymer composite. Due to the incomplete MMA polymerization, the loading is typically higher than the intended 4 wt%. Therefore, additional PMMA (MW 996k) powder was added to adjust the loading to 4 wt%.

The polymer nanocomposite was then dissolved in chloroform to form a viscous solution. Roughly 30-50 μL of the dissolved polymer nanocomposite was then taken out using a pipet and drop-casted on a clean glass slide substrate. The substrate was then placed under vacuum to evaporate the chloroform in a controlled manner and form a polymer thin film for the UV-VIS-NIR

Figure 3.3: Optical image of three nanocomposite films with different Tb3+ doping densities of 0.29 % (left), 1.12 % (middle), and 4.55 % (right). The optical clarity is demonstrated by the clearly visible letters behind the film that do not exhibit any scattering.

spectra and Faraday rotation measurements. The thickness of the polymer nanocomposite films was measured using a stylus profilometer. We find the films to be in a range of thickness from 25 to 37 μm with an average standard deviation of thickness of 5% across the width of the film.

3.4 Optical Characterization

With the size and chemical composition of the nanoparticles characterized. We moved onto optical characterization of the material. For this we ultimately care about two parameters, the first is the optical loss in the material. This is caused by two factors.

The first factor is optical absorption by the material. The PMMA host matrix is highly transparent, so the loss caused by the magnetite nanoparticles. The loss of the material can be controlled by changing the concentration of nanoparticles in the material. Absorption is critically important because it leads to heating of the nanoparticles. As discussed in later chapters, this heating is what ultimately cases the damage threshold of the materials to be quite low.

The second factor is optical scattering. Scattering is a problem because not only does it reduce the returned optical power but also because it will also degrade the potential for high resolution imaging. The nanoparticles are much smaller than an optical wavelength and thus in the Raleigh scattering regime. We found high optical quality in the films which suggested there was minimal scattering. The film quality can be seen in Fig. 3.3.

To characterize the optical absorption we used a VIS-NIR absorption spectrometer with the results shown in Fig. 3.4 demonstrating the wavelength dependent absorption spectrum of

the PMMA-Fe_3O_4:Tb^{3+} nanocomposite films, measured with VIS-NIR spectrophotometry. The intervalence charge transfer (IVCT) transitions of the Fe^{3+} and Fe^{2+} ions [126, 127] that result in magnetite's strong MO response also led to a strong UV absorption band and an elevated NIR absorption peak centered around 1400 nm. On the other hand, no additional NIR absorption is observed when Tb^{3+} is doped into the magnetite nanoparticles, rendering Tb^{3+} doping an effective strategy to simultaneously enhance the Verdet constant and FOM. The lack of any significant changes in the absorption spectra after doping are likely due to the low Tb^{3+} concentration and its small absorption cross-section in comparison to magnetite [126, 128]. The 15% variation in absorption coefficients among different samples is attributed to the uncertainty of the nanoparticle loading which is uncorrelated with the Tb^{3+} doping density. Fig. 3.3 shows an optical image of representative 30-μmthick nanocomposite films with different Tb^{3+} doping densities. The text behind the PMMA- Fe_3O_4:Tb^{3+} nanocomposite films remain sharp without distortion, confirming that the Tb^{3+} doping does not degrade the optical quality of the nanocomposite films.

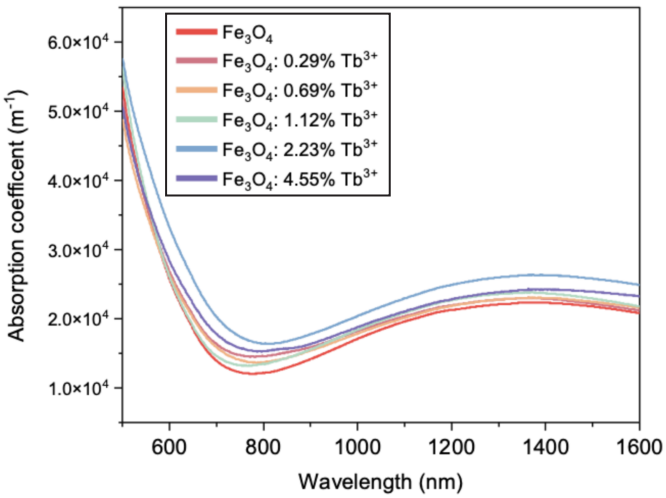

Figure 3.4: VIS-NIR absorption coefficient of the PMMA-Fe_3O_4:Tb^{3+} nanocomposite.

Most critical of all, we had to measure the Verdet constant of the material. This was done by applying a known magnetic field and measuring the response of the material.

The Verdet constant measurement apparatus, illustrated in Fig. 3.5, was designed following

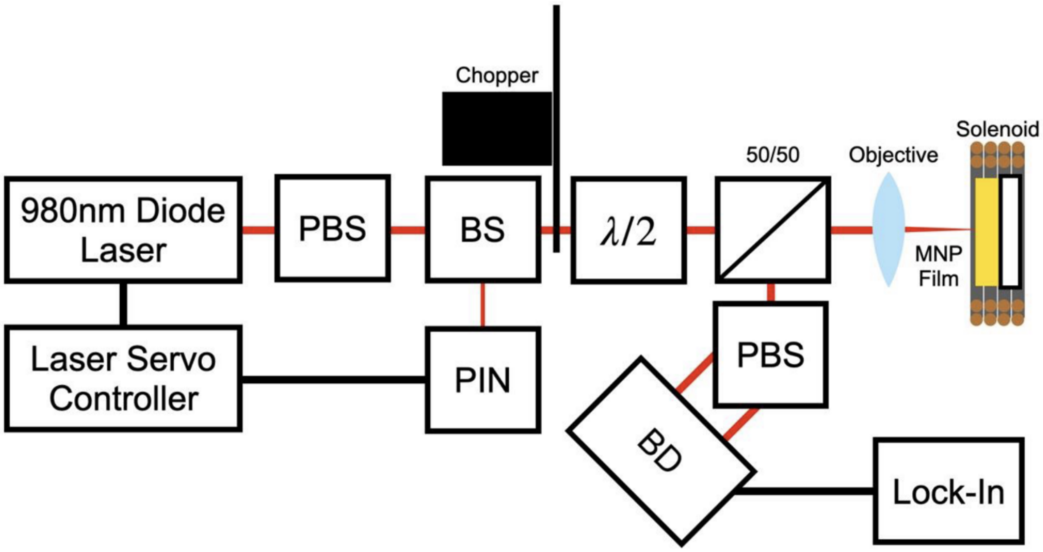

Figure 3.5: System schematic, PBS: Polarizing beam splitter, $\lambda/2$: Half waveplate, BS: Beams sampler, PIN: Photodetector, BD: Balanced detector.

the setup reported in Pavlopoulos et al [100].

To reduce the effects of sample oxidation the samples were measured within two weeks of fabrication. The measurement apparatus is shown in Fig. 3.4 and closely resembles the setup described by Pavlopoulos et al. [100]. The light from a 980 nm pump driver diode is first linearly polarized, and a beam sampler is used to pick off a small portion of the light to measure the intensity of the light. This creates a feedback loop with a PID laser servo controller allowing us to stabilize the laser power against polarization instability from the light delivery path.

Looking more closely at the stabilization performance, we find that we are able to suppress the laser noise by almost 20dB. This is shown by the difference between the orange and blue lines in Fig. 3.6. We find that up to 300Hz we are able to completely suppress the laser noise to below the noise floor of the photodetector. An important note should be make when comparing the in-loop noise Fig. 3.6(a) (Laser to PIN) is that the noise is suppressed to around 1 Hz bandwidth. However, when considering the out-of-loop noise Fig. 3.6(b) (Laser to BD) the suppression becomes significantly worse at 10Hz. This demonstrates that the sample is inducing noise that is not

corrected by the PID loop. We utilized careful shielding to reduce environmental noise but were not able to fully remove it. Using a magnetic shielding chamber was also done but created optical pointing issues which did not reduce the low frequency noise.

The light is then fed through a free space optical chopper to create a signal that can be detected using lock-in detection. A half waveplate on motorized rotation stage is used to bias the light to 45° as well as perform responsivity calibration. We focus the light through the sample and onto a mirror with a long focal length lens (f=100 mm). This double passes the MNP sample negating any residual polarization effects such as stress birefringence from the sample. The magnetic field is applied at DC using a simple homemade solenoid coil.

The light returning from the sample is passed through a Wollaston prism polarization beam splitter onto an autobalanced detector (New Focus Nirvana 2017). The amplitude of the chopped optical signal is measured and recorded by a lock-in detector (Stanford Research Systems, SRS830). To perform an acquisition, the sample is mounted into the solenoid coil. The light first rotated by 0.6 ° (0.3° physical rotation of half waveplate) using the motorized mount. This serves to calibrate the responsivity of the system to the specific optical power incident on the detector (Nominally 300 μW on each port). The solenoid coil is then energized at 3 different field strengths and the results averaged for 30 seconds.

We measure the Faraday rotation of the PMMA-Fe_3O_4:Tb^{3+} nanocomposite films as a function of the applied DC magnetic fields. The Faraday rotation, θ_F, is then normalized by the film thickness, L, to determine the Verdet constant, V according to the equation:

$$\theta_F/L = VB, \tag{3.1}$$

where V is the Verdet constant, B is the applied DC magnetic field, and θ_F/L is the specific Faraday rotation. When the applied DC magnetic field is plotted against the specific Faraday rotation, the slope of the response is determined by the Verdet constant.

It is important to note that while equation 3.1 assumes a linear relationship between the

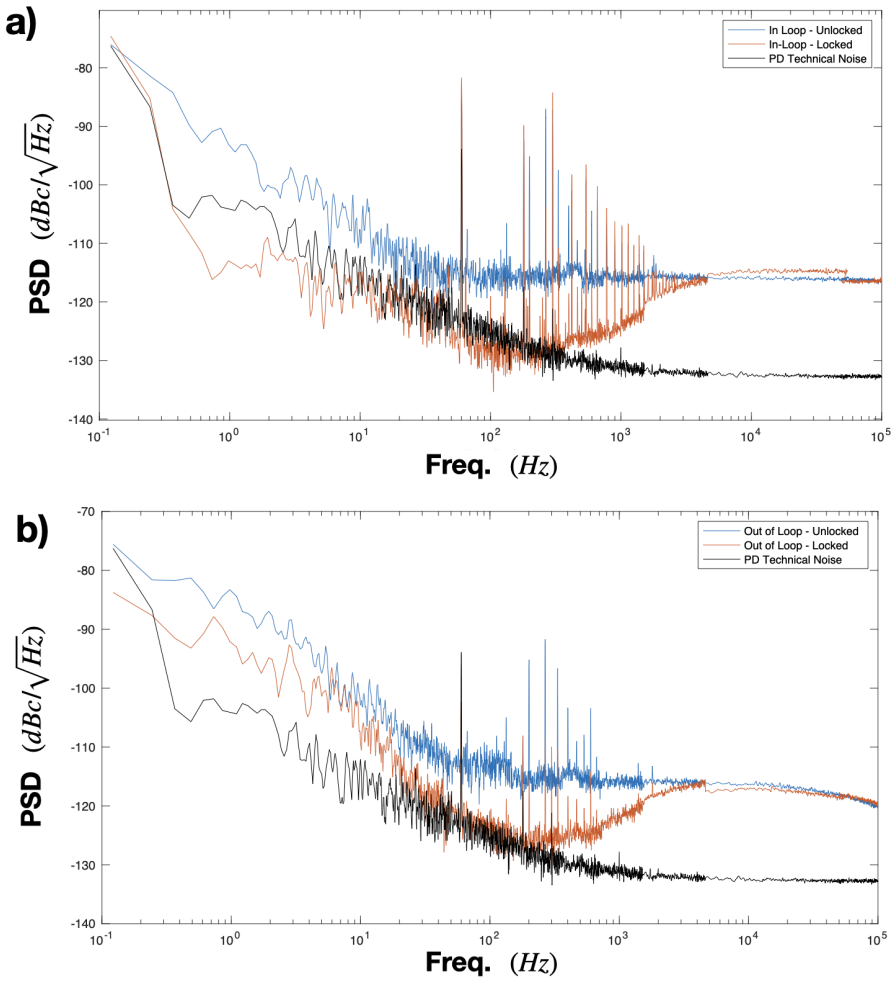

Figure 3.6: Noise power spectral density of stabilization loop. a) In-loop measurement measures noise within the PID stabilization loop. b) Out-of-Loop measurement measures noise at the balanced detector. Locked and unlocked state represents the PID loop being enabled and disabled. Black line represents the electronic noise floor of the PID system which was limited by the dark noise of the photodetector.

Faraday rotation and magnetic field, some MO materials deviate from the linear behavior especially at high magnetic fields [94,101]. To find the validity range of equation 3.1 for our material, we first measured the Faraday rotation of the undoped nanoparticle over a wide range of magnetic fields (i.e., 0 – 90 mT). As shown in Fig. 3.7, the Faraday rotation starts saturating at magnetic fields greater than 10 mT. As a result, we used magnetic fields below 0.5 mT, safely within the linear region as shown in Fig. 3.7 for all subsequent Faraday rotation measurements.

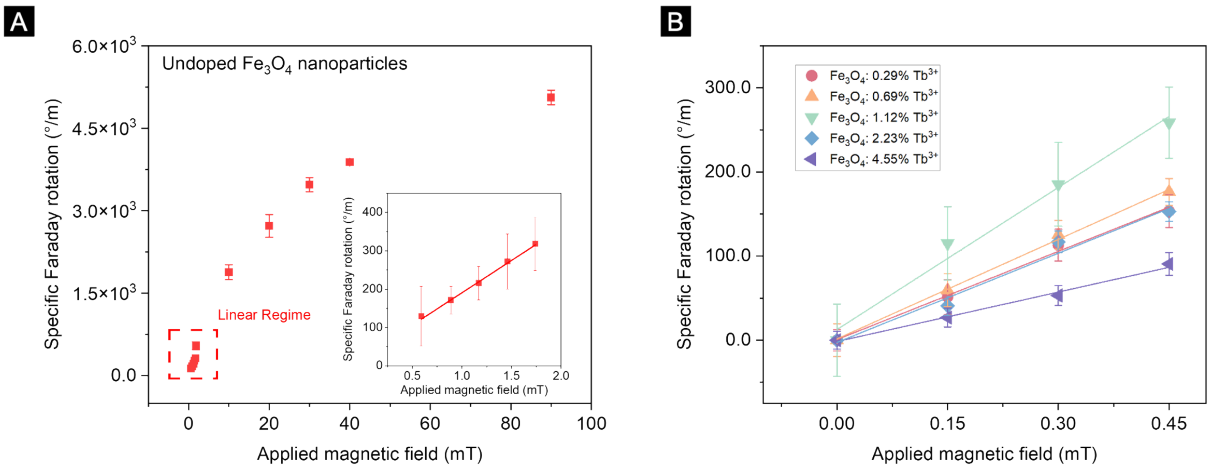

Figure 3.7: (A) Specific Faraday rotation of undoped nanoparticle thin films demonstrating saturation above 10 mT, inset demonstrating linear regime of nanoparticles. (B) Verdet Constant measurements of all fabricated thin films in the linear region. The solid lines are the linear fits of the specific Faraday rotation as a function the applied DC magnetic field.

Fig. 3.8 shows the Verdet constants and FOMs of the PMMA-Fe_3O_4:Tb^{3+} nanocomposite films as a function of Tb^{3+} doping. Both Verdet constants and FOMs reach their peaks at 1.12mol% Tb^{3+} doping, confirming the effectiveness of Tb^{3+} doping to simultaneously enhance the Verdet constant and FOM. The maximum Verdet constant and FOM are 5.6×10^5 °/(T·m) and 31 °/T, respectively, representing a 3-fold enhancement over the undoped magnetite nanoparticles. Fig. 3.9 compares our results to other room temperature MO polymer nanocomposites with 4 wt% loading in the NIR. Our new PMMA-Fe_3O_4:Tb^{3+} nanocomposite is one of a kind that achieves not only high Verdet constant but also high FOM. Compared to the best Co nanocomposite that has a comparable Verdet constant, our new PMMA-Fe_3O_4:Tb^{3+} nanocomposite exhibits an over 5-fold

higher FOM. Compared to the best FePt-nanocomposite that has a comparable FOM, our new PMMA-Fe_3O_4:Tb^{3+} nanocomposite exhibits an order-of-magnitude higher Verdet constant. Our new PMMA-Fe_3O_4:Tb^{3+} nanocomposite outperforms other MO polymer nanocomposites in both Verdet constant and FOM.

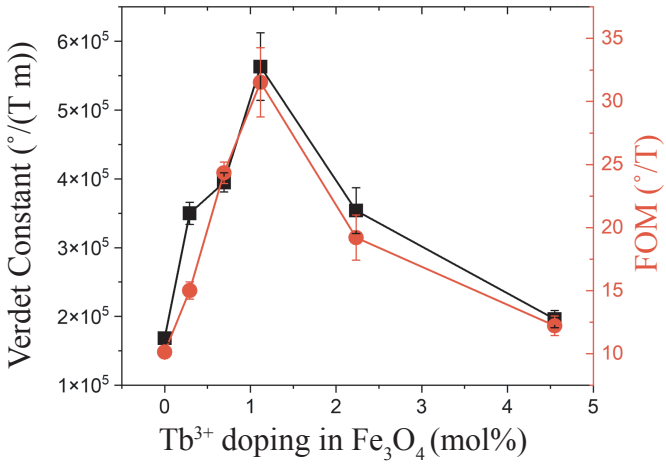

Figure 3.8: Verdet constant and FOM as a function of Tb^{3+} doping density. Positive sign indicates clockwise polarization rotation of light in an anti-parallel magnetic field.

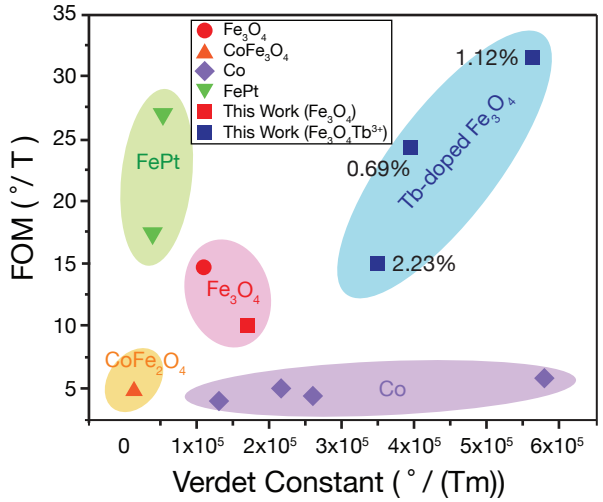

Figure 3.9: Comparison against other room temperature MO polymer nanocomposite in the NIR (800-1300 nm) [100, 102, 103, 105]

Magnetite's strong MO response has been attributed to the allowed IVCT transitions of the

Fe^{3+} and Fe^{2+} ions [127]. The paramagnetic lineshape of these IVCT transitions, particularly in the UV and NIR region, suggest that their contribution to Faraday rotation is of a C-term nature. The magnitude of the C-term MO response is proportional to the dipole transition strength and the magnetic moment of the ground state as shown in equation 3.2:

$$C(j \leftarrow n) = \frac{1}{d_g} \langle n|m_z|n\rangle \ \mathrm{Im}\left\{\langle n|\mu_x|j\rangle \langle j|\mu_y|n\rangle\right\}, \tag{3.2}$$

where n and j are the initial and final states, d_g is the degeneracy of the initial state, the $\langle n|m_z|n\rangle$ term is related to the ground state magnetic moment, and the $\mathrm{Im}\left\{\langle n|\mu_x|j\rangle \langle j|\mu_y|n\rangle\right\}$is related to the dipole transition strength, m_z is the magnetic dipole moment operator parallel to the light propagation direction, and μ_x and μ_y are electric dipole moment operators perpendicular to the light propagation direction [97]. In Fe^{3+} and Fe^{2+} ions, both the magnetic moment and transition dipole strength are large, thereby leading to a high Verdet constant [127].

As denoted recently by Nelson et al. [97], C-term MO responses are ideal for applications where minimal optical loss is desired because the peak of the MO response is shifted with respect to the peak of the absorption band and the MO response has a long tail, extending beyond the region of strong absorption [97]. On this basis, we believe that doping with Tb^{3+} leads to an additional strong C- term contribution to the NIR Faraday rotation, originating from its high magnetic moment as well as its 4f-5d allowed transition in the near UV region [129]. The fact that the MO enhancement peaks around 1.12 mol% before it starts decreasing suggests that another competing effect starts to take over at higher doping levels. A likely culprit in this case is the lattice distortion created by the incorporation of larger amounts of Tb^{3+} ions, thereby negatively impacting the overall magnetic ordering of the ions in the magnetite lattice. Previous studies on rare earth ion doped magnetite nanoparticles have observed a similar behavior with respect to the saturation magnetization and attributed it to the increased lattice strain and disorder and the possible formation of secondary phases when the rare-earth doping exceeds the critical solubility limit [116, 117, 130, 131].

In summary, we report a new strategy to simultaneously enhance the Verdet constant and FOM by doping magnetite nanoparticles with Tb^{3+} ions. At the optimal Tb^{3+} doping density of 1.12 mol%, the PMMA-Fe_3O_4:Tb^{3+} nanocomposite is one of a kind that simultaneously achieves high Verdet constant of 5.6×10^5 °/(T·m) and high FOM of 31 °/T in the NIR, benefiting all applications in either the power-abundant or the power-starved regimes. Our work demonstrates a new strategy toward engineering high performing MO nanoparticles and paves the way toward their potential in magnetic field sensing and imaging.

Broadening this summary to the broader context of this thesis, our work aims to advance the sensitivity and resolution of magnetometers. The materials developed in this study exhibit significantly reduced optical losses for a given level of Faraday rotation. This improvement simultaneously enhances the optical power available to the detector—thereby increasing sensitivity—while minimizing heating effects caused by absorption. Furthermore, the films demonstrate exceptionally low optical scattering, preserving imaging resolution through the material. This characteristic provides the potential for high-resolution imaging applications.

Chapter 4

Advanced Detection Techniques of Faraday Rotation

4.1 Abstract

In the previous chapter we had enhanced the material properties to better enable Faraday rotation magnetometry (FRM). Here, we look to enhance the way that FRM measurements are made with the addition of heterodyne detection. This work is motivated by the observation that the sensitivity of FRM depends in part on applied optical power. While increasing optical power can enhance measurement sensitivity, it can also damage the sensing media. For example, nanoparticle-doped polymers can become permanently damaged. The first part of this chapter addresses this limitation by introducing a non-common-path heterodyne detection scheme that reduces optical illumination power without loss of sensitivity. Experimental results demonstrate excellent performance when used in an organic thin-film FRM magnetometer: this heterodyne detection scheme achieves results approximately 1dB above the shot-noise limit with 568 $\mathrm{nT}/\sqrt{\mathrm{Hz}}$ sensitivity. This is, to the best of our knowledge, the best sensitivity achieved with thin-film materials.

After optimizing the performance of the heterodyne system we were presented with a choice of pursuing experimental results of imaging or chasing enhanced sensitivity. We chose to then extend the boundaries of conventional approaches by proposing an advanced signal processing scheme, termed Dual Balanced Heterodyne Detection (DBHD). This method transforms the signal response from a quadratic dependence on the magnetic field to a linear dependence, we hypothesized that this could significantly enhance the potential sensitivity to 100 $\mathrm{pT}/\sqrt{\mathrm{Hz}}$. After extensive experimental and theory, work we found that the noise scaling of the DBHD system created a nonlinear noise

scaling term that produced results that were comparable to the conventional heterodyne detection scheme.

4.2 Balanced Heterodyne Detection

4.2.1 Introduction

Magnetic field sensing, specifically imaging has found numerous applications from aerospace, physics, and medicine [132–135]. In the examples stated, magnetic field imaging devices have historically had a trade-off between the sensitivity and transducer size [133, 135]. Where sensitivity is a measurement of the minimum detectable magnetic field. It follows that Magnetic field imaging systems with increased transducer sizes will have worse imaging resolution. Moreover, magnetic field imaging techniques that operate effectively at room temperature and within the Earth's ambient magnetic field are particularly advantageous, as they eliminate the need for magnetic shielding, thereby simplifying the transducer design and reducing its overall size and complexity.

Nitrogen vacancy (NV) centers represent the state-of-the-art high sensitivity magnetic imaging modality [132, 133, 136]. Where all of the imaging techniques mentioned in the previous paragraph have been conducted using NV-centers [132, 134, 137, 138]. The measured sensitivity of optical resolution (on the order of 1 μm) limited NV magnetometers is on the order of $\mu\mathrm{T}/\sqrt{\mathrm{Hz}}$ [136, 139, 140]. NV-center magnetometry is nearing a fundamental sensitivity limit imposed by constraints on NV-center density. Specifically, there exists an upper limit to NV-center density beyond which performance is adversely affected [136]. This subject is well known [133] where large ensemble style NV centers can produce upwards of 10 $\mathrm{pT}/\sqrt{\mathrm{Hz}}$ sensitivity [141–143]. On the other end of the resolution spectrum single NV-centers can be illuminated in an atomic force microscope (AFM) tip providing nanometer scale resolution also with $\mu\mathrm{T}/\sqrt{\mathrm{Hz}}$ sensitivity but at cryogenic temperatures [133].

In contrast, we propose enhancements to Faraday rotation magnetometry (FRM) as an alternative magnetic sensing technique, that leverages optical readout to maximize resolution potential.

The principle behind FRM is the detection of Faraday Rotation, which is a physical effect that describes rotation of the polarization around the propagation axis [97, 144]. When dealing with linearly polarized light, the amount of rotation is given by the expression

$$\Delta\theta = VBL, \tag{4.1}$$

where $\Delta\theta$ is the change in the angle of polarization, V an empirically derived material property known as the Verdet constant, B is the magnetic field perpendicular to the optical axis and L is the path length of the optical interaction with the Faraday rotator material.

In FRM, the magnetic field sensitivity is proportional to the total optical power measured at the detector [145]. Unlike NV-centers, the read-out laser spot size does not affect the sensitivity, making FRM ideal for high resolution imaging applications. The challenge of implementing high-sensitivity FRM is finding suitable transducer materials that produce high Verdet constants with low optical loss. The material of choice for sensing applications has historically been rare-earth element doped Yttrium Iron Garnet (YIG) [146]. Though YIG requires sub-micrometer thick layer to produce a linear response to magnetic fields. As an alternative, a new class of materials that Verdet constants as high as 5.8×10^5 $^\circ/(\mathrm{m} \cdot \mathrm{T})$ have been developed for NIR illumination [7, 20–22, 147]. These materials leverage nanoparticles embedded in polymers. The benefit of this is that the nanocomposite can be fabricated into 10's of microns thick polymer films. This will produce more Faraday rotation and thus a higher potential for sensitivity when compared to thin-film YIG. Another key benefit of FRM is that the materials work at room temperature and experience magnetic saturation above 5mT which enables them to be used in unshielded environments exposed to the native-earth magnetic field.

As the sensitivity is coupled to optical power on the transducer material, it is desirable to put as much optical power on the sample as possible. This creates a thermal issues for both polymer nanocomposites as well as YIG. The polymer host materials suffers from a low optical damage threshold. While YIG has the potential to become thermally demagnetized. As a solution we

first considered a non-common path heterodyne configuration. This enables a significant amount of the light to bypass the sample and increase sensitivity without contributing to sample heating. Optical heterodyning is a common technique used in sensitive optical measurements that provides amplification, and noise reduction to enable shot-noise limited measurements. Heterodyne detection has been successfully implemented for the detection of polarization rotation to produce shot noise limited results [145,148–150]. The use of non-common path heterodyne gain to reduce optical power on the transducer to prevent material damage has not been considered in the literature. The only previous demonstration of magentometry using nanocomposite thin films produced results roughly 20 dB above the shot noise limit, exposing the technical challenges of a non-heterodyne system [20]. Simply adding heterodyne gain to an identical experimental configuration enabled us to get within a few dB of of the shot-noise limit.

While implementing balanced heterodyne detection (BHD) we also realized there is a significantly more sensitive detection scheme for FRM. Inspired by polarization sensitive optical coherence tomography (PS-OCT) to implement a dual balanced heterodyne detection (DBHD) configuration when increases responsivity to small changes in polarization rotation [151]. As will be derived in the next section, this technique will change a normally quadratic measured electrical signal power response from $\Delta P^e \propto B^2$ to $\Delta P^e \propto B$, where P^e is the electrical power and B is the magnetic field. This drastically improved sensitivity to small signals. Experimentally this enhancement does not come for free as it requires additional optical complexity as well as special consideration on the detection electronics. We look to describe both techniques in detail as they are both useful.

In this work, we first created heterodyne polarimeter, which presents the highest sensitivity seen in a organic thin-film FRM magnetometers at 658 $\mathrm{nT}/\sqrt{\mathrm{Hz}}$ without the use flux concentrators. We also present a paradigm shifting dual-balanced non-common path heterodyne magnetometer and measure magnetic fields that greatly expands the sensitivity of this technique. Paving the way for a high sensitivity, unshielded, room temperature magnetometer with higher sensitivity at diffraction limited spot sizes than the state-of-the-art NV-center magnetometers.

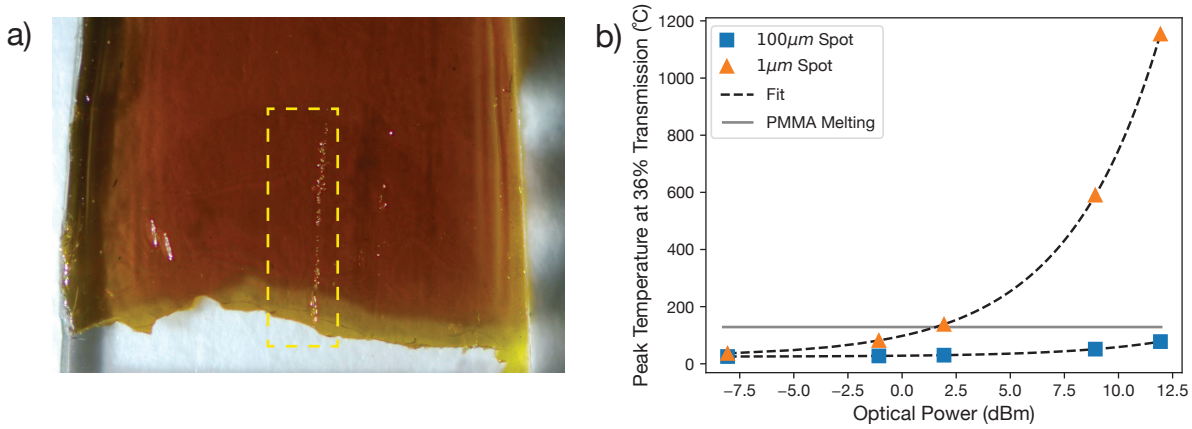

Figure 4.1: a) Line of optical damage created by scanning laser spot on thin-film Faraday rotator. b) Peak thermal temperature simulated in COMSOL simulation modeling our material as a function of optical spot size. Absorption was modeled as a heated cylinder producing heat power equal to the amount of absorbed light, where the radius of the cylinder was defined as the spot size, the thickness was equal to our thin film, the glass substrate was included in the modeling.

4.2.2 Methods

The Verdet constant V from Eqn. 4.1 plays a key role in determining measurement sensitivity. Recent studies have explored both complex organic compounds and inorganic crystal nanoparticles and provided 2 orders of magnetite enhancement in Verdet constant [7,97,147]. In this work, we use Tb^{3+}-doped magnetite (Fe_3O_4) nanoparticles embedded in a polymethyl methacrylate (PMMA) polymer. The Faraday active thin film material specifically used in the system was a 35 µm thick PMMA thin film nanocomposite made of 4 wt.% loading, 17 nm magnetite nanoparticles doped with 1.5 mol% Tb^{3+}. The Verdet constant was measured to be 1.15×10^5 °/(m·T) at 1064 nm. This is lower than our previously measured value, likely due to age-related oxidation of the sample [152].

The polymer nanocomposite films have a low damage threshold because optical absorption in the magnetite nanoparticles heats and eventual melts the PMMA host as seen in Fig. 4.1(a). YIG thin-films potentially suffer from a similar heating issue where the demagnetization temperature (Curie point) is around 290 $°C$ [153]. Thus, YIG is slightly more resilient, but not immune to optical heating degradation of performance. In Fig. 4.1(b) We model the thermal performance of the nanocomposite in COMSOL. Using a 35 μm thick PMMA sheet on top of glass, we model two

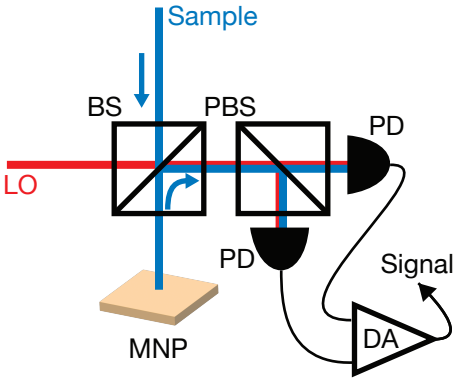

Figure 4.2: Basic non-common path heterodyne configuration used for the detection of polarization rotation. film MNP: Magnetite nanoparticle film, LO: local oscillator, PBS: polarization beam-splitter, PD: photodetector, DA differential amplifier.

laser spot sizes as cylindrical heat sources with a fixed heat power. We find that the reaches the PMMA melting point at approximately 2.5 dBm of illumination power with a 1 μm laser spot, which corresponds to 2 kW/cm^2 of intensity. This value matched well with the experimentally observed damage threshold.

The complete experimental apparatus is similar enough to what was demonstrated in [154], we will focus on describing the detection side. Light is produced by a 80 kHz linewidth, 1064 nm fiber laser [NKT Koheras AdjustiK Y10]. The LO and sample arm beams are generated in a free-space acoustooptic frequency shifter (AOFS) with a frequency difference of 85 MHz. The light is then delivered to the detection schemes described in Fig. 4.2 using polarization maintaining fiber. It is possible to observe the balanced heterodyne schematic in Fig. 4.2. The sample light double passes through the MNP film and then passes through a BS which acts as an optical high-loss circulator. The light passes through a PBS where it is split into the polarization components. The reference (LO) passes through the BS and is also split into polarization components. The sample and LO mix on a photodetector to produce a heterodyne tone. The tones are subtracted from each other in the internal differential amplifier of the balanced detector. This serves to reduce the noise and amplify signals created by polarization modulation. We work through the sensitivity of the

system below:

$$V_{het}(t,\theta) = 2RT_g\sqrt{P_r P_s \cos^2(\theta)}\cos(\Delta\omega t) \tag{4.2}$$

The heterodyne signal is an AC sine wave with an amplitude determined by the optical power in the sample (P_s) and reference (LO) (P_r). The $\cos(\Delta\omega t)$ represents the term created by the frequency difference between the sample and LO. When using balanced photo-detection to reduce noise and dynamic range requirements. The voltage from the balanced heterodyne configuration is as follows:

$$V_{BHD}(\Delta\theta) = 2RT_g\sqrt{\frac{P_r}{2}P_s}\left(\sqrt{\cos^2(\theta)} - \sqrt{\sin^2(\theta)}\right). \tag{4.3}$$

P_r is divided by two to correspond to the total reference power incident on the PBS. P_s will also eventually divided by two in the $\cos^2$ term. In power terms we simplify:

$$P_{BHD}(\Delta\theta) = 2k\sin^2(\Delta\theta) \approx 2k\Delta\theta^2. \tag{4.4}$$

Where k is defined as follows, adding an additional term η_{het} which represents the heterodyne efficiency which was measured to be 85%:

$$k = \frac{R^2T_g^2P_rP_s\eta_{het}^2}{\Omega}, \tag{4.5}$$

4.2.3 Example Signal

An example of the heterodyne tone can be found in Fig. 4.3. Here, we can gain an understanding of how the signal is formed and measured in practice. Starting from the lowest power (lowest noise), we first observe the noise floor of the measurement device, which is represented by the black line.

Next, we observe the blue line, which corresponds to the detector noise. With just a single laser beam incident on the detector, we find that the laser has no significant noise contributions at

85 MHz. Once both lasers (sample and LO) are active, the heterodyne tone appears. We find that the beating introduces minimal additional noise.

The last key feature is the magnetic signal, which is encoded as an amplitude modulation of the 85 MHz peak. This modulation manifests as sidebands to the actual signal. By measuring the height of the sidebands, we can determine the magnetic field.

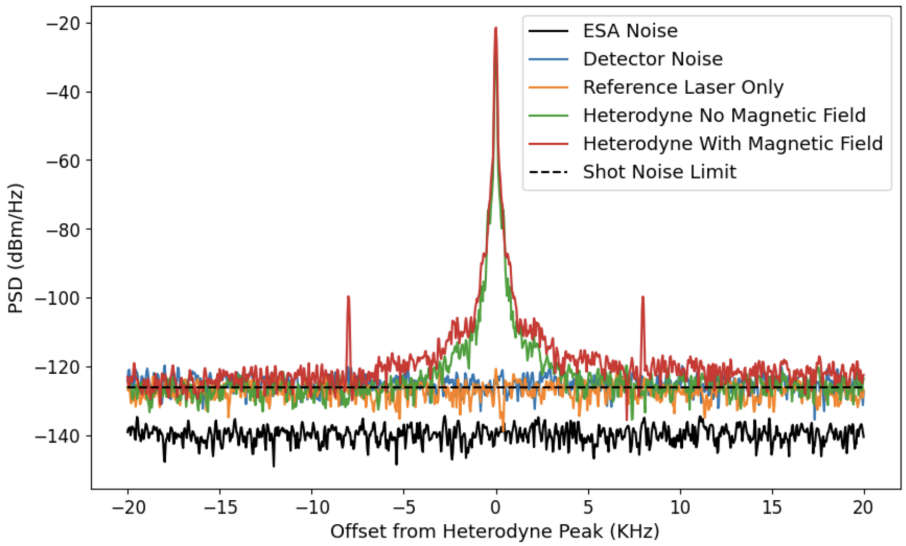

Figure 4.3: Power spectral density of heterodyne tone created by system with and without magnetic fields. Magnetic signal is encoded in sidebands at +- 8 kHz away from the central peak. Magnetic field is approximately 75 μT at 8 kHz AC modulation. Shot noise limit defined mathematically based on applied optical power.

4.2.4 Sensitivity

To calculate the sensitivity we establish a model for the signal-to-noise ratio.

$$SNR = \frac{P_s^e}{P_n^e}, \tag{4.6}$$

where P_s^e is the electrical signal power and P_n^e is the noise power. The noise power will be defined more rigorously in the following section, but it follows the form where we will estimate the power spectral density (PSD) of the noise this must be multiplied by the bandwidth Δf of the measurement,

$$P_n = PSD_n \times \Delta f. \tag{4.7}$$

We need to define how all the parameters affect the signal-to-noise ratio (SNR). We can mostly simply achieve this by calculating the noise equivalent polarization rotation angle $\Delta\theta_{NEA}$.

$$\Delta\theta_{NEA} = \sqrt{\frac{PSD_n \Delta f}{k}}, \tag{4.8}$$

Which can be converted to an integration normalized sensitivity by diving by the bandwidth:

$$\frac{\Delta\theta_{NEA}}{\sqrt{\Delta f}} = \sqrt{\frac{PSD_n}{k}}, \tag{4.9}$$

This defines our minimum detectable field by substituting the equation for Faraday rotation $\Delta\theta = VBL\frac{\pi}{180}$ in units of radians. For balanced heterodyne detection:

$$B_{min} = \frac{180\sqrt{P_n^e}}{\sqrt{2k}\pi LV}, \tag{4.10}$$

4.2.5 Noise

In a heterodyne magnetometer, there are four primary noise sources: environmental noise, technical noise, laser relative intensity noise (RIN), and optical shot noise. When discussing the noise of the system we normalize to the power spectral density (PSD) of the electronic signal in units of W/Hz. The SNR of the system is defined as

$$SNR = \frac{P^e_{\text{signal}}}{\Sigma P^e_{\text{noise}}} = \frac{P^e_{\text{signal}}}{P_{\text{Tech}} + \frac{P_{\text{IN}}}{CMRR} + P_{\text{shot}}}, \tag{4.11}$$

We can start defining noise by considering laser intensity noise (IN): $IN = RIN^2 \times P_{opt}$ of the laser will dominate at higher optical powers, but can optimally be removed by using the common mode rejection ratio (CMRR) of the balanced detector. The laser RIN noise is quoted by the manufacturer to be -120 dBc/Hz Intensity noise is defined as follows:

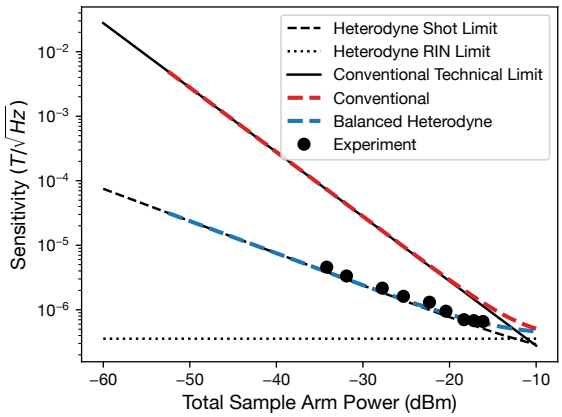

Figure 4.4: a) Experimental validation of predicted SNR as a function of sample power with fixed $1.2mW$ total LO. Magnetic field sensitivity given measured SNR, considering 35 μM thick nanocomposite thin-film with 1.15×10^5 °/(m · T) Verdet constant. Higher optical powers were not considered as they would be beyond the damage threshold of the material.

$$PSD_{IN} = \frac{P_{sig} P_{Ref} RIN\ T_g^2 R^2}{\Omega}. \tag{4.12}$$

Shot noise represents is the quantum limit of our measurement. Shot noise arises from a temporal distribution in the arrival time of photons. This noise cannot be removed by balanced detection. Shot noise is defined as follows:

$$PSD_{shot} = \frac{2T_g^2 qR(P_{sig} + P_{Ref})}{\Omega}. \tag{4.13}$$

Technical noise represents the two sources of electrical noise in the system. The first source is the data acquisition system (DAC). Our DAC (Liquid Instruments Moku Pro) has a noise floor of -140 dBm/Hz for an input range of 400 mVpp. The second source of electronic noise is the balanced detector [Thorlabs PBD435C] which we measure to be -135 dBm/Hz, defining the electronic noise floor.

4.2.6 Results

Validating the sensitivity, we begin considering a theoretical signal without heterodyne amplification, red line 4.4. We see that the signal is limited by technical noise until the sample arm power begins to encroach on the damage threshold of the material. The presents an opportunity for balanced heterodyne configuration blue line 4.4. The heterodyne gain of the signal amplifies the signal above the electrical noise where the signal is ¡2 dB above the shot noise limit. We validated the performance of the heterodyne system and determined the shot noise limited sensitivity to be 658 $\mathrm{nT}/\sqrt{\mathrm{Hz}}$ the best demonstrated in the literature for thin-film nanocomposite based magnetometers.

4.2.7 Conclusion

Heterodyne detection enables us to reduce applied optical power reducing thermal issues related to high optical intensity in FRM transducers. The experiments were performed at room temperature, and within the native earth field. Additionally, if fresh thin films were used, a Verdet constant of $5.6 \times 10^5\ ^\circ/(\mathrm{m} \cdot \mathrm{T})$ could be achieved. We look to leverage the high sensitivity to reduce acquisition time in magnetic field imaging systems, enabling higher frame-rates enabling the study of dynamic systems such cells or time dependent circuit dynamics.

4.3 Dual Balanced Heterodyne Detection

The story of dual balanced heterodyne detection (DBHD) started by asking the question if the signal could be encoded linearly proportional to the magnetic field. This is in direct contrast to the BHD case where the signal is quadratically related to the magnetic field. Where Eqn. 4.4 gave us the signal power response of the balanced heterodyne system as a function of θ^2 a linear system would be able to give us a signal power response θ. This would massively amplify the amount of signal that is produced for small magnetic fields, where the quadratic scaling of BHD is detrimental. The configuration draws heavily from the work in the field of polarization sensitive

OCT (PS-OCT), to achieve the sensitivity required for biological images [151].

To validate the signal response of the dual balanced configuration is linear. I compare the signal formation to the balance heterodyne case. In balanced heterodyne, the signal is formed by the difference in optical power between the two ports of the balanced detector. The key difference is that we build a DBHD system to respond to the difference of electrical power P^e which is proportional to the optical power squared P_{opt}^2.

4.3.1 Schematic

We can compare the DBHD schematic to the BHD schematic in Fig. 4.5. Whereas the BHD system splits the polarization components and takes the difference on a single balanced detector, the DBHD system uses a non-polarizing BS to first split the signal in half. Then, each of those beams is split again by a PBS. This leaves us with two beams carrying the $\hat{s}$ polarized signal and two beams with the $\hat{p}$ polarized signal.

Next, the beams are fiber-coupled and then directed onto balanced photodetectors such that the same polarizations are incident on different ports of the balanced detector. Due to the difference in reflections in the optical path, heterodyne beatnotes produced by the two coupled photodetectors for a single polarization are π out of phase with each other. When the differential signal is taken, this has the effect of doubling the amplitude of the signal. This serves to minimize wasted optical signal and provide a doubling of the signal power.

To perform the subtraction, the heterodyne tones corresponding to both polarizations are simultaneously acquired on two channels of a data acquisition (DAQ) system (Alazar 9371) with 12-bit resolution at 1 Gsps. Here, digital in-phase quadrature (IQ) demodulation is performed to extract the instantaneous signal power, which can then be digitally subtracted from the other polarization electrical power to produce the DBHD signal. Further discussion of the signal processing can be found in Sec. 4.3.2.

In summary, we can look at the response of the BHD system to be as follows:

$$P^{e}_{BHD} \propto \left(P_{\hat{s}} - P_{\hat{s}}\right)^2 . \tag{4.14}$$

Where P^{e}_{BHD} is the electrical power produced by the system and $P_{\hat{s}}$ and $P_{\hat{s}}$ are the optical power contained within a polarization component. The DBHD system is slightly different, and measures:

$$P^{e}_{DBHD} \propto \left(P^2_{\hat{s}} - P^2_{\hat{s}}\right) . \tag{4.15}$$

The difference is subtle but plays a key role in defining sensitivity.

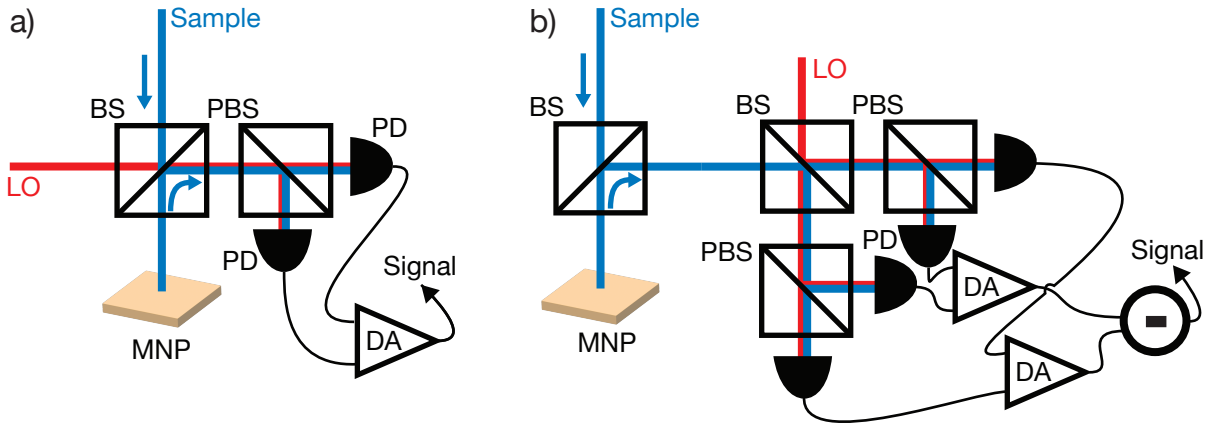

Figure 4.5: a) Basic non-common path heterodyne configuration used for detecting rotated polarization. MNP: Magnetite nanoparticle film, LO: local oscillator, PBS: polarizing beamsplitter, BS: Non-polarizing beamsplitter, PD: photodetector, DA: differential amplifier. b) Dual balanced heterodyne detection scheme.

4.3.2 Signal Acquisition

In BHD, signal acquisition is remarkably straightforward because a low-noise electronic spectrum analyzer (ESA) can be used to directly acquire the signal without requiring any digital signal processing (DSP). This simplicity, however, does not extend to DBHD. Implementing this technique necessitates first determining the instantaneous power of one of the polarization signals to subtract it from the other. This process is challenging because it demands relatively long measurement durations (over 10 ms of acquisition) at high sampling rates to effectively capture the

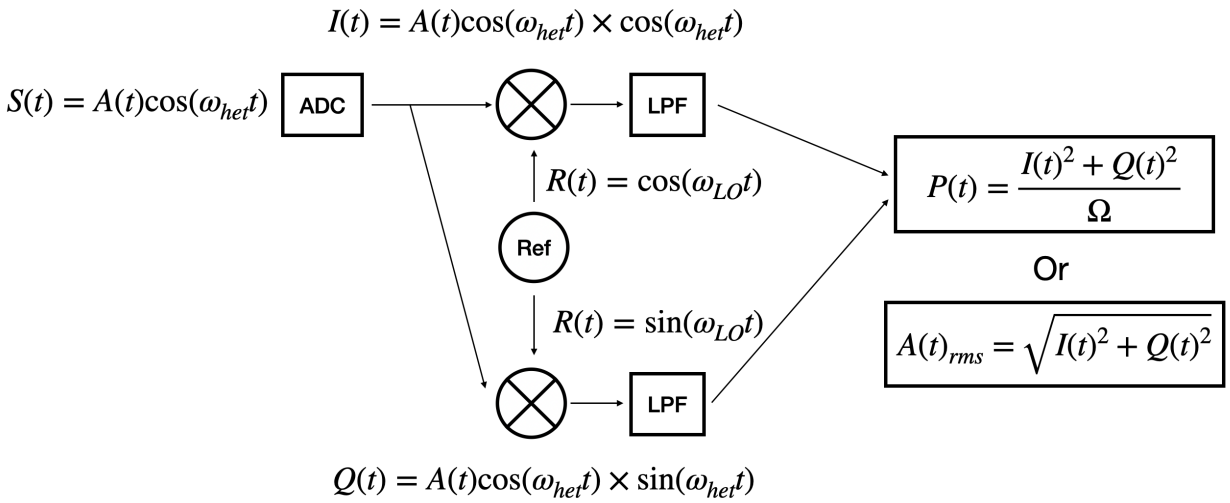

Figure 4.6: Basic block diagram of IQ demodulation scheme, extracting the amplitude of an input cosine with a known amplitude A.

85 MHz beat-note. For this purpose, we employed a DAQ system specifically designed for OCT measurements, capable of sustained sampling at 1 Gsps, limited only by computer memory.

To extract the instantaneous power, we utilize IQ-demodulation, as illustrated in Fig. 4.6. This approach employs a nonlinear heterodyne mixing scheme, analogous to the optical heterodyne method previously discussed, but implemented entirely in the electronic domain. The sample and reference time-domain signals are multiplied, producing a sum-frequency component, which is filtered out using a low-pass filter, and a difference-frequency component, which is retained.

In the special case where the LO frequency matches the heterodyne frequency, the difference signal appears at DC. The multiplication occurs twice: first, the input signal is multiplied by the reference (in-phase) and then by a copy of the reference shifted by $\pi/2$ (quadrature). The signals are subsequently combined in a mean-square fashion to extract the instantaneous power. This scheme is referred to as a superheterodyne receiver, which can demodulate signals regardless of the carrier phase difference between the sample and LO. Superheterodyne receivers are widely used in scenarios requiring demodulation. In laboratory settings, devices that perform this operation are known as lock-in amplifiers. A detailed explanation of their operation can be found in [155].

Though there are lock-in amplifiers available at 85 MHz bandwidth, we did not have any

and decided that the experimental complexity could be greatly reduced without the use of these expensive devices. We were able to achieve comparable results in terms of input noise and dynamic range by using a high quality DAC.

For our acquisition we actually need to perform simultaneous demodulation on two signals at once, we implement this with two digital IQ-demodulators at once, as seen in Fig. 4.7. Here the signals from the balanced detectors are acquired by the DAC, and then run through an IQ demodulator to extract the instantaneous power. The difference is then taken producing our signal of interest.

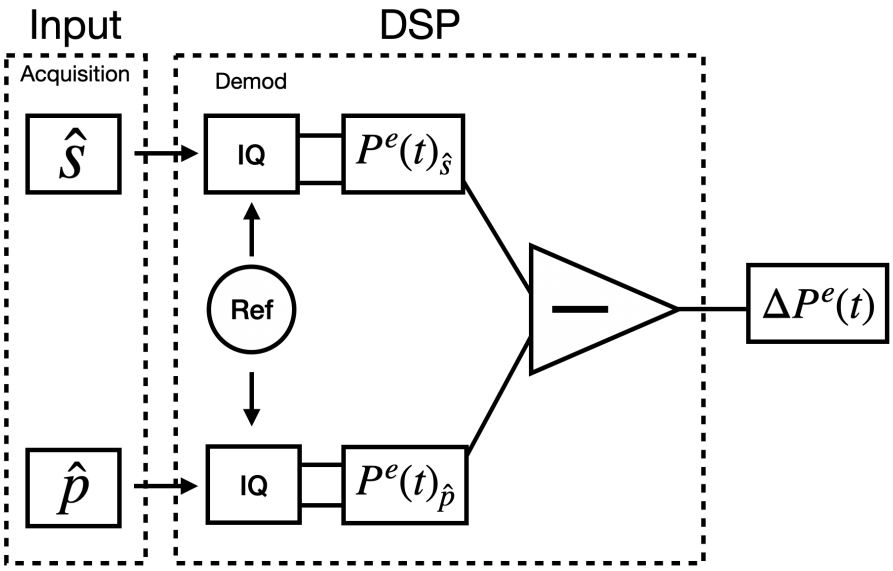

Figure 4.7: Dual IQ-demodulation DSP scheme to get signal from DBHD system. Ref represents digitally generated 85 MHz oscillator, minus sign represents power difference operation.

4.3.3 Signal Derivation

$$P_{DBHD} = P^e_{\hat{s}} - P^e_{\hat{p}} \tag{4.16}$$

We start by getting the heterodyne voltage amplitude on each port is in the form of:

$$V_{\hat{s}} = 2RT_g\sqrt{\frac{P_r}{4}}\sqrt{\frac{P_s}{2}\cos^2(\theta_B + \Delta\theta)}. \tag{4.17}$$

In the DBHD configuration, each polarization is input into its own BD. These signals add constructively in the balanced detector because they are π out of phase, doubling the voltage.

$$V_{BHD} = 4RTg\sqrt{\frac{P_r}{4}}\sqrt{\frac{P_s}{2}\cos^2(\theta_B + \Delta\theta)} \tag{4.18}$$

Converting to power:

$$P_{BHD} = \frac{16RT_g\frac{P_r}{4}\frac{P_s}{2}\cos^2(\theta_B + \Delta\theta)}{2\Omega} = k\cos^2(\theta_B + \Delta\theta)) \tag{4.19}$$

This produces a dual balanced heterodyne expression:

$$P_{DBHD}(\Delta\theta) = k(\cos^2(\theta_B + \Delta\theta) - \sin^2(\theta_B + \Delta\theta)) \tag{4.20}$$

We simplify and approximate for small angles:

$$P_{DBHD}(\Delta\theta) = k\sin(2\Delta\theta) \approx |2k\Delta\theta| \tag{4.21}$$

Thus demonstrating how the response of the signal is linear to angle, which is then linear to magnetic field. This contrasts with the BHD case which is quadratic. We are simply able to calibrate this response with a half wave-plate to change the polarization a known amount, it is possible to see the results of this experiment in Fig. 4.8. Here it is clear to see how the BHD system responds quadratically while the DBHD system responds linearly. Immediately, it is clear that the slope response of the DBHD system is much higher.

.

4.3.4 Noise

We have established that the signal benefits from favorable power scaling, which enhances sensitivity. However, to fully understand the advantages of this system, we must also examine how

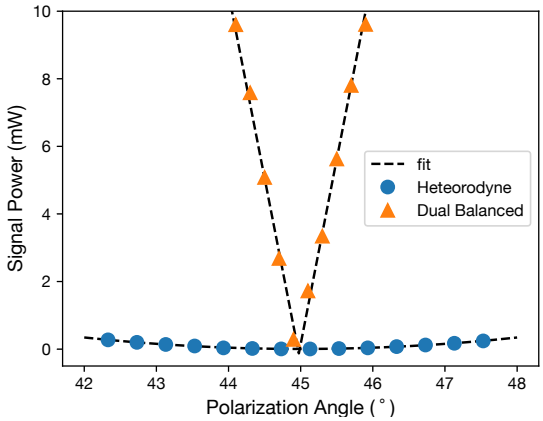

Figure 4.8: Experimental validation of signal electrical power as a function of polarization rotation angle for the balanced heterodyne and dual-balanced configurations. Black line represent quadratic fit for heterodyne case, and absolute value of linear fit for dual balanced. Responses were taken with the same optical power.

the noise scales. The noise sources — such as shot noise and RIN — are the same as those defined in the noise analysis of the BHD measurement.

The key question is: *what happens to the noise when the signal is effectively "square-rooted" compared to the quadratic case considered in BHD?* Intuitively, one might expect the noise to also follow a square-root relationship, resulting in no net gain in sensitivity. My initial attempt to predict the noise behavior suggested that averaging affected the square-rooted noise differently from what was observed in the previous chapter. This led to an extended period of experimental effort aimed at validating our initial prediction of achieving $\mathrm{pT}/\sqrt{\mathrm{Hz}}$ sensitivity. Unfortunately, these experimental attempts were ultimately unsuccessful.

These experimental failures prompted me to revisit the noise analysis more rigorously. In the literature (including my own prior work), noise is often treated with some abstraction, typically represented by variances as we saw in the BHD noise section. My initial hypothesis about noise scaling relied on performing mathematical operations on these abstracted noise terms. This approach was mathematically incorrect and prevented me from observing the correct dynamics.

To arrive at a complete understanding, I needed to consider a more fundamental noise model based on time-domain Gaussian random variables. The full derivation of this model is provided in

Appendix A, but I will cover a few key details here.

First, we model the total photocurrent at the photodiode as a function of time, $i(t)$. The mean photocurrent is $\bar{I}$, and we account for shot noise as an additive term:

$$i(t) = \bar{I} + \sqrt{2q\bar{I}} \cdot n(t),$$

where $n(t)$ is a zero-mean, Gaussian-distributed random variable with unit variance.

When analyzing noise, we typically refer to the power spectral density (PSD) to describe noise power as a function of frequency, $S_i(f)$. This allows us to consider how measurement bandwidth influences noise and helps in evaluating system sensitivity when normalized for integration time.

The PSD is defined as:

$$S_i(f) = \mathrm{F}\{R_{ii}(\tau)\},$$

where R_{ii} is the autocorrelation function of the random variable $n_i(t)$:

$$R_{ii}(\tau) = \langle n_i(t) n_i(t+\tau) \rangle.$$

The angle brackets represent an ensemble average, a concept commonly used in stochastic signal processing to represent infinite averaging.

Skipping the detailed derivation (which is provided in Appendix A), we arrive at the final result for the shot-noise-limited minimum detectable polarization rotation ($\Delta\theta_{min}$), where $SNR(\Delta\theta_{\min}) = 1$. We compare both the BHD and DBHD systems[1] :

Conventional	**Double Balanced**
$SNR_{\Delta V}(\Delta\theta) \propto \frac{\Delta\theta^2 \bar{I}^2}{q\bar{I}}$	$SNR_{\Delta P}(\Delta\theta) \propto \frac{\Delta\theta^2 \bar{I}^4}{q\bar{I}^3}$
$\Delta\theta_{\min} \propto \sqrt{\frac{q}{\bar{I}}}$	$\Delta\theta_{\min} \propto \sqrt{\frac{q}{\bar{I}}}$

This leads us to the unfortunate conclusion that there is no fundamental sensitivity advantage between BHD and DBHD.

[1] Equations are shown in proportional form, as prefactors have been omitted for clarity

4.3.5 Conclusion

This conclusion is disappointing because it means that, even though the signal response may be linear, the contribution of noise is equally strong, resulting in no net improvement in the SNR. Without the addition of analog hardware — which is discussed in the future work section — the DBHD measurement may actually perform worse, as it lacks the analog signal subtraction that is inherent to the balanced detector in the BHD system. This omission causes the measurement to be limited by the dynamic range of the digitization device. I still defend the time spent exploring this approach as worthwhile, because had the DBHD system performed as initially predicted, it could have provided an enhancement in sensitivity of up to six orders of magnitude.

There remains, however, a potential benefit in the linearity of the DBHD signal that warrants further investigation. Referring back to Fig. 4.8, we observe that the BHD signal exhibits a quadratic dependence on the bias angle, whereas the DBHD signal remains linear. This implies that, regardless of the polarization bias angle, the DBHD configuration produces a consistent amount of signal power for a given magnetic field. This is not the case for the BHD system when specifically considering signal power. It is noted that the BHD response is linear when considering signal voltage, it becomes quadratic in terms of power. Further exploration is required to determine if there are scenarios in which a linear signal power response is advantageous, such as when measuring signals with an electronic spectrum analyzer (ESA).

Chapter 5

Limitations of Squeezed-Light Enhanced Upconversion in Real Intermediate State Materials

5.1 Abstract

Upconversion nanoparticles (UCNPs) are a promising contrast agent for use in deep tissue biological imaging in the near infrared illumination regime. Conventional organic upconversion fluorescence dyes are not currently available for deep penetrating NIR illumination. The brightness of UCNPs is limited by the small absorption cross-sections when compared to quantum dots and single photon organic dyes limits. This limits image brightness at low illumination powers. In an effort to increase brightness, previous works with two-photon fluorescence organic dyes has shown that using squeezed paired photons (biphotons) can enhance the upconversion efficiency. These dyes have a virtual intermediate state requiring simultaneous absorption of two photons. In an attempt to see if biphoton light can be used to enhance the performance of UCNPs we adapt a rate equation simulation to model conventional and biphoton illumination of Erbium doped UCNPs which have a real intermediate state lifetime. Unlike two-photon dyes we simulate there will only be luminescent enhancement at low illumination powers proportional to the intermediate state lifetime of the material. In Erbium UCNPs the enhancement can be seen below $10/W\text{cm}^2$. Shortening the intermediate state lifetime to the order of μs level would raise the enhancement threshold and make experimental measurements of the enhancement visible at higher illumination powers. However, we find that using squeezed light on UCNPs provides no gain in fluorescent efficiency at practical illumination powers.

In summary, we explored a hypothesis asking if biphoton illumination of UCNPs would increase the brightness for a fixed optical power. We find that there is no enhancement unless the optical power is very weak or the intermediate state lifetime of the material is very short. Although our hypothesis was proven incorrect, it represents a significant amount of work, both experimentally and in simulation, and is therefore included in this thesis.

5.2 Introduction

Infrared illumination at the low water absorption windows has been shown to be the optimal choice for deep tissue imaging [156–159]. This is due to the combination of low-scattering potential and nonexistent tissue auto-florescence [157,160]. In this wavelength range, commonly studied contrast agents are: organic two-photon fluorescent dyes [157, 161, 162], quantum dots [157, 163–165], and up-converting nanoparticles (UCNPs) [166–169]. Though work is being done to develop single-photon pumped organic dyes in this wavelength range, the compounds are not yet widely available [170]. Organic two-photon fluorescent (2PF) dyes have many advantages including aberration free deep tissue focusing [171], and high imaging resolution [171, 172]. The primary limitation with 2PF dyes is that the absorption process is extremely inefficient due to the requirement of near-simultaneous absorption of two photons [171]. The powerful illumination leads to rapid photobleaching of the dye and thermal damage to tissue [161,171]. Quantum dot based contrast agents offer a single photon absorption alternative that can be very bright when compared to 2PF dyes. Complications with quantum dots including design of non-blinking [164,165], and managing potentially toxic composition [163, 173]. UCNPs are typically composed of lanthanide-doped inorganic crystals that exhibit fluorescence via upconversion [166–168]. Yet, one major limitation of UCNPs is that their absorption cross-sections is small, thus fluorescent images captured with tissue safe illumination intensities are significantly dimmer than quantum dots and single-photon fluorescence of organic dyes [174]. UCNP are still many orders of magnitude brighter than 2PF organic dyes and are able to produce detectable fluorescence under tissue-safe CW illumination. To further increase the clinical viability of UCNPs, much attention has been focused on making UCNPs fluorescence

more brightly by modifying their chemical composition [166] and structure [167]. In a novel attempt to improve the performance of UCNPs we examine the influence of illumination with squeezed-light generated paired photons (biphotons). Following inspiration from the field of 2PF dyes, where luminescent enhancement has been demonstrated under biphoton illumination [171,175–180], we look to demonstrate the potential for enhancement in UCNPs. We perform a rate equation simulation to model the efficiency of upconversion fluorescence in UCNPs under conventional and biphoton illumination. Where enhancement in the luminescent efficiency would increase the clinical viability of UCNPs by making them brighter.

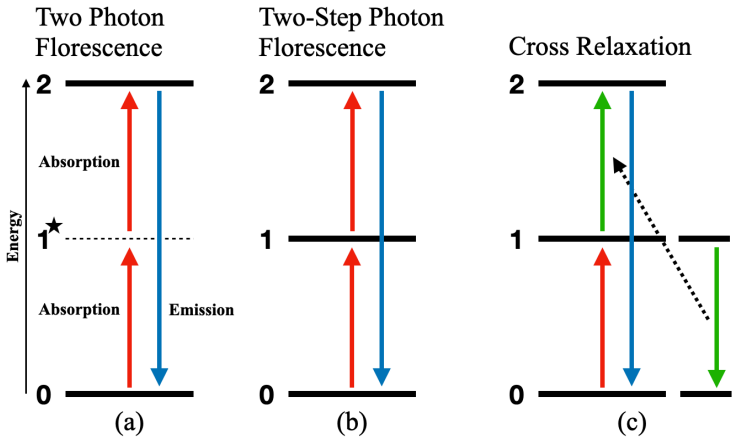

Figure 5.1: A few upconversion mechanisms, (a) two-photon fluorescence with star representing virtual transition, (b) two-step fluorescence, (c) cross relaxation from secondary ion.

The process of fluorescence upconversion converts multiple lower energy photons into a higher energy, shorter wavelength photon. We can categorize three, two photon upconversion processes by their underlying mechanisms as shown in Fig. 5.1. Two-photon fluorescence (2PF) is a nonlinear optical process where the intermediate state is a virtual transition, requiring simultaneous absorption to produce upconversion [161]. This is the primary means of upconversion in organic dyes. The requirement of simultaneous absorption is the reason that biphoton sources have shown luminescent efficiency enhancement over conventional illumination [171, 175–180].

Two-step fluorescence (2SF) is a process where two photons are absorbed sequentially [176]. With a real intermediate state, the electron will statistically remain excited about the period of a

lifetime not requiring simultaneous absorption to produce upconversion. The UCNPs considered in this report will perform upconversion with this mechanism. We expect that performing a pair absorption will ignore the lifetime of the intermediate state and enhance the efficiency at low power. Once sufficient illumination intensity has been reached, the rate of conventional upconversion will overtake the efficiency of the biphoton mediated upconversion.

Upconversion can also be mediated by the excitement of a secondary ion and then energy transfer to an acceptor electron in the intermediate state. This is known as cross relaxation [168, 181], and can be seen in Fig. 5.1. Depending on the dopant concentration, cross relaxation can become a dominant energy transfer process in UCNPs [182].

5.3 Methods

Modeling and predicting key parameters such as transition probabilities, radiative lifetimes, and branching ratios of lanthanide group materials has been well understood for rare earth ions since the 1960s [181–184]. We implement a coupled partial differential rate equation system to model the electron dynamics using the derived parameters as seen in [181–183]. The model considers all the inflows and outflows of election from each discrete energy level of the Er^{3+} ion. We model each of the 6 excited state levels as well as the ground state with a separate equation. The differential equation representing the change in electron population given for each level i is in the form:

$$\frac{dn_i}{dt} = N\sigma_{abs_i} + \frac{N}{2}\sigma_{2SF} - \sum_{j=0}^{i} A[i,j]n_i ... + \sum_{k=i+1}^{6} A[k,i]n_k + NR[i,i-1]n_i - NR[i+1,i] + CR_a n_i n_d - CR_d n_i n_a \quad (5.1)$$

Absorption of photons is handled by the photon flux N and the absorption cross-section σ_i. When applicable, we include the 2SF absorption. Using the Einstein A coefficients we can model the inflows and outflows due to radiative decay, which is scaled by the probability of an electron existing at a specific level n_i. NR corresponds to the nonradiative decay arriving and leaving the

level. Lastly, CR describes cross relaxation pathways between donor (CR_d) and acceptor (CR_a) levels. An abridged version of the model can be seen in Fig. 5.2. We define the probability of each of the events as follows in terms of transitions per ion per second. A description of the common parameters can be found in [181,182,184]. We describe modeling of cross relaxations and a biphoton absorption below.

Parameter	σ_{GSA}	σ_{ESA}	σ_{ESA2}	σ_{2SF}
Value	1×10^{-20}	0.2×10^{-20}	0.8×10^{-20}	2×10^{-41}

Table 5.1: NIR absorption cross sections of Erbium. All values presented in units of [cm^2]. Following Fig. 5.2, σ_{GSA} describes $^4I_{15/2} \rightarrow^4 I_{13/2}$, σ_{ESA} describes $^4I_{13/2} \rightarrow^4 I_{9/2}$, σ_{ESA2} describes $^4I_{9/2} \rightarrow^4 S_{3/2}$

In our model, the key to understanding the luminescent efficiency is to model how electrons populate the specific level $^4I_{11/2}$ in our case. Following Fig.5.2 we can see that the level is populated by conventional absorption, biphoton absorption, and cross relaxation using the fast nonradiative transition between $^4I_{9/2}$ and $^4I_{11/2}$ levels. Each of these pathways has a rate described in (1). To see enhancement, the rate of biphoton absorption must be greater than that of conventional and cross relaxation.

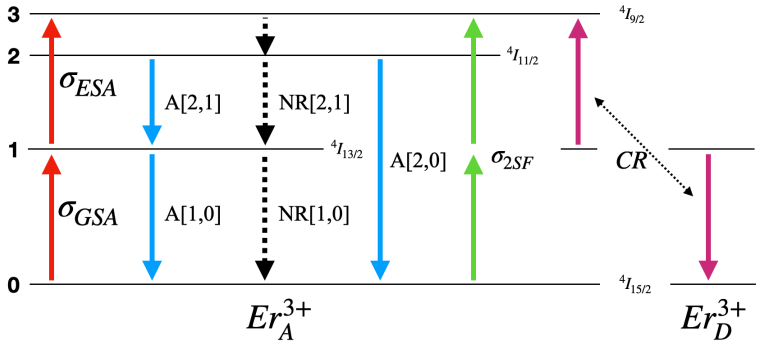

Figure 5.2: Energy level diagram containing key levels of Er^{3+}, The σ represents absorption events including 2SF absorption shown in green, A the given Einstein coefficients. NR represents non-radiative transitions. CR represents cross relaxation between donor ($_D$) and acceptor ($_A$) ions. Higher levels are fully implemented in simulation but are not included in this figure for clarity.

5.3.1 Cross Relaxation

One key effect that must be modeled when working with UCNP particles is multi-ion processes driven by Förster resonance energy transfer (FRET). Depending on the ion species and illumination wavelength, this can become the dominant excitation process known as cross relaxation. As the illumination power increases the inversion of electrons will form complex networks with 100s of possible pathways [182]. The full quantum mechanical picture was first described by Kushida in 1973 [185]. This has been applied many times in the literature, and we will use parameters from the following works [182, 183].

We only need to consider energy transfer effects that are possible in the very weak illumination regime where squeezed light could have an advantage over conventional light. The primary characteristic of this regime is minimal inversion from the ground state into the first excited state ${}^4I_{13/2}$. The only energy transfer pathway available in this condition is the cross-relaxation between ${}^4I_{13/2}$ electrons decaying to the ground state promoting an electron from the same ${}^4I_{13/2}$ state to ${}^4I_{9/2}$ as seen in fig. 5.1. To calculate the probability we define a CR parameter that describes the probability of a transfer happening. This is scaled by the available population in the donor and acceptor states. We use a rate of $15.3s^{-1}$ empirically fitted for a 2% doped Er UCNP [183].

To account for finite Er density, we need to scale to account for the shortened average distance between ions, R. This is done by comparing the probability of FRET, which scales as R^{-6} and the R as a function of doping concentration D. We find that the cross relaxation rate CR scales quadratically to the doping concentration [184]

$$CR' = CR\left(\frac{D'}{D}\right)^2 \tag{5.2}$$

This gives us a transition rate of $2391s^{-1}$ which will become the dominant driving force for excitation into the ${}^4I_{9/2}$ state under 1523 nm illumination. To apply this to the rate equation we use the cross relaxation rate and donor and acceptor population as follows

$$\frac{dn_{i_{\mathrm{cr}}}}{dt} = CR_a n_i n_d - CR_d n_i n_a \tag{5.3}$$

5.3.2 Biphoton Absorption

Biphoton sources, also known as correlated photon pair generators or entangled photon sources, are optical devices that generate pairs of photons. These light sources are based on nonlinear optical processes, such as spontaneous parametric down-conversion or four-wave mixing, which occur in nonlinear crystals, waveguides, or fibers. Most work regarding the absorption of has focused on spontaneous parametric down-conversion (SPDC) sources [175, 176, 178], the challenge with these sources is that they produce output powers at the photon counting levels, making fluorescence measurements difficult, more recent works [171] have used two-mode squeezed light sources that provide much higher illumination powers. We will sweep a range of illumination powers that could be covered with both types of sources.

We need to determine a model to consider absorption probabilities in the form of σ values for the biphoton illumination case. Look at Fig. 5.3 we gain intuition on how the single absorption is handled in the model. For any given illuminated ion, the amount of photons absorbed is determined by the total photon flux density multiplied by the "effective area" of the ion. This meaning any photon that enters the green circle will be absorbed. However, the photon can hit the sample anywhere with in the illuminated area A_{illum}. This giving rise to what is described as the absorption cross-section. Following this logic we will consider the case where we want to know the probability that a single ion will absorb two photons from the biphoton source as something in the form of σ^2.

Since we are considering a real intermediate state we can consider the conventional cross-section and use a combinatorial statistics approach to determine the probability $\mathfrak{p}$ of paired photons are absorbed. This allows us to model an uconversion pathway that fundamentally ignores any effects at the intermediate state.

$$\mathfrak{p}(2SF) = \mathfrak{p}(GSA \cap ESA) \tag{5.4}$$

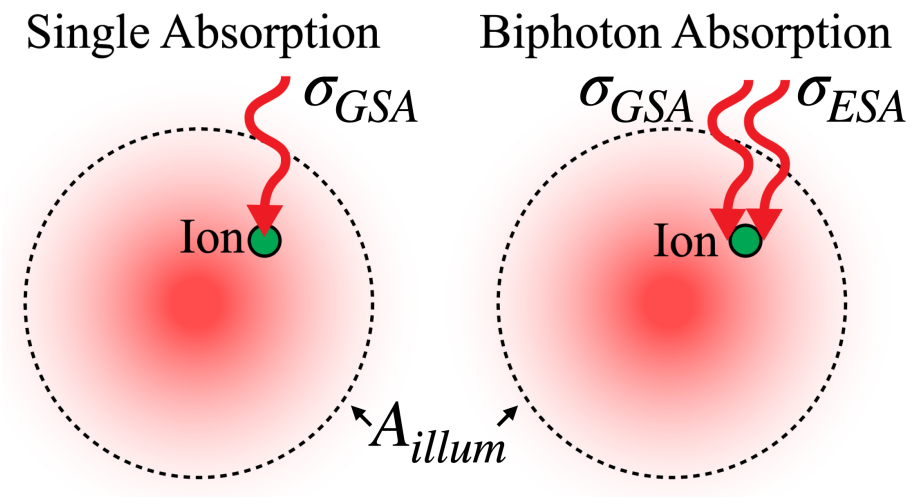

Figure 5.3: Visual representation of how we derive the probability of a biphoton absorption illumination even occurring.

$$\sigma_{2SF} = \sigma_{GSA}\sigma_{ESA} \tag{5.5}$$

With the ground state absorption (GSA) given by σ_{GSA}, excited state absorption (ESA) cross-section σ_{ESA}. In (1) the absorbed photon flux N normalized by 2 to consider paired photons. There is a series of assumptions that must hold true for this cross-section to work. These being, the ground state of the UCNP is full, intermediate state is relatively empty, and the probability of all events is mutually exclusive. Since we expect to see enhancement at low optical intensity, there should be minimal inversion validating the first two assumptions. The probability of absorption of a photon by an Er^{3+} ion is on the order of 10^{-13} which can safely be considered as mutually exclusive.

When simulating the absorption of entangled photons, we need to consider how the photons interact with the materials. We can describe the uncertainty in the photon arrival time and location as a function of the temporal and spatial entanglement.

5.3.2.1 Temporal Photon Correlation

As previously mentioned, certain quantum systems exhibit correlations between photons in both the temporal and spatial domains. Temporal photon correlation describes a state where

the conventional arrival time statistics are broken in favor of paired photon arrival. Depending on the source, the biphotons can be delayed from a few fs up to μs level [176, 186]. Biphoton delay is commonly induced when measuring 2PF absorption to confirm that the effect is caused by entanglement. To model the effects on the 2SF system we can implement delay in the rate equation model by using a scaling factor that is a function of the intermediate state lifetime. This corresponds to the probability that an absorbed photon will remain in the excited state when the subsequent photon is absorbed. The correction is implemented as follows. With T_e corresponding to the average photon delay, and τ corresponding to the intermediate state lifetime.

$$\sigma_{2SF} = \sigma_{GSA}\sigma_{ESA}e^{-T_e/\tau} \tag{5.6}$$

This scaling preserves implementation of the rate equation simulation without needing to add Monte Carlo elements and preserves the simulation efficiency. In addition, we make the assumption that the statistical distribution of photon pair delay is much smaller than the intermediate state lifetime and can be subsequently modeled as a delta function. This is valid for UCNPs but not necessarily true for 2PF systems.

5.3.2.2 Spatial Photon Correlation

Spatial photon correlation explores the statistical relationships between arrival locations of photons. For some sources, the spatial correlation has been well studied [187]. For applications in imaging and therapeutics where the enhancement would be most desirable, a diffraction limited spot size is modeled. At the diffraction limited spot it is impossible to distinguish between lateral positional variations of the photons. If this was possible, significant resolution enhancement past the Abbe diffraction limit would be possible in the single photon regime. The implication of this is that every photon could interact with every ion in the illuminated spot, therefore we do not consider any spatial enhancement of the source. This is accounted for by multiplying the two absorption cross-sections in (5) which models that the two photons are probabilistically absorbed into the same ion. Should a system be used that has spatial correlation on the ion level we would

expect to see an increase in the enhancement gain.

5.3.2.3 Biphoton Purity

Even though the photons are generated as pairs, loss in the delivery optics needs to be minimized to maintain the concentration of biphotons. Attenuation will fractionally reduce the amount of photons that remain paired, thus reverting to a flux with conventional photon statistics. In this simulation we consider a pure biphoton stream. For experimental comparison the predicted threshold should be scaled by the loss on the delivery path.

5.4 Results

The rate equation simulation was performed with values determined from the literature [181, 183]. We will first look to model the UCNPs under conventional illumination, moving next to a simplified biphoton illumination without energy transfer dynamics. We will then explore the implication of energy transfer pathways as well as entanglement delay to complete the model. We are interested in modeling the efficiency of 980 nm generation from 1550 nm illumination which is driven by the ${}^4I_{11/2} \rightarrow {}^4I_{13/2}$ $(2 \rightarrow 0)$ transition. This transition is characterized by a particularly long intermediate state, which exemplifies its use as a laser transition. However, the following approach is general and can be applied to many materials and wavelengths as long as some key parameters are known.

In simulation, we first performed an intensity sweep observing all seven relevant levels of the Er^{3+} ion. In Fig. 5.4 we find that as the illumination intensity increases we find a gradual inversion of electrons into excited states. Where all the electrons start in the ground state and eventually partially fill the first excited state. Then the second energy level is filled. To generalize the dynamic we have sequential filling of the energy levels as the illumination intensity increases.

This provides the first hint that biphoton illumination will have no significant effect on the fluorescent efficiency. This is because the intermediate state has a long relative lifetime and there is some amount of electrons that can be found in this state, even at low illumination powers. If

there is some population of excited state electrons, all that is needed to produce an upconversion attempt is a single absorption event which is not aided by the use of biphoton illumination.

This model allows us to narrow the parameter space by establishing an upper bound on the illumination intensity. Exceeding 10^5 W/cm^2 results in population inversion of the $^4I_{13/2}$ level, shifting the process toward dominance by single-photon absorption, which will see no enhancement under biphoton illumination.

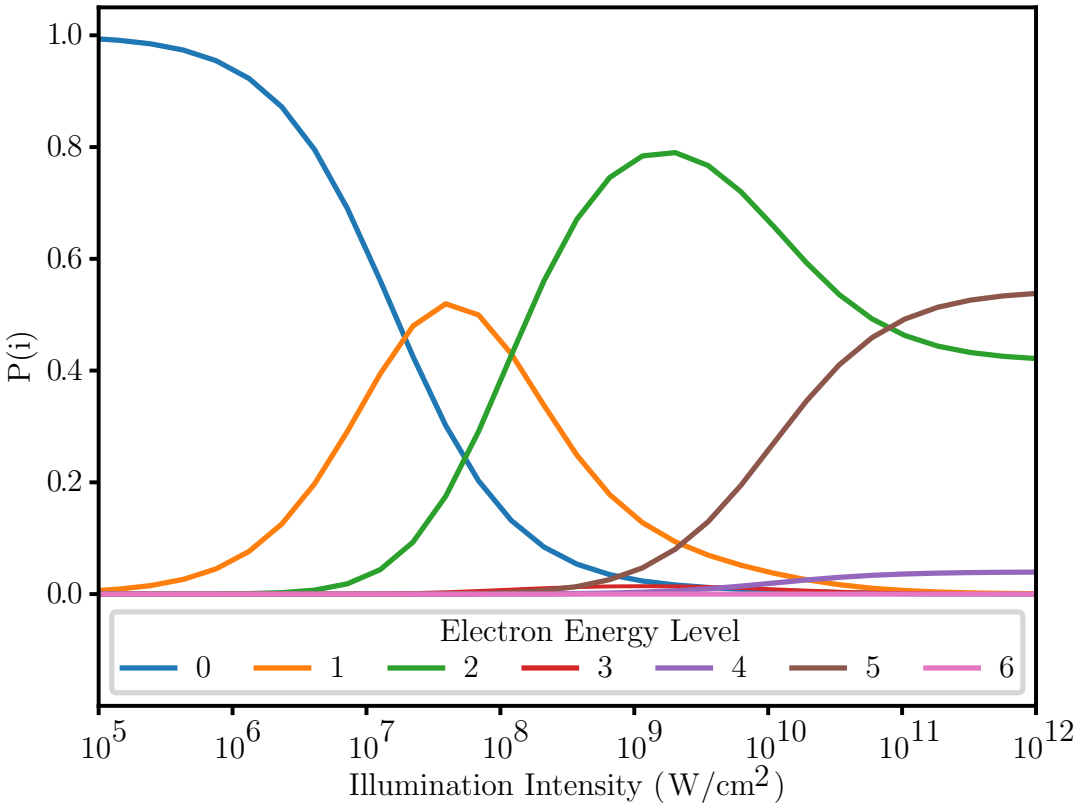

Figure 5.4: Probability distribution of Er^{3+} electron population into different energy levels $P(i)$ as a function of conventional illumination intensity at 1550 nm.

5.4.1 Biphoton Enhancement from Rate Equation modeling

To gain intuition about a potential enhancement region and the factors that control the dynamics, we examine the relevant parameters in detail. We simulate the output fluorescence intensity, which is directly proportional to the probability of an electron existing in level 2 ($P(2)$).

With $A[2,0]$ representing the Einstein coefficient. Thus giving us the luminescent efficiency in the units of per ion luminescence rate $dn_{2_{rad}}/dt$.

$$\frac{dn_{2_{rad}}}{dt} = A[2,0]P(2) \tag{5.7}$$

We again run the rate equation simulation as seen in Fig. 5.4 but only consider the population of $P(2)$ for three different intermediate state lifetimes. The results can be seen in Fig. 5.5. First considering purely conventional illumination (black dotted lines) modeled for three different intermediate state lifetimes, we see a consistent slope efficiency until saturation. The slope remains consistent with varying intermediate state lifetime. The curves become more efficient (shifted to the left) when the lifetime is increased. Considering squeezed illumination (colored lines) we can see luminescent enhancement over conventional illumination at low intensity. This is shown by an increase in output photon flux when the colored line deviates from the dotted black line. Above the inflection point the conventional matches the squeezed illumination suggesting that the biphotons are absorbed with the same statistics as conventional photons. As such biphoton illumination would have no effect on the output power. The illumination intensity of the inflection point decreases with intermediate state lifetime.

The implications of these results are as follows. First, the lifetime of the intermediate state plays a critical role in determining the fluorescence efficiency of real intermediate-state materials. Specifically, the longer an electron remains in the excited state, the greater the probability of undergoing a second excitation to reach the fluorescent emission wavelength. This property is particularly advantageous for upconversion nanoparticles (UCNPs), as they are high-quality materials characterized by long intermediate-state lifetimes.

Second, materials with extended intermediate-state lifetimes exhibit lower inflection points, where biphoton excitation becomes more efficient. This behavior suggests that such materials are inherently more suited for applications requiring enhanced multiphoton processes due to their ability to sustain higher excitation efficiencies at lower energy thresholds.

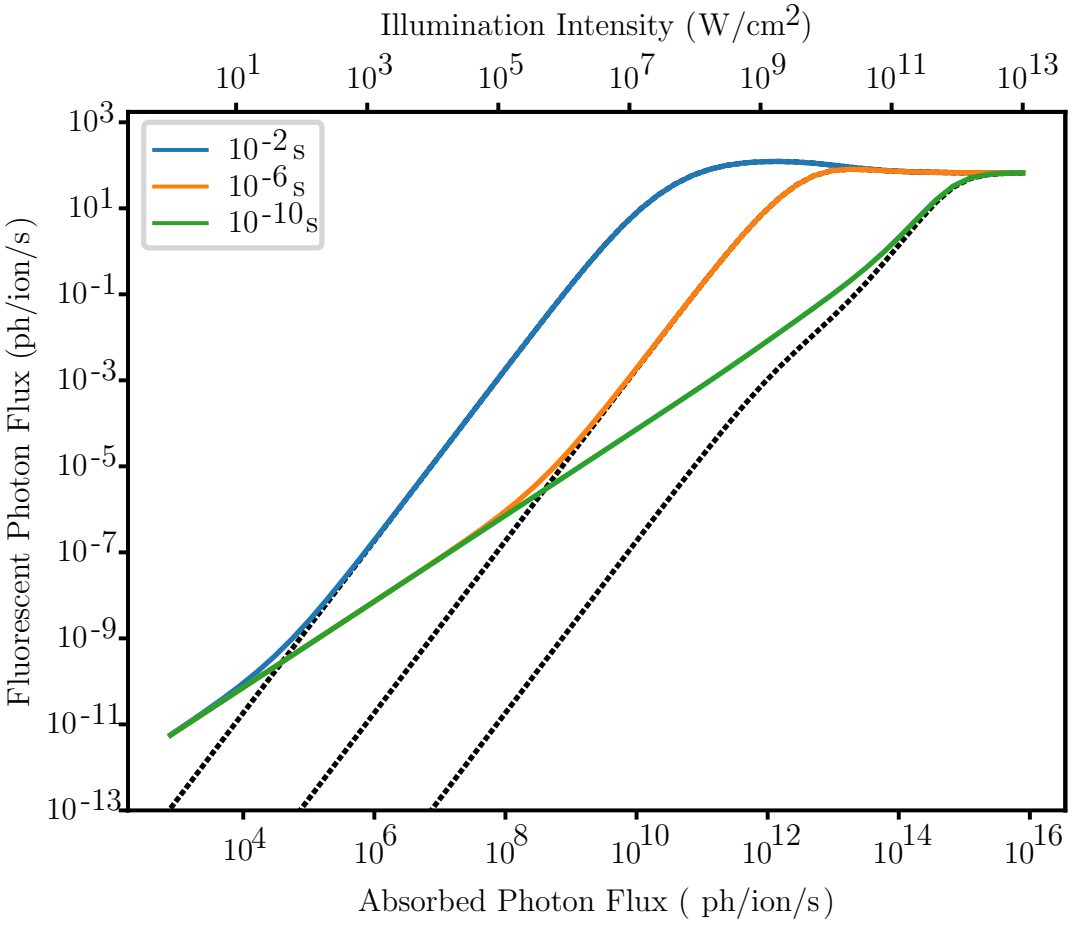

Figure 5.5: a

s a function of illumination power]Output luminescence flux from ${}^4I_{11/2}$ [$n = 2$]. Colored lines correspond to intermediate state lifetime of the ${}^4I_{13/2}$ level under squeezed light illumination. Dotted black lines correspond to conventional illumination with the same intermediate state lifetime as the colored line that is above them.

To build intuition about the dynamics, we can solve a simplified version of the steady state system analytically. We consider a four level [i = 0-3] model (${}^4I_{15/2}$ to ${}^4I_{9/2}$) with an instantaneous decay between ${}^4I_{9/2}$ and ${}^4I_{11/2}$. This is reasonable as we expect to see enhancement when there is little to no population inversion. We additionally do not consider the effects of cross relaxation, which can often be lumped in with the intermediate state lifetime. We find that the rate of conventional upconversion $dn_{2_{conv}}/dt$ as a function of the photon flux N

$$\frac{dn_{2_{conv}}}{dt} = \frac{\sigma_{ESA}\sigma_{GSA}N^2}{A[1,0] + \sigma_{eESA}N}. \tag{5.8}$$

The biphoton enhanced upconversion rate ($dn_{2_{bi}}/dt$) is given by:

$$\frac{dn_{2_{bi}}}{dt} = \sigma_{2SF}\frac{N}{2} = \sigma_{ESA}\sigma_{GSA}\frac{N}{2}. \tag{5.9}$$

When the rates are equal we find the threshold flux where the conventional illumination overtakes the 2SF as given by:

$$N_{th} = \frac{\sigma_{ESA}\sigma_{GSA}}{2\tau_{is}}. \tag{5.10}$$

Drawing conclusions again from both the simulation performed in Fig. 5.5 as well as the analytic expression above. First, there is a threshold where conventional illumination becomes the dominant upconversion process, unlike in virtual state 2PF upconverters, we cannot expect to have enhancement at all illumination intensities [178]. This is not necessarily a problem because deep tissue *in-vivo* imaging operates in the low intensity illumination regime. The second conclusion is that the threshold intensity where the enhancement ceases is only dependent on the intermediate state lifetime. In simulation, we adjust this value to find a region that would be measurable with a physical system. The results from the analytic expression are supported by the modeling results in Fig. 5.6 (Left).

The key limitation of Eqn. 5.10 is that it does not consider cross relaxation, a mechanic where energy is exchanged between neighboring ions in a bulk material. Cross relaxation can significant depending on the system and is particularity strong in highly doped UCNPs with long intermediate state lifetimes [80]. In the next section we model the effects of cross-relaxation, focusing on the impact of the conventional illumination efficiency threshold over biphoton illumination.

5.4.2 Effects of Cross Relaxation on Upconversion Efficiency

Cross relaxation can often play an important role in UCNP energy dynamics [182]. The exact pathways vary between ions and the rates depend on the ion concentration within the nanoparticle. In our case of Eribium UCNPs the key cross relaxation pathway can be seen in Fig 5.2. This pathway is collaborative with the absorption pathway where it excited electrons to the $^4I_{9/2}$ level.

Next we look to expand the model to include energy transfer effects that can be observed in Fig. 5.6. We see a similar inflection dynamic when cross relaxation is added to the model. Looking at conventional illumination. The slope efficiency remains constant, with an increase in luminescent efficiency at the 10^-2s lifetime. This is a result of the collaborative cross relaxation pathway found in erbium. As the intermediate state lifetime decreases the effects of cross-relaxation becomes negligible. When considering squeezed illumination, the increased conventional luminescent efficiency will further lower the threshold for squeezed illumination enhancement. Refining this conclusion we find that cross relaxation does not have a strong effect unless the lifetime is nonphysically short on the order of 10 ms.

The effect of intermediate state lifetime can be more clearly demonstrated in Fig. 5.8. Here we look to generalize the relationship between the intermediate state lifetime and threshold where conventional illumination becomes more efficient. There is a monotonic decrease in the threshold as the intermediate state lifetime decreases. Any region above the line has no benefit from biphoton illumination, and any region below has enhancement.

Previous experimental works with 2PF dyes [171] have shown that the effect can be challenging to measure experimentally due to the low output power of the SPDC sources. In our case, we need to operate in a low power illumination regime to have enhancement, it must be determined if output fluorescence from the enhancement regime is even detectable. This can be achieved by scaling the per ion fluorescent flux by the number of ions illuminated. We assume a spot size radius of $2.5\mu m$ and a depth of field of $1\mu m$, in this volume we illuminate approximately 4×10^{10} Erbium ions. In the right axis of Fig. 5.7 the total output luminescence of the sample can be seen. To see

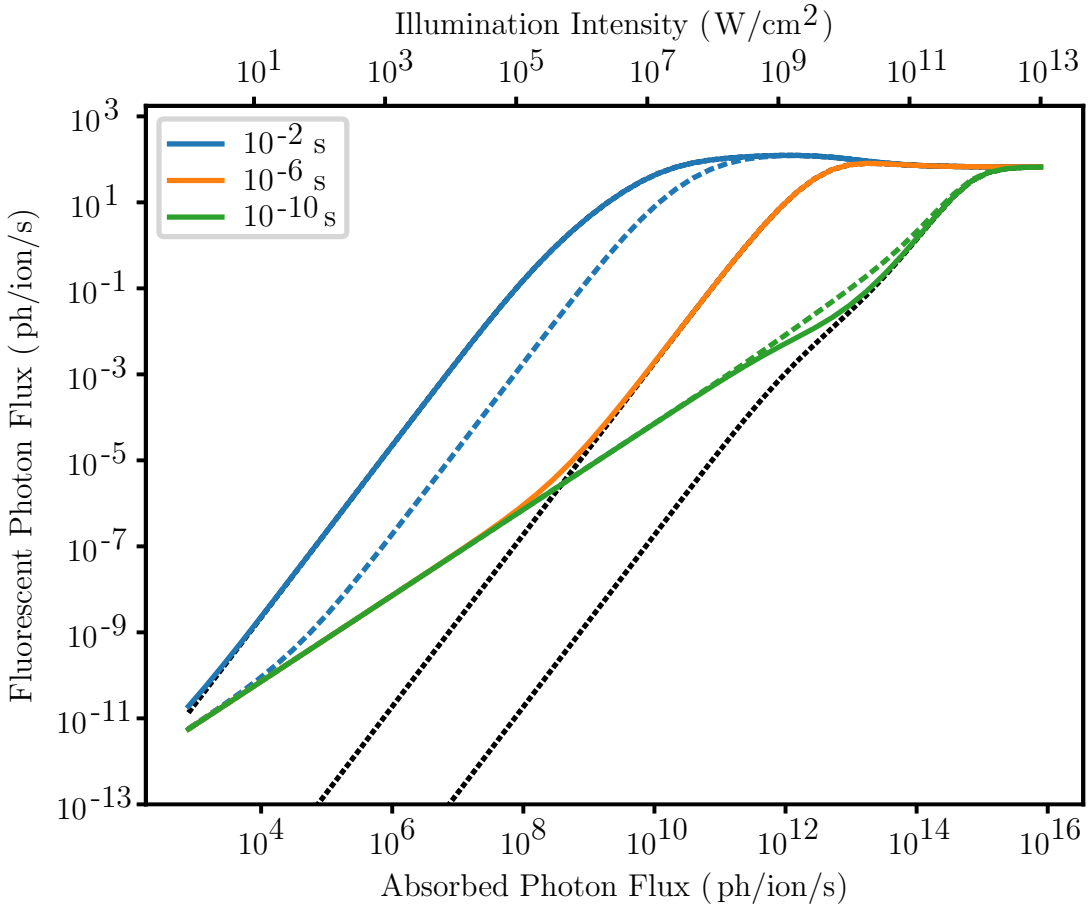

Figure 5.6: Output luminescence flux from ${}^4I_{11/2}$ level in a 25% Erbium UCNP. Solid colored lines correspond to biphoton illumination with cross relaxation. Dashed colored lines correspond to biphoton illumination without cross relaxation. Black dashed lines correspond to conventional illumination with cross relaxation.

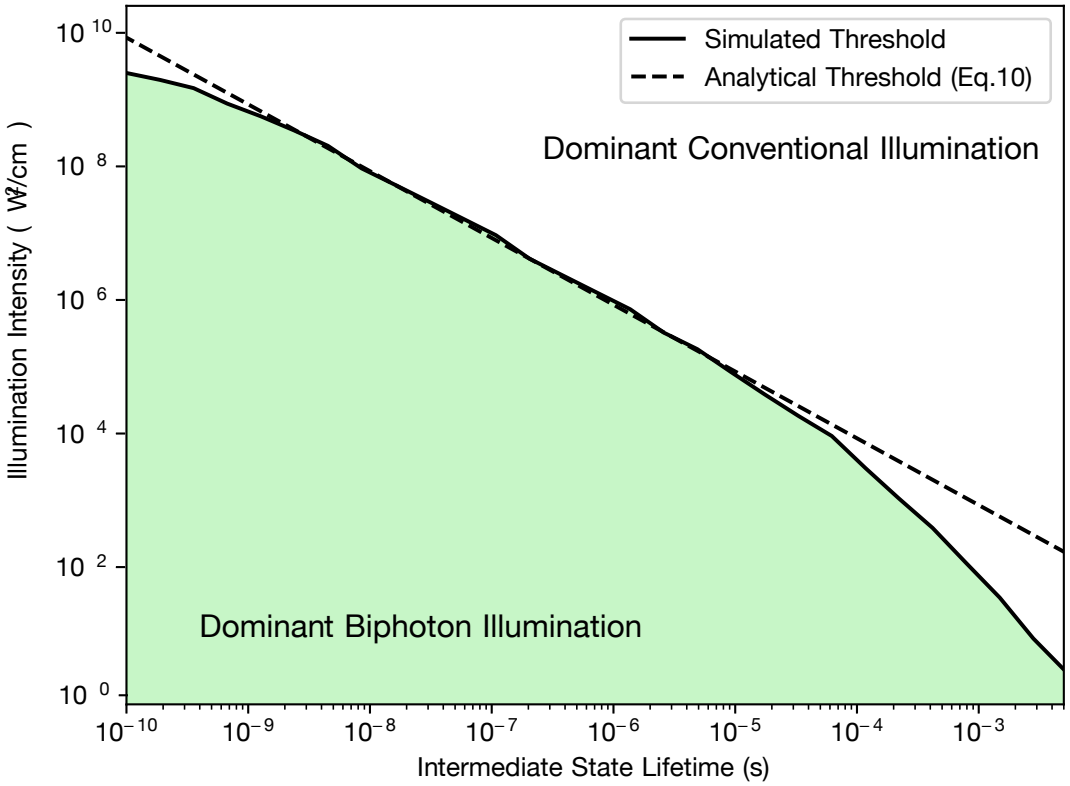

Figure 5.7: Illumination intensity as a function of intermediate state lifetime. Threshold illumination intensity where biphoton light exceeds conventional illumination by 3dB as a function of intermediate state lifetime. Green area corresponds to illumination regime where enhancement is achieved with biphoton light.

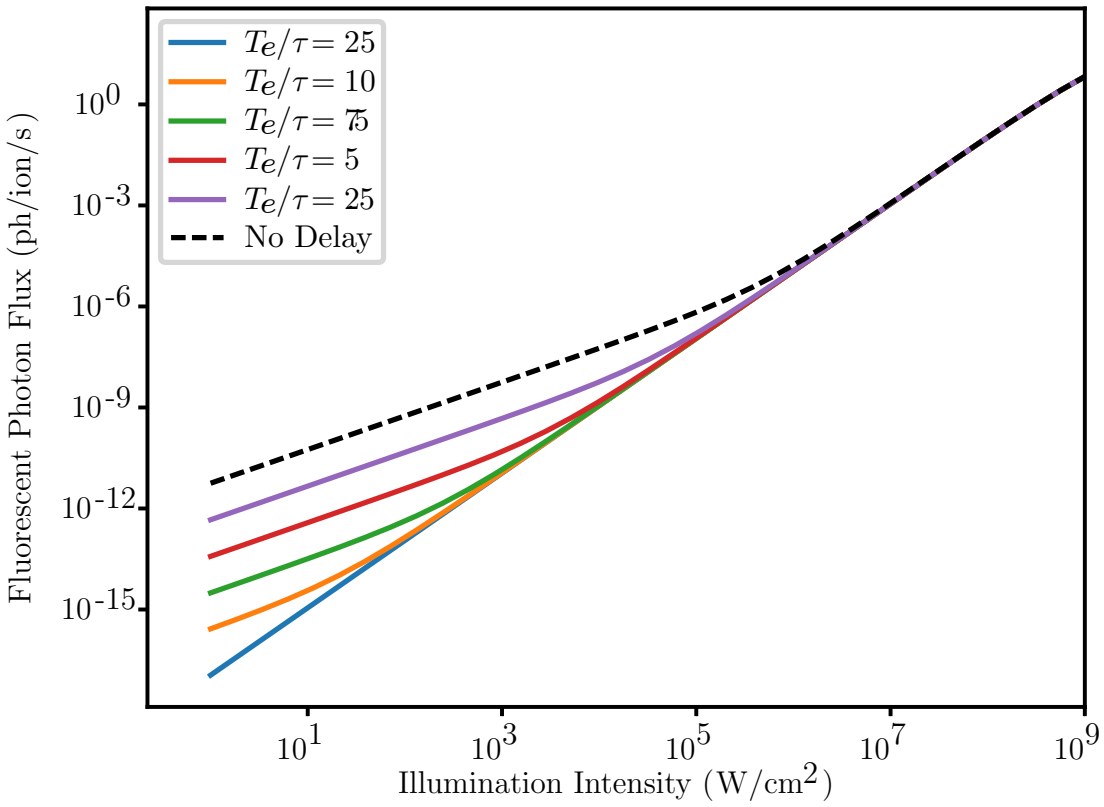

Figure 5.8: Fluorescent photon flux as a function of illumination intensity. Output luminescence flux as a function of photon delay. The delay is normalized to the intermediate state lifetime which is simulated at $1\mu s$.

results experimentally this will need to get scaled by the microscope objective collection efficiency and the probability of photon detection in the detector, which can be conservatively approximated as a 10dB loss from the total efficiency. For Erbium ions that commonly have millisecond intermediate state lifetimes we expect to collect significantly less than 1 photon per second of light, which would make experimental efforts challenging. More reasonable experimental efforts could be had if the intermediate state lifetime was shortened to the μs regime.

We can further generalize the effects of cross relaxation to different concentrations and different active ions. The dominant energy pathways will depend on the relative rates between decay and energy transfer. As the ion concentration is increased the cross relaxation rate will also increase and potentially become dominant. The effects on the squeezed enhancement threshold is dependent on if the pathway is collaborative. If cross relaxation enhances luminescent efficiency the threshold for enhancement will become lower. If instead, the cross relaxation facilitates depopulation of the intermediate state without enhancing upconversion this will raise the enhancement threshold by lowering the effective intermediate state lifetime. This could be used to engineer UCNPs with different active ions that demonstrate squeezed upconversion enhancement outside the single photon regime.

5.4.3 Entanglement Delay

We can also simply consider the delay between biphoton pairs. We normalize the delay by the intermediate state lifetime T_e/τ where T_e is the average photon delay and τ is the intermediate state lifetime. Results can be seen in Fig. 5.8. The induced temporal delay between the photons has the effect of reducing the upconversion efficiency between the bounds of no delay and conventional illumination. In a physical experiment care should be taken that the entangled photon delay is at least on the order of the intermediate state lifetime or lower to optimize the upconversion enhancement.

5.5 Conclusion

We present the first theoretical study on the potential for enhancing the efficiency of UCNPs with real intermediate states by using a biphoton laser source. Unlike virtual state upconverters there is a more delicate balance between conventional and entangled illumination that is driven by the intermediate state lifetime of the material. In a physical system with parameters based on 25% Er doped UCNPs we expect to be able to detect enhancement with a $1\mu s$ intermediate state lifetime. This is challenging to realize experimentally because the required lifetime is too fast for all real lanthanide transitions, it is also much too slow for any virtual transitions. We attempted to shorten the intermediate state lifetime by intentionally oxidizing the UCNPs to induce additional lattice defects. This lowered the intermediate state lifetime to 100s of microseconds which was not sufficient to observe enhancement. In UCNPs, cross relaxation often plays an important role in upconversion pathways, in our case the effect on the enhancement threshold was negligible but would need to be carefully considered in other materials. Lastly, when dealing with biphotons it is important to consider the potential delay between photons. We found that as long the photon delay is at the same order of magnitude as the intermediate state lifetime the efficiency of the process would be preserved.

With knowledge of just a few experimental parameters one could find a suitable real intermediate state upconversion material and simply demonstrate enhancement without the need of virtual state transitions. It is common to implement co-doping UCNPs with Yb and Er. Since Yb has a larger absorption cross-section and strong energy transfer to Er^{3+}. This could be added into the model with the addition of partial differential equations for the available Yb states and energy transfer to Er. We chose not to implement this for our 1523 nm pumping scheme that would require a 2PF absorption to excite the Yb. We hope that since the intermediate states are real, the simpler kinetics will allow for conclusive enhancement if it is found experimentally in the future.

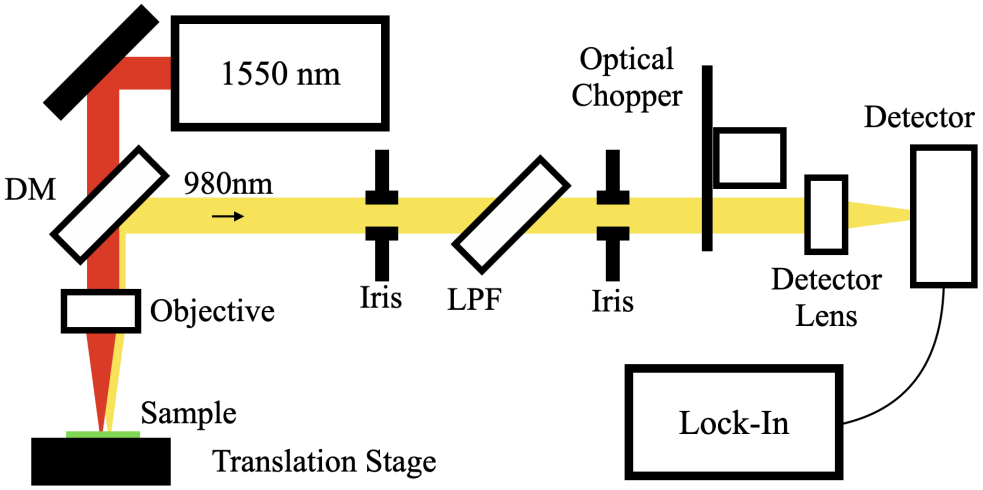

Figure 5.9: Schematic of upconversion fluorescence microscope used to experimentally measure fluorescent efficiency of various samples as well as produce images. DM, dichoric mirror, LPF, long pass optical filter.

5.6 Experimental Work

The simulation work presented above was preceded by experimental efforts that yielded inconclusive results. Nevertheless, I include several snapshots here to demonstrate the successful construction of a fluorescence microscope capable of acquiring confocal images of an upconversion nanoparticle (UCNP) target. The schematic of the optical setup is shown in Fig. 5.9.

In this setup, a dichroic mirror was employed to separate the illumination and detection paths. Two irises were positioned as a confocal gate to improve spatial resolution. An optical chopper, in conjunction with a lock-in detector, was utilized to stabilize measurements and enhance sensitivity, enabling the detection of extremely low levels of collected fluorescent light. To further improve detection sensitivity, a high-gain avalanche photodetector, optimized for femtowatt-level measurements, was employed to measure the output power accurately

We made an imaging target to validate the imaging capability of the system. Using a laser cutter we etched a CU target into a glass microscope slide and filled it with liquid UCNP solution and allowed it to dry. The resulting image is seen in Fig. 5.10.

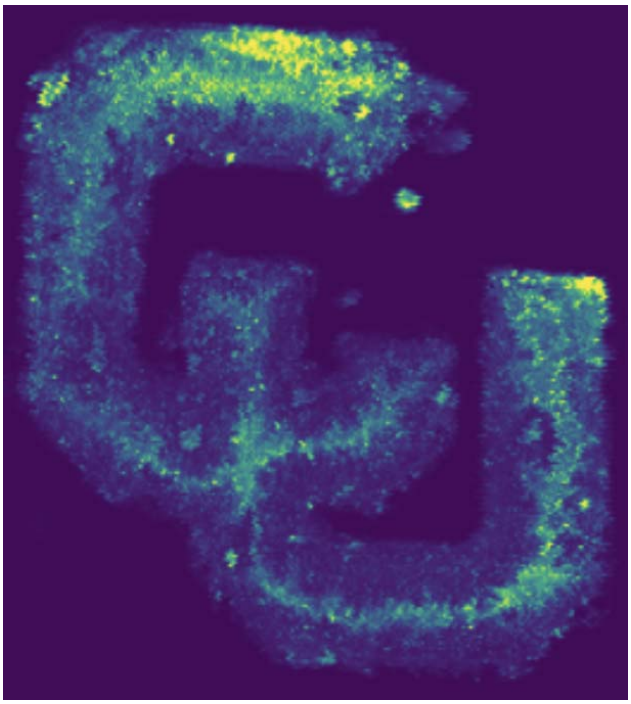

Figure 5.10: Image of CU created by laser etching a microscope slide and filling the well with upconversion nanoparticles and allowing them to dry. The drying process produced a coffee-ring-like effect on the sample, resulting in an uneven distribution of particles. Total width of target was 1 cm.

Chapter 6

Thesis Summary and Future Work

6.1 Thesis summary

From a broad perspective, this thesis demonstrates how nanomaterials can be leveraged to enhance the sensitivity of measurement tools. Specifically, nanoparticles were employed both for magnetic field sensing and for generating upconversion fluorescence. The small size of the nanoparticles enabled the formation of largely defect-free crystals with properties favorable for enhanced sensing. In the case of magnetic field sensing, the particles were more responsive to external magnetic fields, as evidenced by an enhanced Verdet response. Their size also contributed to low optical losses due to reduced scattering and absorption. In terms of fluorescence, the particles exhibited very long intermediate-state lifetimes, making them highly efficient upconverters. For fluorescence microscopy, the UCNPs displayed exceptionally long lifetimes and highly efficient fluorophores. Ultimately the viability of UCNP based flourophores are primarily limited by their small absorption cross-sections.

Nanoparticles cover a broad spectrum of applications beyond those discussed in this thesis, their fabrication can be challenging. The vast parameter space in terms of material composition and structural design underscores the potential for incremental improvements using custom-engineered materials.

6.1.1 Magnetic Field Sensing

Our work on magnetic field sensing was driven by the question of whether sensitivity limits could be decoupled from the size of the transducers. We identified Faraday Rotation Measurement (FRM) as an optimal solution because its sensitivity depends on total optical power rather than intensity. To achieve the sensitivity limits of this technique, we developed a novel material by lightly doping magnetite (Fe_3O_4) nanoparticles with terbium (Tb^{3+}). This process yielded a material that was both more transparent and exhibited a higher Verdet constant than other thin-film Faraday rotators in its class.

Having developed this material, we sought to push the sensitivity of the technique to its theoretical limits. Initially, we increased optical illumination power until the samples began to thermally degrade. To overcome this limitation, we employed a simple balanced heterodyne detection method, allowing us to reduce optical power on the sample while using coherent gain to amplify signals at the detector. This approach enabled shot-noise-limited measurements with a sensitivity of 658 $\mathrm{nT}/\sqrt{\mathrm{Hz}}$, outperforming all other techniques operating at the optical diffraction limit.

Discussions about further improving detection sensitivity led us to investigate a novel detection scheme known as dual-balanced heterodyne detection. This method combines heterodyne gain, higher sensitivity regimes, and common-mode noise rejection into a single system. After careful experimental work we found that our hypothesis that the system would be more sensitive was rejected due to nonlinear noise scaling. The system ultimately only provided approximately the same performance as balanced heterodyne system.

6.1.2 Upconversion Measurements

The second research focus addressed whether the fluorescence efficiency of upconversion nanoparticles could be enhanced using squeezed light. We found that the high quality of the nanoparticles' internal crystal structures produced materials with extremely long intermediate-

state lifetimes. This resulted in highly efficient fluorophores that minimized energy losses through non-radiative transitions. However, these materials underperformed relative to other candidates such as organic two-photon dyes due to their small absorption cross-section.

Simulations of the rate equations governing this system revealed that, due to the intrinsic efficiency of the nanoparticles, they did not benefit from squeezed light unless illumination power was so low as for the output to be practically undetectable. Consequently, we opted not to pursue experimental validation further, ultimately disproving our initial hypothesis. In summary, the nanoparticles were already too efficient to benefit from enhancement through squeezed light.

6.1.3 Broader Reflections

Taking a broader view of this work, the primary conclusion is that nanomaterials and nanoparticles can significantly enhance measurement capabilities. That said, these materials can be challenging to fabricate and maintain. For example, magnetite nanoparticles were prone to oxidation and film degradation over time, presenting reliability challenges.

Beyond material challenges, the sensing process itself proved to be one of the most demanding aspects of this research. Achieving and reproducing sensitivity measurements required meticulous control over a wide range of experimental parameters. Developing a deep understanding of the inner workings of the magnetometer and maintaining consistency in measurements was far from trivial. Nevertheless, these efforts underscore the complexity and potential of nanoparticle-based sensing technologies and highlight avenues for further research and refinement.

6.2 Future Work

My deep study specifically in the field of magnetic field sensing has led me to present a few areas of future work.

6.2.1 Material Enhancement

We chose to use magnetite nanoparticles for our work. The idea of terbium doping emerged from a review of the literature, where rare-earth doping of magnetically active materials is a common practice for enhancing magnetic responsiveness. Our initial studies exploring alternative rare-earth dopants for magnetite nanoparticles did not yield significant enhancements [120]. Nonetheless, there remains a vast array of materials to explore within the polymer nanocomposite framework.

From a speculative perspective, cobalt nanoparticles doped with terbium may represent a promising avenue for achieving even higher Verdet values. More complex ordered structures, such as those presented in [20], which utilized layers of nanoparticles separated by unloaded polymer layers, could also be leveraged to enhance sensitivity.

Additionally, heterodyne detection provides tolerance to high optical losses, minimizing impacts on sensitivity. We had initially considered heavily loaded magnetic nanoparticle thin films with potential Verdet constants exceeding $10^6, ^\circ/(m \cdot T)$. While this approach poses challenges such as increased aggregation and scattering losses, these effects could be compensated for through heterodyne gain.

Finally, renewed efforts on rare-earth doped yttrium iron garnet (YIG) films may also be worthwhile. Both in the form of nanoparticles—previously limited by poor crystal formation—and as doped thin films, these materials are optimized for heterodyne detection and imaging. YIG films have already demonstrated Verdet constants above $10^6, ^\circ/(m \cdot T)$, making them a promising candidate for future work with our high-sensitivity magnetometer.

6.2.2 Analog Readout

Regarding future work with the DBHD project. There is space for enhancement in the analog data acquisition. In the DBHD, the signal is first digitized using a DAC, and then a series of DSP processes are used to extract the signal. For certain applications, it may be more effective to perform the IQ demodulation in analog hardware. This approach would lower the

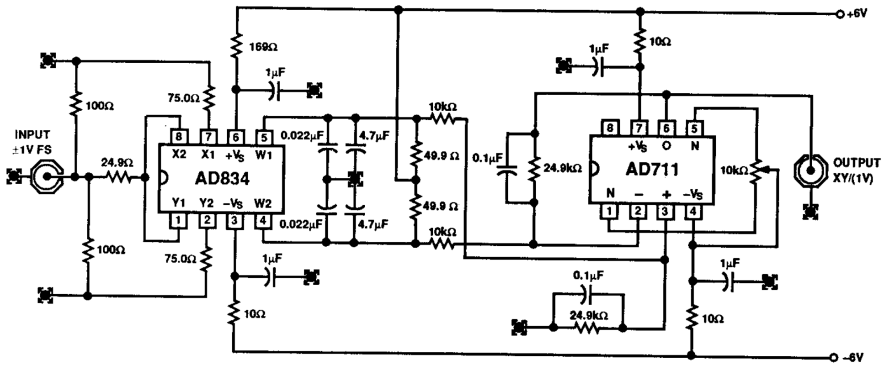

Figure 6.1: Mean-Square measurement device for the AD834 four-quadrant multiplier enabling low-noise analog demodulation up to 500 MHz. Image taken from AD834 application note [1].

sampling rate requirements for the DAC hardware. Currently, data acquisition during magnetic field measurements generates approximately 8 GB/s of data, making long-term sampling impractical.

Since the heterodyne carrier is relatively strong and the signal represents small variations, the primary design challenge revolves around achieving sufficient dynamic range. Ideally, the system should possess approximately 100 dB of dynamic range, which exceeds the capabilities of any integrated circuit (IC)-based demodulation scheme. Furthermore, the linear RF power detectors currently available operate with a maximum dynamic range of 40 dB. Consequently, custom electronic hardware development is necessary.

To address this issue, I identified a circuit architecture capable of enabling low-noise amplitude demodulation with the potential for high dynamic range. The AD834, a four-quadrant multiplier chip, provides a means for low-noise mean-square demodulation of the 85 MHz carrier signal. Following the guidance outlined in the application note, I propose constructing a circuit that adheres to the architecture defined in the application guide (see Fig. 6.1).

I would implement a system as follows. Using an AD834-based mean-square measurement circuit for each channel of the polarization measurement, I would then incorporate an interaction circuit to remove the residual carrier. The signal would subsequently be converted to a DC signal with voltage proportional to the electrical power from each polarization. This output could then be fed into an auto-balancing low-noise differential amplifier (LeCroy DA155A). Such an approach

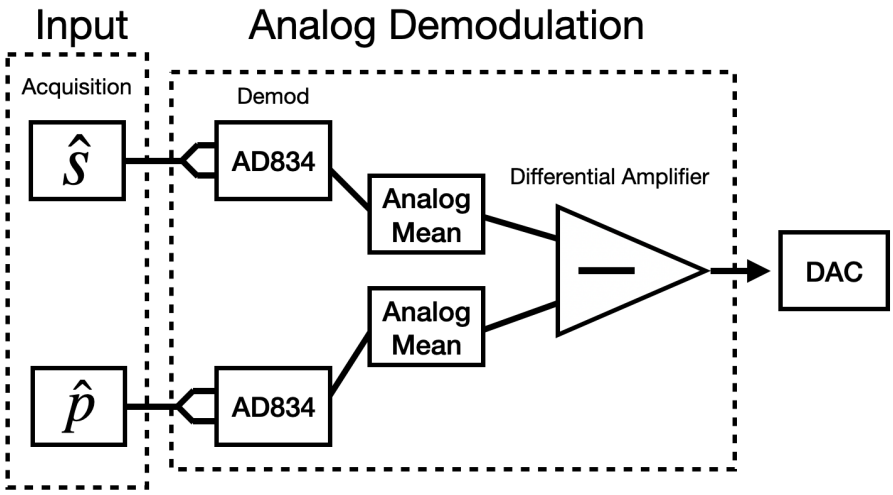

Figure 6.2: Analog demodulation concept circuit for power based DBHD demodulation and detection leveraging the AD834 four-quadrant multiplier circuit shown in the previous figure.

would significantly reduce the requirements on data acquisition, simplifying the system's practical implementation. A general block diagram can be found in Fig. 6.2. At 85 MHz, certain RF considerations would need to be addressed during circuit design. However, the primary challenge would lie in managing the electronic noise of the system.

6.2.3 Scale Factor Stabilization

The primary challenge of our measurement system is that the bias point of the polarization is only stable for approximately 500 μs. In Chapter 3, we implemented an active noise-canceling system that used a feedback loop to reduce laser intensity noise. Ideally, an active polarization noise stabilization device could be implemented to increase measurement stability time, enabling longer integration periods.

I initially tested a rudimentary stabilization device using a liquid crystal variable waveplate. However, this device was optimized for binary operation and did not perform well for active polarization noise cancellation. A piezoelectric-driven rotational nanopositioning stage could provide finer movement resolution and enable active noise cancellation. Nevertheless, a device with smoother motion dynamics would be preferred.

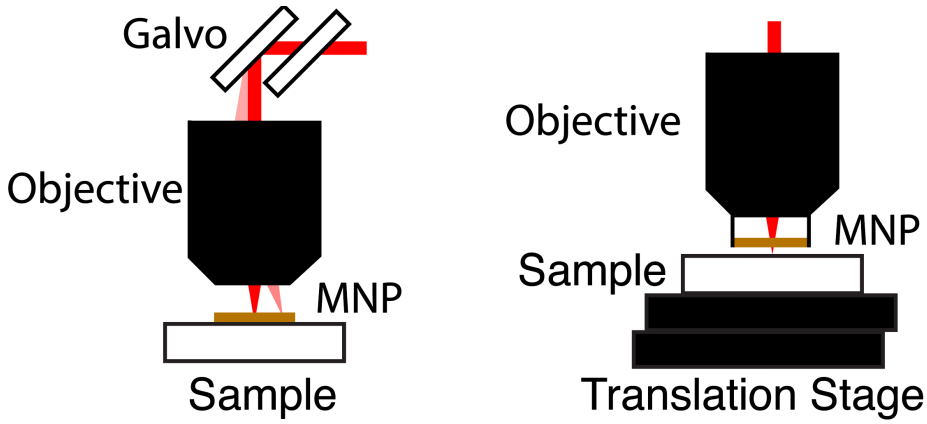

Figure 6.3: Potential imaging configurations. Left) Laser scanner configuration where galvonometer is used to sweep laser spot on sample. Right) Translation stage measurement with fixed MNP thin film

The polarization stability issue is fundamentally an engineering challenge related to packaging and system design and remains an active area of development for the DBHD magnetometer.

6.2.4 Imaging

All of the work that I have done during my PhD has revolved around one form of imaging or another. However, technical challenges associated with achieving a single-pixel measurement prevented me from fully exploring the implementation of a complete imaging system.

Specifically, regarding the magnetometer, we considered two different imaging configurations. The first configuration, designed for fast imaging, involved constructing a diffraction-limited laser scanning head capable of rapidly sweeping a spot size over a sample to produce images. Concerns arose regarding non-uniformity in the thin-film, which could affect polarization stability. To mitigate this issue, we implemented a scheme where the sample, rather than the laser spot, would be moved, allowing the laser to remain fixed in one place on the MNP thin film. The two configurations have are shown in Fig. 6.3

Achieving magnetic imaging requires high long-term measurement stability, which the current system is not capable of providing. However, I have laid the groundwork for enhancing the system to enable the development of a truly revolutionary imaging magnetometer.

6.3 Backmatter

6.3.1 Thesis contributions

The work discussed in this thesis is documented in the following papers:

(1) Jan Bartos, Taleb Ba Tis, Mingming Nie, Shu-Wei Huang, and Wounjhang Park. "High-Verdet Constant and Low-Optical Loss Tb^{3+} Doped Magnetite Nanoparticles." *Nano Letters* 24, no. 30 (2024): 9163-9168.

(2) Jan Bartos, Taleb Ba Tis, Wounjhang Park, Shu-Wei Huang. "Favorable Size-Sensitivity Scaling of Faraday Rotation Magnetometers", In preparation

In addition, I worked on the following papers during my time at the University of Colorado, Boulder, but these papers are not discussed in this thesis:

(1) Bowen Li, Jan Bartos, Yijun Xie, and Shu-Wei Huang. "Time-magnified photon counting with 550-fs resolution." *Optica* 8, no. 8 (2021): 1109-1112.

(2) Mingming Nie, Jonathan Musgrave, Kunpeng Jia, Jan Bartos, Shining Zhu, Zhenda Xie, and Shu-Wei Huang. "Turnkey photonic flywheel in a microresonator-filtered laser." *Nature Communications* 15, no. 1 (2024): 55.

(3) Samuel Galinsky, Euduardo Miscles, Jan Bartos, Jon Musgrave, Shu-Wei Huang, Victor Bright, and Juliet Gopinath. "Nonmechanical spectral domain optical coherence tomography using an electrowetting beam-scanner", In preparation

(4) Gazelle Hajimazdarani, Jan Bartos, and Shu-Wei Huang. "Stimulated Brillouin Gain in Long Lithium Niobate on Chip Waveguides." In preparation.

The following provisional patents cover some of my work:

(1) Non-Mechanical Tomography System - No. 63/718,135

6.3.2 AI Use Disclosure

This thesis was written in the early days of widespread large language model use and best practices have not been fully established. I disclose that I used the OpenAI ChatGPT 4o model as a tool for editing this thesis. AI was not used to generate original content.

Bibliography

[1] Analog Devices. Low noise signal conditioning for sensor-based measurements. Technical Report AN-212, Analog Devices, Inc., 2009. Accessed: 2024-12-26.

[2] Donald B. Plewes and Walter Kucharczyk. Physics of MRI: A primer. Journal of Magnetic Resonance Imaging, 35(5):1038–1054, 2012.

[3] Matthew J Turner, Nicholas Langellier, Rachel Bainbridge, Dan Walters, Srujan Meesala, Thomas M Babinec, Pauli Kehayias, Amir Yacoby, Evelyn Hu, Marko Lončar, et al. Magnetic field fingerprinting of integrated-circuit activity with a quantum diamond microscope. Physical Review Applied, 14(1):014097, 2020.

[4] David R Glenn, Kyungheon Lee, Hongkun Park, Ralph Weissleder, Amir Yacoby, Mikhail D Lukin, Hakho Lee, Ronald L Walsworth, and Colin B Connolly. Single-cell magnetic imaging using a quantum diamond microscope. Nature methods, 12(8):736–738, 2015.

[5] Michael Faraday. I. experimental researches in electricity.—nineteenth series. Philosophical Transactions of the Royal Society of London, 1846.

[6] Zachary Nelson, Léo Delage-Laurin, and Timothy M Swager. ABCs of faraday rotation in organic materials. Journal of the American Chemical Society, 144(27):11912–11926, 2022.

[7] Kyle J Carothers, Robert A Norwood, and Jeffrey Pyun. High verdet constant materials for magneto-optical faraday rotation: A review. Chemistry of Materials, 34(6):2531–2544, 2022.

[8] David C Jiles and David L Atherton. Theory of ferromagnetic hysteresis. Journal of magnetism and magnetic materials, 61(1-2):48–60, 1986.

[9] Andrew L Balk, Carlos Hangarter, Samuel M Stavis, and John Unguris. Magnetometry of single ferromagnetic nanoparticles using magneto-optical indicator films with spatial amplification. Applied Physics Letters, 106(11), 2015.

[10] Mehmet C Onbasli, Lukáš Beran, Martin Zahradník, Miroslav Kučera, Roman Antoš, Jan Mistrík, Gerald F Dionne, Martin Veis, and Caroline A Ross. Optical and magneto-optical behavior of cerium yttrium iron garnet thin films at wavelengths of 200–1770 nm. Scientific reports, 6(1):23640, 2016.

[11] Sara A Majetich, Tianlong Wen, and O Thompson Mefford. Magnetic nanoparticles. MRS Bulletin, 38(11):899–903, 2013.

[12] Zhe Chen, Yin Hang, Xiangyong Wang, and Jiaqi Hong. Fabrication and characterization of tgg crystals containing paramagnetic rare-earth ions. Solid State Communications, 241:38–42, 2016.

[13] David Vojna, Ondřej Slezák, Antonio Lucianetti, and Tomáš Mocek. Verdet constant of magneto-active materials developed for high-power faraday devices. Applied Sciences, 9(15):3160, 2019.

[14] Kamil Barczak, Ryszard Cimek, and Ryszard Buczynski. Measurements of verdet constant in heavy metal oxide glasses for magneto-optic fiber current sensors. Optical Materials, 123:111942, 2022.

[15] Kevin T Stevens, Wolfgang Schlichting, Gregory Foundos, Alexis Payne, and Evan Rogers. Promising materials for high power laser isolators: Growth of large single-crystals for faraday rotator and isolator applications. Laser Technik Journal, 13(3):18–21, 2016.

[16] Jiawei Dai, Yubai Pan, Xiaoying Li, Tengfei Xie, Zhaoxiang Yang, and Jiang Li. Fabrication and properties of $(Tb_{1-x}Ce_x)_3Al_5O_{12}$ magneto-optical ceramics with different doping concentrations. Scripta Materialia, 155:46–49, 2018.

[17] Philippe Veber, Matias Velázquez, Grégory Gadret, Daniel Rytz, Mark Peltz, and Rodolphe Decourt. Flux growth at 1230 c of cubic tb 2 o 3 single crystals and characterization of their optical and magnetic properties. CrystEngComm, 17(3):492–497, 2015.

[18] Jan Bartos, Taleb Ba Tis, Mingming Nie, Shu-Wei Huang, and Wounjhang Park. High-verdet constant and low-optical loss tb3+ doped magnetite nanoparticles. Nano letters, 24(30):9163–9168, 2024.

[19] A Lopez-Santiago, P Gangopadhyay, J Thomas, RA Norwood, A Persoons, and N Peyghambarian. Faraday rotation in magnetite-polymethylmethacrylate core-shell nanocomposites with high optical quality. Applied Physics Letters, 95(14), 2009.

[20] Alejandra Lopez-Santiago, Hannah R Grant, Palash Gangopadhyay, Ramakrishna Voorakaranam, Robert A Norwood, and N Peyghambarian. Cobalt ferrite nanoparticles polymer composites based all-optical magnetometer. Optical Materials Express, 2(7):978–986, 2012.

[21] Alexander Miles, Yue Gai, Palash Gangopadhyay, Xinyu Wang, Robert A Norwood, and James J Watkins. Improving faraday rotation performance with block copolymer and FePt nanoparticle magneto-optical composite. Optical Materials Express, 7(6):2126–2140, 2017.

[22] Kyle J Carothers, Nicholas P Lyons, Nicholas G Pavlopoulos, Kyung-Seok Kang, Tobias M Kochenderfer, Anthony Phan, Lindsey N Holmen, Shelbi L Jenkins, In-Bo Shim, Robert A Norwood, et al. Polymer-coated magnetic nanoparticles as ultrahigh verdet constant materials: correlation of nanoparticle size with magnetic and magneto-optical properties. Chemistry of Materials, 33(13):5010–5020, 2021.

[23] Léo Delage-Laurin and Timothy M Swager. Liquid crystalline magneto-optically active peralkylated azacoronene. JACS Au, 3(7):1965–1974, 2023.

[24] HP Fu, RY Hong, YJ Wu, GQ Di, B Xu, Yaolin Zheng, and DG Wei. Preparation and faraday rotation of Bi-YIG/PMMA nanocomposite. Journal of magnetism and magnetic materials, 320(21):2584–2590, 2008.

[25] Chi Tang, Mohammed Aldosary, Zilong Jiang, Houchen Chang, Benjamin Madon, Kyle Chan, Mingzhong Wu, Javier E Garay, and Jing Shi. Exquisite growth control and magnetic properties of yttrium iron garnet thin films. Applied Physics Letters, 108(10), 2016.

[26] T. Dyer, P. F. Griffin, and E. Riis. Single-board low-noise fluxgate magnetometer. Journal of Applied Physics, 135(3):034501, 01 2024.

[27] Michal Dressler, Michal Janosek, and Mattia Butta. Reduction of magnetic noise limits of orthogonal fluxgate sensor. AIP Advances, 11(1):015347, 01 2021.

[28] Asaf Grosz, Michael J Haji-Sheikh, and Subhas C Mukhopadhyay. High sensitivity magnetometers, volume 19. Springer, 2017.

[29] Jan Dauber, Abhay A. Sagade, Martin Oellers, Kenji Watanabe, Takashi Taniguchi, Daniel Neumaier, and Christoph Stampfer. Ultra-sensitive Hall sensors based on graphene encapsulated in hexagonal boron nitride. Applied Physics Letters, 106(19):193501, 05 2015.

[30] O. Kazakova, V. Panchal, J. Gallop, P. See, D. C. Cox, M. Spasova, and L. F. Cohen. Ultrasmall particle detection using a submicron Hall sensor. Journal of Applied Physics, 107(9):09E708, 04 2010.

[31] Jan-Hendrik Storm, Peter Hömmen, Dietmar Drung, and Rainer Körber. An ultra-sensitive and wideband magnetometer based on a superconducting quantum interference device. Applied Physics Letters, 110(7):072603, 02 2017.

[32] John R. Kirtley and John P. Wikswo. Scanning squid microscopy. Annual Review of Materials Research, 29(Volume 29, 1999):117–148, 1999.

[33] Elena Boto, Sofie S Meyer, Vishal Shah, Orang Alem, Svenja Knappe, Peter Kruger, T Mark Fromhold, Mark Lim, Paul M Glover, Peter G Morris, et al. A new generation of magnetoencephalography: Room temperature measurements using optically-pumped magnetometers. NeuroImage, 149:404–414, 2017.

[34] Orang Alem, K Jeramy Hughes, Isabelle Buard, Teresa P Cheung, Tyler Maydew, Andreas Griesshammer, Kendall Holloway, Aaron Park, Vanessa Lechuga, Collin Coolidge, et al. An integrated full-head OPM-MEG system based on 128 zero-field sensors. Frontiers in Neuroscience, 17:1190310, 2023.

[35] Ying Xu, Weiye Zhang, and Chuanshan Tian. Recent advances on applications of NV-magnetometry in condensed matter physics. Photonics Research, 11(3):393–412, 2023.

[36] John F Barry, Jennifer M Schloss, Erik Bauch, Matthew J Turner, Connor A Hart, Linh M Pham, and Ronald L Walsworth. Sensitivity optimization for NV-diamond magnetometry. Reviews of Modern Physics, 92(1):015004, 2020.

[37] Thomas Wolf, Philipp Neumann, Kazuo Nakamura, Hitoshi Sumiya, Takeshi Ohshima, Junichi Isoya, and Jörg Wrachtrup. Subpicotesla diamond magnetometry. Physical Review X, 5(4):041001, 2015.

[38] Dwi Prananto, Daisuke Kikuchi, Kunitaka Hayashi, Yuta Kainuma, and Toshu An. Imaging of stray magnetic field vectors from a magnetic particle with an ensemble of nitrogen-vacancy centers in diamond. Japanese Journal of Applied Physics, 58(SI):SIIB20, 2019.

[39] Merrit N Deeter, AH Rose, and Gordon W Day. Fast, sensitive magnetic-field sensors based on the faraday effect in YIG. Journal of lightwave technology, 8(12):1838–1842, 1990.

[40] Ogsen Galstyan, Hanju Lee, Arsen Babajanyan, Arsen Hakhoumian, Barry Friedman, and Kiejin Lee. Magneto-optical visualization by Bi:YIG thin films prepared at low temperatures. Journal of Applied Physics, 117(16), 2015.

[41] Vinay Sharma and Bijoy Kumar Kuanr. Magnetic and crystallographic properties of rare-earth substituted yttrium-iron garnet. Journal of Alloys and Compounds, 748:591–600, 2018.

[42] Viet Dongquoc, Phuoc Cao Van, Rambabu Kuchi, Trinh Nguyen Thi, Duc Duong Viet, Eui-Tae Kim, Byong-Guk Park, Ji-Wan Kim, and Jong-Ryul Jeong. Extraordinary enhancement of magneto-optical faraday rotation angle in Bi-YIG/Pt/glass prepared by metal organic decomposition method. Surfaces and Interfaces, page 104652, 2024.

[43] MN Deeter, Gordon W Day, TJ Beahn, and M Manheimer. Magneto-optic magnetic field sensor with 1.4 pt/sqrt(hz) minimum detectable field at 1 khz. Electronics Letters, 29(11):993–994, 1993.

[44] Ulf Holm, Hans Sohlstrom, and Torgny Brogardh. YIG-sensor design for fibre optical magnetic field measurements. In 2nd Intl Conf on Optical Fiber Sensors: OFS'84, volume 514, pages 333–336. SPIE, 1984.

[45] Merritt N Deeter, Allen H Rose, and Gordon W Day. Faraday-effect magnetic field sensors based on substituted iron garnets. In Fiber Optic and Laser Sensors VIII, volume 1367, pages 243–248. SPIE, 1991.

[46] N Koshev, P Kapralov, Svetlana Evstigneeva, O Lutsenko, Polina Shilina, M Zharkov, N Pyataev, A Darwish, A Timin, Maxim Ostras, et al. Yttrium-iron garnet film magnetometer for registration of magnetic nano-and submicron particles: In vitro and in vivo studies. IEEE Transactions on Biomedical Engineering, 2023.

[47] Ekaterina Skidchenko, Anna Butorina, Maxim Ostras, Petr Vetoshko, Alexey Kuzmichev, Nikolay Yavich, Mikhail Malovichko, and Nikolay Koshev. Yttrium-iron garnet magnetometer in meg: Advance towards multi-channel arrays. Sensors, 23(9):4256, 2023.

[48] James S Bennett, Brian E Vyhnalek, Hamish Greenall, Elizabeth M Bridge, Fernando Gotardo, Stefan Forstner, Glen I Harris, Félix A Miranda, and Warwick P Bowen. Precision magnetometers for aerospace applications: A review. Sensors, 21(16):5568, 2021.

[49] Maneea Eizadi Sharifabad, Rémy Soucaille, Xuyiling Wang, Michael Rotherham, Tom Loughran, James Everett, David Cabrera, Ying Yang, Robert Hicken, and Neil Telling. Optical microscopy using the faraday effect reveals in situ magnetization dynamics of magnetic nanoparticles in biological samples. ACS nano, 18(7):5297–5310, 2024.

[50] Boris Polyak and Gary Friedman. Magnetic targeting for site-specific drug delivery: applications and clinical potential. Expert opinion on drug delivery, 6(1):53–70, 2009.

[51] Ilja Fescenko, Abdelghani Laraoui, Janis Smits, Nazanin Mosavian, Pauli Kehayias, Jong Seto, Lykourgos Bougas, Andrey Jarmola, and Victor M Acosta. Diamond magnetic microscopy of malarial hemozoin nanocrystals. Physical review applied, 11(3):034029, 2019.

[52] Seongtae Bae, Sang Won Lee, Atsuo Hirukawa, Yasushi Takemura, Youn Haeng Jo, and Sang Geun Lee. AC magnetic-field-induced heating and physical properties of ferrite nanoparticles for a hyperthermia agent in medicine. IEEE Transactions on nanotechnology, 8(1):86–94, 2008.

[53] Barbara A Maher, Imad AM Ahmed, Vassil Karloukovski, Donald A MacLaren, Penelope G Foulds, David Allsop, David MA Mann, Ricardo Torres-Jardón, and Lilian Calderon-Garciduenas. Magnetite pollution nanoparticles in the human brain. Proceedings of the National Academy of Sciences, 113(39):10797–10801, 2016.

[54] P Kehayias, EV Levine, L Basso, J Henshaw, M Saleh Ziabari, M Titze, R Haltli, J Okoro, DR Tibbetts, DM Udoni, et al. Measurement and simulation of the magnetic fields from a 555 timer integrated circuit using a quantum diamond microscope and finite-element analysis. Physical Review Applied, 17(1):014021, 2022.

[55] Maitreyi Ashok, Matthew J Turner, Ronald L Walsworth, Edlyn V Levine, and Anantha P Chandrakasan. Hardware trojan detection using unsupervised deep learning on quantum diamond microscope magnetic field images. ACM Journal on Emerging Technologies in Computing Systems (JETC), 18(4):1–25, 2022.

[56] Pauli Kehayias, Ezra Bussmann, Tzu-Ming Lu, and Andrew M Mounce. A physically unclonable function using NV diamond magnetometry and micromagnet arrays. Journal of Applied Physics, 127(20), 2020.

[57] David A Broadway, Sam C Scholten, Cheng Tan, Nikolai Dontschuk, Scott E Lillie, Brett C Johnson, Guolin Zheng, Zhenhai Wang, Artem R Oganov, Shangjie Tian, et al. Imaging domain reversal in an ultrathin van der waals ferromagnet. Advanced Materials, 32(39):2003314, 2020.

[58] SC Scholten, AJ Healey, IO Robertson, GJ Abrahams, DA Broadway, and J-P Tetienne. Widefield quantum microscopy with nitrogen-vacancy centers in diamond: Strengths, limitations, and prospects. Journal of Applied Physics, 130(15), 2021.

[59] Jundi Li, Wei Quan, Binquan Zhou, Zhuo Wang, Jixi Lu, Zhaohui Hu, Gang Liu, and Jiancheng Fang. Serf atomic magnetometer–recent advances and applications: A review. IEEE Sensors Journal, 18(20):8198–8207, 2018.

[60] Rudolf Schäfer and Jeffrey McCord. Magneto-optical microscopy. Magnetic measurement techniques for materials characterization, pages 171–229, 2021.

[61] T Aichele, A Lorenz, R Hergt, and P Görnert. Garnet layers prepared by liquid phase epitaxy for microwave and magneto-optical applications–a review. Crystal Research and Technology: Journal of Experimental and Industrial Crystallography, 38(7-8):575–587, 2003.

[62] Jihye Yang and Hanju Lee. Simultaneous imaging of static and microwave magnetic field distributions by magneto optical indicator microscopy. IEEE Access, 2024.

[63] Hironaru Murakami and Masayoshi Tonouchi. High-sensitive scanning laser magneto-optical imaging system. Review of Scientific Instruments, 81(1), 2010.

[64] JM Hafez, J Gao, and JG Eden. Detection of weak (0.5–300nt), low frequency (5–100hz) magnetic fields at room temperature by kilohertz modulation of the magneto-optical hysteresis in rare earth–iron garnet films. Applied physics letters, 90(13), 2007.

[65] Pabitra Mandal, Debanjan Chowdhury, SS Banerjee, and T Tamegai. High sensitivity differential magneto-optical imaging with a compact faraday-modulator. Review of Scientific Instruments, 83(12), 2012.

[66] Yoichi Shiota, Shinsaku Funada, Ryusuke Hisatomi, Takahiro Moriyama, and Teruo Ono. Imaging of caustic-like spin wave beams using optical heterodyne detection. Applied Physics Letters, 116(19), 2020.

[67] Brian T Schaefer, Lei Wang, Alexander Jarjour, Kenji Watanabe, Takashi Taniguchi, Paul L McEuen, and Katja C Nowack. Magnetic field detection limits for ultraclean graphene hall sensors. Nature communications, 11(1):4163, 2020.

[68] Kento Sasaki, Ed E Kleinsasser, Zhouyang Zhu, Wen-Di Li, Hideyuki Watanabe, Kai-Mei C Fu, Kohei M Itoh, and Eisuke Abe. Dynamic nuclear polarization enhanced magnetic field sensitivity and decoherence spectroscopy of an ensemble of near-surface nitrogen-vacancy centers in diamond. Applied Physics Letters, 110(19), 2017.

[69] Mayeul Chipaux, Alexandre Tallaire, Jocelyn Achard, Sébastien Pezzagna, Jan Meijer, Vincent Jacques, Jean-François Roch, and Thierry Debuisschert. Magnetic imaging with an ensemble of nitrogen-vacancy centers in diamond. The European Physical Journal D, 69:1–10, 2015.

[70] Rupak Timalsina, Cody Schultz, Suvechhya Lamichhane, Adam Erickson, Sy-Hwang Liou, Rebecca Lai, and Abdelghani Laraoui. Magnetic sensing of iron in biomolecules using diamond nitrogen vacancy centers. In APS March Meeting Abstracts, volume 2022, pages Q39–004, 2022.

[71] John F Barry, Matthew J Turner, Jennifer M Schloss, David R Glenn, Yuyu Song, Mikhail D Lukin, Hongkun Park, and Ronald L Walsworth. Optical magnetic detection of single-neuron action potentials using quantum defects in diamond. Proceedings of the National Academy of Sciences, 113(49):14133–14138, 2016.

[72] James L Webb, Joshua D Clement, Luca Troise, Sepehr Ahmadi, Gustav Juhl Johansen, Alexander Huck, and Ulrik L Andersen. Nanotesla sensitivity magnetic field sensing using a compact diamond nitrogen-vacancy magnetometer. Applied Physics Letters, 114(23), 2019.

[73] Joseph Shaji Rebeirro, Muhib Omar, Till Lenz, Omkar Dhungel, Peter Blümler, Dmitry Budker, and Arne Wickenbrock. Microwave-free wide-field magnetometry using nitrogen-vacancy centers. arXiv preprint arXiv:2310.16575, 2023.

[74] Zeeshawn Kazi, Isaac Shelby, Nicholas Brunelle, Hideyuki Watanabe, Kohei M Itoh, Paul Wiggins, and Kai-Mei Fu. Wide-field magnetic imaging of sub-50 nm ferromagnetic nanoparticles for time-resolved bio-mechanical orientation measurements. In 2019 Conference on Lasers and Electro-Optics (CLEO), pages 1–2. IEEE, 2019.

[75] Zhecheng Wang, Fei Kong, Pengju Zhao, Zhehua Huang, Pei Yu, Ya Wang, Fazhan Shi, and Jiangfeng Du. Picotesla magnetometry of microwave fields with diamond sensors. Science advances, 8(31):eabq8158, 2022.

[76] O Kazakova, R Puttock, C Barton, H Corte-León, M Jaafar, V Neu, and A Asenjo. Frontiers of magnetic force microscopy. Journal of applied Physics, 125(6), 2019.

[77] Alix Tatiana Escalante-Quiceno, Ondřej Novotnỳ, Jan Neuman, César Magén, and José María De Teresa. Long-term performance of magnetic force microscopy tips grown by focused electron beam induced deposition. Sensors, 23(6):2879, 2023.

[78] Orang Alem, Rahul Mhaskar, Ricardo Jiménez-Martínez, Dong Sheng, John LeBlanc, Lutz Trahms, Tilmann Sander, John Kitching, and Svenja Knappe. Magnetic field imaging with microfabricated optically-pumped magnetometers. Optics express, 25(7):7849–7858, 2017.

[79] Young Jin Kim and Igor Savukov. Ultra-sensitive magnetic microscopy with an optically pumped magnetometer. Scientific reports, 6(1):24773, 2016.

[80] Feng Wang, Juan Wang, and Xiaogang Liu. Direct evidence of a surface quenching effect on size-dependent luminescence of upconversion nanoparticles. Angew. Chem. Int. Ed, 49(41):7456–7460, 2010.

[81] Faheem Ahmad, Mounir M Salem-Bekhit, Faryad Khan, Sultan Alshehri, Amir Khan, Mohammed M Ghoneim, Hui-Fen Wu, Ehab I Taha, and Ibrahim Elbagory. Unique properties of surface-functionalized nanoparticles for bio-application: functionalization mechanisms and importance in application. Nanomaterials, 12(8):1333, 2022.

[82] Chen Fang, Narayan Bhattarai, Conroy Sun, and Miqin Zhang. Functionalized nanoparticles with long-term stability in biological media. Small (Weinheim an der Bergstrasse, Germany), 5(14):1637, 2009.

[83] Conrad Corbella Bagot, Taleb Ba Tis, Bo Xu, Cobi Sabo, Eric Rappeport, and Wounjhang Park. Optical force sensor based on plasmon modulated upconversion luminescence. Advanced Optical Materials, page 2400393, 2024.

[84] Conrad Corbella Bagot, Eric Rappeport, Ananda Das, Taleb Ba Tis, and Wounjhang Park. True FRET-based sensing of pH via separation of FRET and photon reabsorption. Advanced Optical Materials, 10(15):2200242, 2022.

[85] Rong Xu, Huiqun Cao, Danying Lin, Bin Yu, and Junle Qu. Lanthanide-doped upconversion nanoparticles for biological super-resolution fluorescence imaging. Cell Reports Physical Science, 3(6), 2022.

[86] Michael J Sanderson, Ian Smith, Ian Parker, and Martin D Bootman. Fluorescence microscopy. Cold Spring Harbor Protocols, 2014(10):pdb–top071795, 2014.

[87] Fritjof Helmchen and Winfried Denk. Deep tissue two-photon microscopy. Nature methods, 2(12):932–940, 2005.

[88] Shihui Wen, Jiajia Zhou, Kezhi Zheng, Artur Bednarkiewicz, Xiaogang Liu, and Dayong Jin. Advances in highly doped upconversion nanoparticles. Nature communications, 9(1):2415, 2018.

[89] Feng Wang, Debapriya Banerjee, Yongsheng Liu, Xueyuan Chen, and Xiaogang Liu. Upconversion nanoparticles in biological labeling, imaging, and therapy. Analyst, 135(8):1839–1854, 2010.

[90] Xian Chen, Denfeng Peng, Qiang Ju, and Feng Wang. Photon upconversion in core–shell nanoparticles. Chemical Society Reviews, 44(6):1318–1330, 2015.

[91] Jan Bartos, Taleb Ba Tis, Mingming Nie, Shu-Wei Huang, and Wounjhang Park. High-verdet constant and low-optical loss tb3+ doped magnetite nanoparticles. Nano letters, 24(30):9163–9168, 2024.

[92] SD Jacobs, KJ Teegarden, and RK Ahrenkiel. Faraday rotation optical isolator for 10.6-μm radiation. Applied Optics, 13(10):2313–2316, 1974.

[93] Keyu Xia, Nan Zhao, Jason Twamley, and EQuS Collaboration. Detection of a weak magnetic field via cavity-enhanced faraday rotation. Physical Review A, 92(4):043409, 2015.

[94] Kyle J Carothers, Robert A Norwood, and Jeffrey Pyun. High verdet constant materials for magneto-optical faraday rotation: A review. Chemistry of Materials, 34(6):2531–2544, 2022.

[95] David Vojna, Ondřej Slezák, Antonio Lucianetti, and Tomáš Mocek. Verdet constant of magneto-active materials developed for high-power faraday devices. Applied Sciences, 9(15):3160, 2019.

[96] Herbert Piller. Faraday rotation. In Semiconductors and Semimetals, volume 8, pages 103–179. Elsevier, 1972.

[97] Zachary Nelson, Léo Delage-Laurin, and Timothy M Swager. Abcs of faraday rotation in organic materials. Journal of the American Chemical Society, 144(27):11912–11926, 2022.

[98] Ondrej Slezak, Ryo Yasuhara, Antonio Lucianetti, and Tomas Mocek. Wavelength dependence of magneto-optic properties of terbium gallium garnet ceramics. Optics Express, 23(10):13641–13647, 2015.

[99] Guojun Gao, Anja Winterstein-Beckmann, Oleksii Surzhenko, Carsten Dubs, Jan Dellith, Markus A Schmidt, and Lothar Wondraczek. Faraday rotation and photoluminescence in heavily tb3+-doped geo2-b2o3-al2o3-ga2o3 glasses for fiber-integrated magneto-optics. Scientific reports, 5(1):8942, 2015.

[100] NG Pavlopoulos, KS Kang, LN Holmen, NP Lyons, F Akhoundi, KJ Carothers, SL Jenkins, T Lee, TM Kochenderfer, A Phan, et al. Polymer and magnetic nanoparticle composites with tunable magneto-optical activity: role of nanoparticle dispersion for high verdet constant materials. Journal of Materials Chemistry C, 8(16):5417–5425, 2020.

[101] A Lopez-Santiago, P Gangopadhyay, J Thomas, RA Norwood, A Persoons, and N Peyghambarian. Faraday rotation in magnetite-polymethylmethacrylate core-shell nanocomposites with high optical quality. Applied Physics Letters, 95(14), 2009.

[102] RK Ahrenkiel, TJ Coburn, D Pearlman, E Carnall Jr, TW Martin, and SL Lyu. A new class of room-temperature magneto-optic insulators: The cobalt ferrites. In AIP Conference Proceedings, volume 24, pages 186–187. American Institute of Physics, 1975.

[103] Alejandra Lopez-Santiago, Hannah R Grant, Palash Gangopadhyay, Ramakrishna Voorakaranam, Robert A Norwood, and N Peyghambarian. Cobalt ferrite nanoparticles polymer composites based all-optical magnetometer. Optical Materials Express, 2(7):978–986, 2012.

[104] Kyle J Carothers, Nicholas P Lyons, Nicholas G Pavlopoulos, Kyung-Seok Kang, Tobias M Kochenderfer, Anthony Phan, Lindsey N Holmen, Shelbi L Jenkins, In-Bo Shim, Robert A Norwood, et al. Polymer-coated magnetic nanoparticles as ultrahigh verdet constant materials: correlation of nanoparticle size with magnetic and magneto-optical properties. Chemistry of Materials, 33(13):5010–5020, 2021.

[105] Yu A Barnakov, BL Scott, V Golub, L Kelly, V Reddy, and KL Stokes. Spectral dependence of faraday rotation in magnetite-polymer nanocomposites. Journal of Physics and Chemistry of Solids, 65(5):1005–1010, 2004.

[106] Alexander Miles, Yue Gai, Palash Gangopadhyay, Xinyu Wang, Robert A Norwood, and James J Watkins. Improving faraday rotation performance with block copolymer and fept nanoparticle magneto-optical composite. Optical Materials Express, 7(6):2126–2140, 2017.

[107] Ying Xu, Weiye Zhang, and Chuanshan Tian. Recent advances on applications of NV-magnetometry in condensed matter physics. Photonics Research, 11(3):393–412, 2023.

[108] Mehmet C Onbasli, Lukáš Beran, Martin Zahradník, Miroslav Kučera, Roman Antoš, Jan Mistrík, Gerald F Dionne, Martin Veis, and Caroline A Ross. Optical and magneto-optical behavior of cerium yttrium iron garnet thin films at wavelengths of 200–1770 nm. Scientific reports, 6(1):23640, 2016.

[109] Sašo Gyergyek, David Pahovnik, Ema Žagar, Alenka Mertelj, Miloš Beković, Marko Jagodič, Heinrich Hofmann, Darko Makovec, et al. Nanocomposites comprised of homogeneously dispersed magnetic iron-oxide nanoparticles and poly (methyl methacrylate). Beilstein journal of nanotechnology, 9(1):1613–1622, 2018.

[110] Yunxia Jin, David Kishpaugh, Chao Liu, Tibor Jacob Hajagos, Qi Chen, Lu Li, Yi Chen, and Qibing Pei. Partial ligand exchange as a critical approach to the synthesis of transparent ytterbium fluoride–polymer nanocomposite monoliths for gamma ray scintillation. Journal of Materials Chemistry C, 4(16):3654–3660, 2016.

[111] Uygun V Valiev, John B Gruber, Gary W Burdick, Anvar K Mukhammadiev, Dejun Fu, and Vasiliy O Pelenovich. Some interesting features of the tb3+ magnetooptics in the paramagnetic garnets. Optical Materials, 36(7):1101–1111, 2014.

[112] Katherine P Rice, Stephen E Russek, Roy H Geiss, Justin M Shaw, Robert J Usselman, Eric R Evarts, Thomas J Silva, Hans T Nembach, Elke Arenholz, and Yves U Idzerda. Temperature-dependent structure of tb-doped magnetite nanoparticles. Applied Physics Letters, 106(6), 2015.

[113] Channa R De Silva, Steve Smith, Inbo Shim, Jeffrey Pyun, Timothy Gutu, Jun Jiao, and Zhiping Zheng. Lanthanide (iii)-doped magnetite nanoparticles. Journal of the American Chemical Society, 131(18):6336–6337, 2009.

[114] OE Polozhentsev, SP Kubrin, VV Butova, VK Kochkina, AV Soldatov, and VV Stashenko. Structure and magnetic properties of pure and samarium doped magnetite nanoparticles. Journal of Structural Chemistry, 57:1459–1468, 2016.

[115] Richa Jain, Vandna Luthra, and Shubha Gokhale. Dysprosium doping induced correlated electrical and optical behaviour of magnetite nanoparticles. In AIP Conference Proceedings, volume 2136. AIP Publishing, 2019.

[116] Richa Jain, Vandna Luthra, and Shubha Gokhale. Probing influence of rare earth ions (er3+, dy3+ and gd3+) on structural, magnetic and optical properties of magnetite nanoparticles. Journal of Magnetism and Magnetic Materials, 456:179–185, 2018.

[117] VN Nikoforov and BL Oksengendler. Magnetometric study of gadolinium solubility in magnetite nanocrystals. Inorganic Materials, 50:1222–1225, 2014.

[118] Maarten Bloemen, Stefaan Vandendriessche, Vincent Goovaerts, Ward Brullot, Maarten Vanbel, Sophie Carron, Nick Geukens, Tatjana Parac-Vogt, and Thierry Verbiest. Synthesis and characterization of holmium-doped iron oxide nanoparticles. Materials, 7(2):1155–1164, 2014.

[119] Fuxiang Cheng, Chunsheng Liao, Junfeng Kuang, Zhigang Xu, Chunhua Yan, Liangyao Chen, Haibin Zhao, and Zhu Liu. Nanostructure magneto-optical thin films of rare earth (RE = Gd, Tb, Dy) doped cobalt spinel by sol–gel synthesis. Journal of applied physics, 85(5):2782–2786, 1999.

[120] Taleb A Ba Tis. Nanostructured Materials for Optical Sensing. PhD thesis, University of Colorado at Boulder, 2024.

[121] Shouheng Sun and Hao Zeng. Size-controlled synthesis of magnetite nanoparticles. Journal of the American Chemical Society, 124(28):8204–8205, 2002.

[122] Tomoharu Kataoka, Yasunori Tsukahara, Yasuchika Hasegawa, and Yuji Wada. Size-controlled synthesis of quantum-sized EuS nanoparticles and tuning of their faraday rotation peak. Chemical communications, pages 6038–6040, 2005.

[123] François Royer, Damien Jamon, Jean Jacques Rousseau, Valérie Cabuil, Daniel Zins, Hélène Roux, and C Bovier. Experimental investigation on γ- Fe2O3 nanoparticles faraday rotation: particles size dependence. The European Physical Journal-Applied Physics, 22(2):83–87, 2003.

[124] Mladen Lakic, Ljubica Andjelkovic, Marija Sulijagic, Predrag Vulic, Marko Peric, Predrag Iskrenovic, Ivan Krstic, Milorad M Kuraica, and Aleksandar S Nikolic. Optical evidence of magnetic field-induced ferrofluid aggregation: Comparison of cobalt ferrite, magnetite, and magnesium ferrite. Optical Materials, 91:279–285, 2019.

[125] JC Boyer, NJJ Johnson, and FCJM Van Veggel. Upconverting lanthanide-doped NaYF4-PMMA polymer composites prepared by in situ polymerization. Chemistry of Materials, 21(10):2010–2012, 2009.

[126] Jing Tang, Matt Myers, Ken A Bosnick, and Louis E Brus. Magnetite Fe3O4 nanocrystals: spectroscopic observation of aqueous oxidation kinetics. The Journal of Physical Chemistry B, 107(30):7501–7506, 2003.

[127] WFJ Fontijn, PJ Van Der Zaag, LF Feiner, Ruud Metselaar, and MAC Devillers. A consistent interpretation of the magneto-optical spectra of spinel type ferrites. Journal of Applied Physics, 85(8):5100–5105, 1999.

[128] Maxim Demesh, Konstantin Gorbachenya, Viktor Kisel, Elena Volkova, Viktor Maltsev, Elizaveta Koporulina, Elena Dunina, Alexey Kornienko, Ludmila Fomicheva, and Nikolay Kuleshov. Transitions intensities and cross-sections of Tb 3+ ions in YAl 3 (BO 3) 4 crystal. OSA Continuum, 4(3):822–830, 2021.

[129] Peter Dorenbos. The 5d level positions of the trivalent lanthanides in inorganic compounds. Journal of Luminescence, 91(3-4):155–176, 2000.

[130] Richa Jain, Vandna Luthra, and Shubha Gokhale. Dysprosium doping induced shape and magnetic anisotropy of Fe3-xDyxO4 (x=0.01–0.1) nanoparticles. Journal of Magnetism and Magnetic Materials, 414:111–115, 2016.

[131] IM Obaidat, V Mohite, B Issa, N Tit, and Y Haik. Predicting a major role of surface spins in the magnetic properties of ferrite nanoparticles. Crystal Research and Technology: Journal of Experimental and Industrial Crystallography, 44(5):489–494, 2009.

[132] David R Glenn, Kyungheon Lee, Hongkun Park, Ralph Weissleder, Amir Yacoby, Mikhail D Lukin, Hakho Lee, Ronald L Walsworth, and Colin B Connolly. Single-cell magnetic imaging using a quantum diamond microscope. Nature methods, 12(8):736–738, 2015.

[133] Ying Xu, Weiye Zhang, and Chuanshan Tian. Recent advances on applications of NV-magnetometry in condensed matter physics. Photonics Research, 11(3):393–412, 2023.

[134] Pauli Kehayias, Ezra Bussmann, Tzu-Ming Lu, and Andrew M. Mounce. A physically unclonable function using NV diamond magnetometry and micromagnet arrays. Journal of Applied Physics, 127(20), 5 2020.

[135] James S Bennett, Brian E Vyhnalek, Hamish Greenall, Elizabeth M Bridge, Fernando Gotardo, Stefan Forstner, Glen I Harris, Félix A Miranda, and Warwick P Bowen. Precision magnetometers for aerospace applications: A review. Sensors, 21(16):5568, 2021.

[136] SC Scholten, AJ Healey, IO Robertson, GJ Abrahams, DA Broadway, and J-P Tetienne. Widefield quantum microscopy with nitrogen-vacancy centers in diamond: Strengths, limitations, and prospects. Journal of Applied Physics, 130(15), 2021.

[137] Matthew J Turner, Nicholas Langellier, Rachel Bainbridge, Dan Walters, Srujan Meesala, Thomas M Babinec, Pauli Kehayias, Amir Yacoby, Evelyn Hu, Marko Lonvcar, et al. Magnetic field fingerprinting of integrated-circuit activity with a quantum diamond microscope. Physical Review Applied, 14(1):014097, 2020.

[138] Ilja Fescenko, Abdelghani Laraoui, Janis Smits, Nazanin Mosavian, Pauli Kehayias, Jong Seto, Lykourgos Bougas, Andrey Jarmola, and Victor M Acosta. Diamond magnetic microscopy of malarial hemozoin nanocrystals. Physical review applied, 11(3):034029, 2019.

[139] AJ Healey, Alastair Stacey, BC Johnson, DA Broadway, Tokuyuki Teraji, DA Simpson, J-P Tetienne, and LCL Hollenberg. Comparison of different methods of nitrogen-vacancy layer formation in diamond for wide-field quantum microscopy. Physical Review Materials, 4(10):104605, 2020.

[140] Dwi Prananto, Daisuke Kikuchi, Kunitaka Hayashi, Yuta Kainuma, and Toshu An. Imaging of stray magnetic field vectors from a magnetic particle with an ensemble of nitrogen-vacancy centers in diamond. Japanese Journal of Applied Physics, 58(SI):SIIB20, 2019.

[141] Ali Tayefeh Younesi, Muhib Omar, Arne Wickenbrock, Dmitry Budker, and Ronald Ulbricht. Towards high-sensitivity magnetometry with nitrogen vacancy centers in diamond using the singlet infrared absorption. arXiv preprint arXiv:2410.20876, 2024.

[142] John F Barry, Matthew J Turner, Jennifer M Schloss, David R Glenn, Yuyu Song, Mikhail D Lukin, Hongkun Park, and Ronald L Walsworth. Optical magnetic detection of single-neuron action potentials using quantum defects in diamond. Proceedings of the National Academy of Sciences, 113(49):14133–14138, 2016.

[143] Y Masuyama, K Mizuno, H Ozawa, H Ishiwata, Y Hatano, T Ohshima, T Iwasaki, and M Hatano. Extending coherence time of macro-scale diamond magnetometer by dynamical decoupling with coplanar waveguide resonator. Review of Scientific Instruments, 89(12), 2018.

[144] Ruben Piepgras, Sebastian Michlmayr, Johannes Egger, and Bernhard G Zagar. Measurement of magnetic microstructures with a faraday rotation magnetometer. In 2020 IEEE International Instrumentation and Measurement Technology Conference (I2MTC), pages 1–5. IEEE, 2020.

[145] Yin Wang, Michal Nikodem, and Gerard Wysocki. Cryogen-free heterodyne-enhanced mid-infrared faraday rotation spectrometer. Optics express, 21(1):740–755, 2013.

[146] Ekaterina Skidchenko, Anna Butorina, Maxim Ostras, Petr Vetoshko, Alexey Kuzmichev, Nikolay Yavich, Mikhail Malovichko, and Nikolay Koshev. Yttrium-iron garnet magnetometer in meg: Advance towards multi-channel arrays. Sensors, 23(9):4256, 2023.

[147] Jan Bartos, Taleb Ba Tis, Mingming Nie, Shu-Wei Huang, and Wounjhang Park. High-verdet constant and low-optical loss tb3+ doped magnetite nanoparticles. Nano letters, 24(30):9163–9168, 2024.

[148] Dechao He, Boya Xie, and Sheng Feng. Null polarimetry near shot noise limit at 1 hz. Review of Scientific Instruments, 87(4), 2016.

[149] Steeve Cronenberger and Denis Scalbert. Quantum limited heterodyne detection of spin noise. Review of Scientific Instruments, 87(9), 2016.

[150] Yoichi Shiota, Shinsaku Funada, Ryusuke Hisatomi, Takahiro Moriyama, and Teruo Ono. Imaging of caustic-like spin wave beams using optical heterodyne detection. Applied Physics Letters, 116(19), 2020.

[151] Masahiro Yamanari, Shuichi Makita, and Yoshiaki Yasuno. Polarization-sensitive swept-source optical coherence tomography with continuous source polarization modulation. Optics express, 16(8):5892–5906, 2008.

[152] Robert L Rebodos and Peter J Vikesland. Effects of oxidation on the magnetization of nanoparticulate magnetite. Langmuir, 26(22):16745–16753, 2010.

[153] Vladimir Cherepanov, Igor Kolokolov, and Victor L'vov. The saga of YIG: Spectra, thermodynamics, interaction and relaxation of magnons in a complex magnet. Physics reports, 229(3):81–144, 1993.

[154] Steeve Cronenberger and Denis Scalbert. Quantum limited heterodyne detection of spin noise. Review of Scientific Instruments, 87(9), 2016.

[155] Zurich Instruments. Principles of lock-in detection. Technical report, Zurich Instruments, 2016.

[156] Feifei Wang, Fuqiang Ren, Zhuoran Ma, Liangqiong Qu, Ronan Gourgues, Chun Xu, Ani Baghdasaryan, Jiachen Li, Iman Esmaeil Zadeh, Johannes WN Los, et al. In vivo non-invasive confocal fluorescence imaging beyond 1,700 nm using superconducting nanowire single-photon detectors. Nature Nanotechnology, 17(6):653–660, 2022.

[157] Shuqing He and Zhen Cheng. Advancements of Second Near-Infrared Biological Window Fluorophores: Mechanism, Synthesis, and Application In Vivo, pages 81–123. Springer International Publishing, Cham, 2020.

[158] Norihiko Nishizawa, Hiroyuki Kawagoe, Masahito Yamanaka, Miyoko Matsushima, Kensaku Mori, and Tsutomu Kawabe. Wavelength dependence of ultrahigh-resolution optical coherence tomography using supercontinuum for biomedical imaging. IEEE Journal of Selected Topics in Quantum Electronics, 25(1):1–15, 2018.

[159] Karsten König. Multiphoton microscopy in life sciences. Journal of microscopy, 200(2):83–104, 2000.

[160] Monica Monici. Cell and tissue autofluorescence research and diagnostic applications. Biotechnology annual review, 11:227–256, 2005.

[161] Fritjof Helmchen and Winfried Denk. Deep tissue two-photon microscopy. Nature methods, 2(12):932–940, 2005.

[162] Janah Shaya, Peter R Corridon, Basem Al-Omari, Abdulrahman Aoudi, Abeer Shunnar, Mohamed Infas Haja Mohideen, Ahsanulhaq Qurashi, Benoît Y Michel, and Alain Burger. Design, photophysical properties, and applications of fluorene-based fluorophores in two-photon fluorescence bioimaging: A review. Journal of Photochemistry and Photobiology C: Photochemistry Reviews, 52:100529, 2022.

[163] F Pelayo García de Arquer, Dmitri V Talapin, Victor I Klimov, Yasuhiko Arakawa, Manfred Bayer, and Edward H Sargent. Semiconductor quantum dots: Technological progress and future challenges. Science, 373(6555):eaaz8541, 2021.

[164] Mao Ye and Peter C Searson. Blinking in quantum dots: The origin of the grey state and power law statistics. Physical Review B, 84(12):125317, 2011.

[165] Benoit Mahler, Piernicola Spinicelli, Stephanie Buil, Xavier Quelin, Jean-Pierre Hermier, and Benoit Dubertret. Towards non-blinking colloidal quantum dots. Nature materials, 7(8):659–664, 2008.

[166] Shihui Wen, Jiajia Zhou, Kezhi Zheng, Artur Bednarkiewicz, Xiaogang Liu, and Dayong Jin. Advances in highly doped upconversion nanoparticles. Nature Communications, 9(1):2415, June 2018.

[167] Preethi Selvamuthu, Jaison Darson, Chandrasekar Ponnusamy, Gopalakrishnan Chandrasekar, Sivakumar Muthusamy, Ruckmani Kandasamy, and Subramanian Natesan. Effect of ytterbium and erbium co-doped nayf4@nasmf4 upconversion core-shell nanoparticles on their luminescence and morphological properties. Materials Research Express, 6(10):104004, aug 2019.

[168] Kumbam Lingeshwar Reddy, Ramachandran Balaji, Ashish Kumar, and Venkata Krishnan. Lanthanide doped near infrared active upconversion nanophosphors: fundamental concepts, synthesis strategies, and technological applications. Small, 14(37):1801304, 2018.

[169] Liang Cheng, Kai Yang, Shuai Zhang, Mingwang Shao, Shuittong Lee, and Zhuang Liu. Highly-sensitive multiplexed in vivo imaging using PEGylated upconversion nanoparticles. Nano research, 3:722–732, 2010.

[170] Jie Cao, Binling Zhu, Kefang Zheng, Songguo He, Liang Meng, Jibin Song, and Huanghao Yang. Recent progress in NIR-II contrast agent for biological imaging. Frontiers in bioengineering and biotechnology, 7:487, 2020.

[171] Tian Li, Fu Li, Charles Altuzarra, Anton Classen, and Girish S Agarwal. Squeezed light induced two-photon absorption fluorescence of fluorescein biomarkers. Applied Physics Letters, 116(25):254001, 2020.

[172] Min Gu and CJR Sheppard. Comparison of three-dimensional imaging properties between two-photon and single-photon fluorescence microscopy. Journal of microscopy, 177(2):128–137, 1995.

[173] Kevin J McHugh, Lihong Jing, Adam M Behrens, Surangi Jayawardena, Wen Tang, Mingyuan Gao, Robert Langer, and Ana Jaklenec. Biocompatible semiconductor quantum dots as cancer imaging agents. Advanced Materials, 30(18):1706356, 2018.

[174] Sandy F Himmelstoß and Thomas Hirsch. A critical comparison of lanthanide based upconversion nanoparticles to fluorescent proteins, semiconductor quantum dots, and carbon dots for use in optical sensing and imaging. Methods and applications in fluorescence, 7(2):022002, 2019.

[175] Oleg Varnavski, Brian Pinsky, and Theodore Goodson III. Entangled photon excited fluorescence in organic materials: an ultrafast coincidence detector. The journal of physical chemistry letters, 8(2):388–393, 2017.

[176] Hong-Bing Fei, Bradley M Jost, Sandu Popescu, Bahaa EA Saleh, and Malvin C Teich. Entanglement-induced two-photon transparency. Physical review letters, 78(9):1679, 1997.

[177] Nikunjkumar Prajapati, Ziqi Niu, and Irina Novikova. Quantum-enhanced two-photon spectroscopy using two-mode squeezed light. Optics Letters, 46(8):1800–1803, 2021.

[178] Kristen M. Parzuchowski, Alexander Mikhaylov, Michael D. Mazurek, Ryan N. Wilson, Daniel J. Lum, Thomas Gerrits, Charles H. Camp, Martin J. Stevens, and Ralph Jimenez.

Setting bounds on entangled two-photon absorption cross sections in common fluorophores. Phys. Rev. Appl., 15:044012, Apr 2021.

[179] Bryce P Hickam, Manni He, Nathan Harper, Szilard Szoke, and Scott K Cushing. Single-photon scattering can account for the discrepancies among entangled two-photon measurement techniques. The Journal of Physical Chemistry Letters, 13(22):4934–4940, 2022.

[180] Samuel Corona-Aquino, Omar Calderón-Losada, Mayte Y. Li-Gómez, Hector Cruz-Ramirez, Violeta Álvarez Venicio, María del Pilar Carreón-Castro, Roberto de J. León-Montiel, and Alfred B. URen. Experimental Study of the Validity of Entangled Two-Photon Absorption Measurements in Organic Compounds. The Journal of Physical Chemistry A, 126(14):2185–2195, April 2022.

[181] Stefan Fischer, Heiko Steinkemper, Philipp Löper, Martin Hermle, and Jan Christoph Goldschmidt. Modeling upconversion of erbium doped microcrystals based on experimentally determined Einstein coefficients. Journal of Applied Physics, 111(1), 01 2012. 013109.

[182] Ayelet Teitelboim, Bining Tian, David J. Garfield, Angel Fernandez-Bravo, Adam C. Gotlin, P. James Schuck, Bruce E. Cohen, and Emory M. Chan. Energy transfer networks within upconverting nanoparticles are complex systems with collective, robust, and history-dependent dynamics. The Journal of Physical Chemistry C, 123(4):2678–2689, 2019.

[183] Emory M. Chan, Gang Han, Joshua D. Goldberg, Daniel J. Gargas, Alexis D. Ostrowski, P. James Schuck, Bruce E. Cohen, and Delia J. Milliron. Combinatorial discovery of lanthanide-doped nanocrystals with spectrally pure upconverted emission. Nano Letters, 12(7):3839–3845, 2012. PMID: 22713101.

[184] Changhwan Lee, Emma Z. Xu, Yawei Liu, Ayelet Teitelboim, Kaiyuan Yao, Angel Fernandez-Bravo, Agata M. Kotulska, Sang Hwan Nam, Yung Doug Suh, Artur Bednarkiewicz, Bruce E. Cohen, Emory M. Chan, and P. James Schuck. Giant nonlinear optical responses from photon-avalanching nanoparticles. Nature, 589(7841):230–235, 2021.

[185] Takashi Kushida. Energy transfer and cooperative optical transitions in rare-earth doped inorganic materials. i. transition probability calculation. Journal of the physical society of Japan, 34(5):1318–1326, 1973.

[186] Kristen M Parzuchowski, Alexander Mikhaylov, Michael D Mazurek, Ryan N Wilson, Daniel J Lum, Thomas Gerrits, Charles H Camp Jr, Martin J Stevens, and Ralph Jimenez. Setting bounds on entangled two-photon absorption cross sections in common fluorophores. Physical Review Applied, 15(4):044012, 2021.

[187] John C. Howell, Ryan S. Bennink, Sean J. Bentley, and R. W. Boyd. Realization of the einstein-podolsky-rosen paradox using momentum- and position-entangled photons from spontaneous parametric down conversion. Phys. Rev. Lett., 92:210403, May 2004.

Appendix A

Proof: Noise Transfer through a Power Difference Signal

In the dual-balanced heterodyne detection scheme, we are interested in measuring the electrical power difference between two separate balanced detectors. This alters how the scale factor of the polarization rotation signal is determined. We hypothesized that this would have a significant impact on the minimum detectable polarization rotation. This was not found to be true in experiments. Thus, we need a better understanding of how the noise is affected by taking the power difference.

This proof demonstrates that the minimum detectable polarization rotation angle, corresponding to the magnetic field sensitivity, is the same for both the balanced heterodyne and dual-balanced heterodyne detection methods. I establish this by analyzing the transfer of shot noise through each measurement scheme.

The key to this derivation is the use of the formal definition of the power spectral density $S_i(f)$:

$$S_i(f) = \mathrm{F}\{R_{ii}(\tau)\},$$

defined as the Fourier transform of the autocorrelation, where R_{ii} is the autocorrelation function of random variable $n_i(t)$:

$$R_{ii}(\tau) = \langle n_i(t) n_i(t+\tau) \rangle.$$

I have chosen to model the system in terms of photocurrent. We define the mean photocurrent as

$\bar{I}$ and just considering shot noise as the second term. Each detector sees photocurrent in the form:

$$i_1(t) = \bar{I} + \sqrt{2q\bar{I}} \cdot n_1(t), \quad i_2(t) = \bar{I} + \sqrt{2q\bar{I}} \cdot n_2(t),$$

where:

- $n_1(t)$ and $n_2(t)$ are independent, zero-mean white Gaussian noise processes.
- Autocorrelation: $\langle n_i(t) n_i(t+\tau) \rangle = \delta(\tau)$
- Power Spectral Density: $S_{n_i}(f) = 1$

A.1 Conventional Balanced Detection

Before examining the dual-balanced case, we should first consider how shot noise affects the power in the conventional measurement using a single balanced detector.

We define the differential voltage signal (linear to electrical current):

$$V(t) \propto i_1(t) - i_2(t)$$

We substitute the photocurrent definitions:

$$V(t) = \bar{I} + \sqrt{2q\bar{I}} \cdot n_1(t) - \bar{I} - \sqrt{2q\bar{I}} \cdot n_2(t)$$
$$V(t) = \sqrt{2q\bar{I}} \left(n_1(t) - n_2(t) \right)$$

Solving for the PSD we start with the autocorrelation:

$$R_{\Delta V} = 2q\bar{I} \left\langle (n_1(t) - n_2(t))(n_1(t+\tau) - n_2(t+\tau)) \right\rangle$$

We make the full expansion:

$$R_{\Delta V} = 2q\bar{I} \langle n_1(t) n_1(t+\tau) \rangle - \langle n_1(t) n_2(t+\tau) \rangle - \langle n_2(t) n_1(t+\tau) \rangle + \langle n_2(t) n_2(t+\tau) \rangle$$

We can remove cross terms because $\langle n_i(t)n_j(t+\tau)\rangle = 0$ when the noise is completely uncorrelated. Also, we know from above that the autocorrelation of zero-mean white Gaussian noise only produces values at zero delay $\langle n_i(t)n_i(t+\tau)\rangle = \delta(\tau)$.

$$R_{\Delta V} = 2q\bar{I}(\delta(\tau) + \delta(\tau))$$

$$R_{\Delta V} = 4q\bar{I}\delta(\tau)$$

We can sum the delta functions because they represent uncorrelated noise contributions. We can now take the Fourier Transform to get PSD:

$$S_{\Delta V}(f) = \mathrm{F}\{R_{\Delta V}\} = 4q\bar{I} = 2q\bar{I}_{tot} \quad [A^2/Hz] \tag{A.1}$$

Intuitively, this shows that the shot noise from a balanced detector depends on the total photocurrent, which is itself proportional to the optical power, as expected. The prefactors arise as expecte, and this expression forms the level of abstraction used to consider noise in the literature. The complexity of the proof begins when you need to consider the PSD of the power-difference scheme as seen in dual balanced heterodyne detection (DBHD).

A.2 Dual Balanced Heterodyne Detection

In DBHD we are now interested in the power difference signal (electrical current squared):

$$\Delta P(t) = i_1^2(t) - i_2^2(t)$$

Expanding each squared term:

$$i_1^2(t) = \bar{I}^2 + 2\bar{I}\sqrt{2q\bar{I}}n_1(t) + 2q\bar{I}n_1^2(t),$$

$$i_2^2(t) = \bar{I}^2 + 2\bar{I}\sqrt{2q\bar{I}}n_2(t) + 2q\bar{I}n_2^2(t).$$

This expansion potentially creates the problematic quadratic, non-Gaussian random variable that has a mean: $n_i^2(t)$. Foreshadowing the proof this variable creates a problem because the autocorrelation $\langle n_i^2(t)n_i^2(t+\tau)\rangle$ does not arise simply.

To start the proof we want to separate the linear from the quadratic terms by change of variables:

$$\Delta P(t) = i_1^2(t) - i_2^2(t) = x(t) + y(t).$$

where:

$$x(t) = 2\bar{I}\sqrt{2q\bar{I}}(n_1(t) - n_2(t)), \quad y(t) = 2q\bar{I}(n_1^2(t) - n_2^2(t)).$$

Knowing this, we define the autocorrelation function as:

$$R_{\Delta P}(\tau) = \langle \Delta P(t) \cdot \Delta P(t+\tau) \rangle = \langle (x(t) + y(t))(x(t+\tau) + y(t+\tau)) \rangle$$

Expanding this product

$$R_{\Delta P}(\tau) = \langle x(t)x(t+\tau) \rangle + \langle x(t)y(t+\tau) \rangle + \langle y(t)x(t+\tau) \rangle + \langle y(t)y(t+\tau) \rangle$$

Assuming stationarity and real-valued signals, we use the fact that:

$$\langle x(t)y(t+\tau) \rangle = \langle y(t)x(t+\tau) \rangle$$

Thus, the autocorrelation simplifies to:

$$R_{\Delta P}(\tau) = \langle x(t)x(t+\tau) \rangle + \langle y(t)y(t+\tau) \rangle + 2\langle x(t)y(t+\tau) \rangle$$

Giving us 3 terms to work with:

- Linear Autocorrelation: $R_{xx}(\tau) = \langle x(t)x(t+\tau) \rangle$
- Quadratic Autocorrelation: $R_{yy}(\tau) = \langle y(t)y(t+\tau) \rangle$
- Cross-correlation $R_{xy}(\tau) = 2\langle x(t)y(t+\tau) \rangle$

A.2.1 Linear Autocorrelation

We compute:

$$R_{xx}(\tau) = \langle x(t)x(t+\tau)\rangle = A^2\langle (n_1(t) - n_2(t))(n_1(t+\tau) - n_2(t+\tau))\rangle$$

Where the pre-factors are condensed into $A = 2\bar{I}\sqrt{2q\bar{I}}$. Expanding further:

$$R_{xx}(\tau) = A^2\left[\langle n_1(t)n_1(t+\tau)\rangle + \langle n_2(t)n_2(t+\tau)\rangle - \langle n_1(t)n_2(t+\tau)\rangle - \langle n_2(t)n_1(t+\tau)\rangle\right]$$

Since n_1, n_2 are independent we can simplify:

$$\langle n_1(t)n_2(t+\tau)\rangle = \langle n_2(t)n_1(t+\tau)\rangle = 0$$

$$\langle n_i(t)n_i(t+\tau)\rangle = \delta(\tau) \Rightarrow R_{xx}(\tau) = 2A^2\delta(\tau)$$

Substituting $A^2 = 8q\bar{I}^3$, producing the linear autocorrelation term:

$$R_{xx}(\tau) = 16q\bar{I}^3\delta(\tau) \tag{A.2}$$

A.2.2 Quadratic Autocorrelation

We perform similar operation to calculate the autocorrelation of the quadratic terms. We substitute the prefactor $B = 2q\bar{I}$.

$$y(t) = B(n_1^2(t) - n_2^2(t)) \Rightarrow R_{yy}(\tau) = B^2\langle (n_1^2(t) - n_2^2(t))(n_1^2(t+\tau) - n_2^2(t+\tau))\rangle$$

Expanding:

$$R_{yy}(\tau) = B^2\left[\langle n_1^2(t)n_1^2(t+\tau)\rangle + \langle n_2^2(t)n_2^2(t+\tau)\rangle - 2\langle n_1^2(t)n_2^2(t+\tau)\rangle\right]$$

Dealing with the simple term, using the fact that n_1, n_2 are independent and simplify:

$$\langle n_1^2(t)n_2^2(t+\tau)\rangle = \langle n_1^2(t)\rangle\langle n_2^2(t+\tau)\rangle = 1$$

Thus leaving us with the difficult to handle term:

$$\langle n_i^2(t) n_i^2(t+\tau) \rangle = ?$$

Stochastic signal processing provides us with a theorem to reduce the order of the moment when considering zero-mean Gaussian variables.

A.2.2.1 Isserlis' Theorem

We let X_1, X_2, X_3, X_4 be zero-mean, jointly Gaussian random variables. Then:

$$\langle X_1 X_2 X_3 X_4 \rangle = \langle X_1 X_2 \rangle \langle X_3 X_4 \rangle + \langle X_1 X_3 \rangle \langle X_2 X_4 \rangle + \langle X_1 X_4 \rangle \langle X_2 X_3 \rangle$$

Now apply this to the autocorrelation of squared Gaussian noise:

$$\langle n^2(t) n^2(t+\tau) \rangle = \langle n(t) n(t) n(t+\tau) n(t+\tau) \rangle$$

Identify:

$$X_1 = X_2 = n(t), \quad X_3 = X_4 = n(t+\tau)$$

Using Isserlis' Theorem:

$$\begin{aligned} \langle n^2(t) n^2(t+\tau) \rangle &= \langle n(t) n(t) \rangle \langle n(t+\tau) n(t+\tau) \rangle + 2 \cdot \langle n(t) n(t+\tau) \rangle^2 \\ &= \langle n^2(t) \rangle \langle n^2(t+\tau) \rangle + 2 R_n^2(\tau) \end{aligned}$$

Assuming stationary and unit variance $\langle n^2(t) \rangle = 1$, we get:

$$\langle n^2(t) n^2(t+\tau) \rangle = 1 + 2 R_n^2(\tau)$$

Which completes the autocorrelation expression:

$$R_{yy}(\tau) = B^2 \left[2(2 R_n^2(\tau) + 1) - 2 \right] = 4 B^2 R_n^2(\tau)$$

$$R_{yy}(\tau) = 16 q^2 \bar{I}^2 R_n^2(\tau)$$

Where $R_n^2(\tau) = \delta^2(\tau)$ this provides the following expression:

$$R_{yy}(\tau) = 16q^2\bar{I}^2\delta^2(\tau) \tag{A.3}$$

Which still leaves us with the poorly defined term $\delta^2(\tau)$. This will be dealt with when we Fourier transform the result to get to the noise PSD.

A.2.3 Cross-Term: $R_{xy}(\tau)$

$$R_{xy}(\tau) = \langle x(t)y(t+\tau)\rangle = AB\langle(n_1(t) - n_2(t))(n_1^2(t+\tau) - n_2^2(t+\tau))\rangle$$

Expanding:

$$\begin{aligned} R_{xy}(\tau) = AB\big[&\langle n_1(t)n_1^2(t+\tau)\rangle - \langle n_1(t)n_2^2(t+\tau)\rangle \\ &-\langle n_2(t)n_1^2(t+\tau)\rangle + \langle n_2(t)n_2^2(t+\tau)\rangle\big] \end{aligned}$$

All terms are 3rd-order moments of zero-mean Gaussian variables:

$$\langle n_i(t)n_{i\pm1}^2(t+\tau)\rangle = 0 \quad \text{(Correlation of odd Gaussian moments goes to zero)}$$

So:

$$R_{xy}(\tau) = 0 \tag{A.4}$$

Which is convenient.

A.2.4 Total Autocorrelation

We now combine the individual autocorrelation variables.

$$R_{\Delta P}(\tau) = R_{xx} + R_{yy} + R_{xy}$$

Which gives us the expression[1] :

[1] An aside about units: this is the PSD of a power signal, which is provided in units proportional to $[W^2/Hz] \propto [A^4/Hz]$. This is why the white noise expression has unconventional prefactors

$$R_{\Delta P}(\tau) = 16q\bar{I}^3\delta(\tau) + 16q^2\bar{I}^2\delta^2(\tau) + 0 \tag{A.5}$$

A.3 Noise Power Spectral Density

Now all that is left is to do the Fourier transform of the autocorrelation to arrive at the PSD of the noise. We can split the expression again along linear and quadratic terms. We start with linear terms producing a white noise component as seen in the conventional balanced detection.

$$S_x(f) = \mathrm{F}\{R_{xx}(\tau)\} = 16q\bar{I}^3 \quad [A^4/Hz] \tag{A.6}$$

Next is the quadratic term :

$$S_y(f) = \mathrm{F}\{R_{yy}(\tau)\} = 16q\bar{I}^2 \cdot \mathrm{F}\{\delta^2(\tau)\}$$

To gain intuition on how to handle the squared delta-function I chose to bandwidth limit the white-noise. As is the case in out actually system the acquired bandwidth of the signal is limited by the sampling rate of the system in the frequency domain. We have done this a few time but to review, a non-bandwidth limited system looks like:

$$R_i(\tau) = \delta(\tau) \Rightarrow S_i(f) = 1$$

In the bandwidth limited case this is turned into:

$$S_i'(f) = \mathrm{rect}(\frac{f}{4b_w}) \Rightarrow R_i'(\tau) = \mathrm{sinc}(2b_w\tau)$$

Defining the Nyquist limited acquisition bandwidth as $2b_w$. Bandwidth limiting the signal enables us to take the square of $R_{yy}(\tau)$:

$$R_i^2(\tau) = \text{sinc}^2(2b_w\tau) \Rightarrow \text{F}[R_i^2(\tau)] = \frac{1}{2b_w} \cdot \text{tri}\left(\frac{f}{4b_w}\right)$$

Therefore:

$$S_y(f) = 4B^2 \cdot \left(\frac{1}{2b_w} \cdot \text{tri}\left(\frac{f}{4b_w}\right)\right) = 2B^2\frac{1}{b_w} \cdot \text{tri}\left(\frac{f}{4b_w}\right)$$

Now multiply by the original constant $B = 2q\bar{I}$:

$$y(t) = B(n_1^2(t) - n_2^2(t)) \Rightarrow B = 2q\bar{I} \Rightarrow B^2 = 4q^2\bar{I}^2$$

So finally:

$$S_y(f) = 4q^2\bar{I}^2 \cdot 2b_w \cdot \text{tri}\left(\frac{f}{4b_w}\right)$$

Which produces the final expression:

$$S_y(f) = 8q^2\bar{I}^2 b_w \cdot \text{tri}\left(\frac{f}{4b_w}\right) \quad [A^4/Hz] \tag{A.7}$$

Now combining with the linear term calculated earlier we can get an expression for the transfer of shot noise through the DBHD system.

$$S_{\Delta P}(f) = 16q\bar{I}^3 + 8q^2\bar{I}^2 b_w \cdot \text{tri}\left(\frac{f}{4b_w}\right) \quad [A^4/Hz] \tag{A.8}$$

Looking at the result intuitively we find that there is a component of the noise that is a form a or flat bandwidth noise that arises from the linear noise component. The second term is a colored noise term whose slope changes as a function of the measurement bandwidth.

We start by considering further simplifications to understand how the equation can be analyzed. One aspect that I neglected earlier in the proof was the absolute value of the prefactor terms A and B. In the final expression both A and B get squared:

$$A^2 = 16q\bar{I}^3, \qquad B^2 \cdot b_w = 16q^2\bar{I}^2 \cdot b_w$$

We put experimental values to this model including a mean current of [$\bar{I} = 1$ mA] and electron charge as [$q = 1.6 \times 10^{-19}$ C]. We find that the because we are operating at a current (charge flow) that is much, much larger than the charge of an electron that the B term can be entirely neglected by over 6 orders of magnitude, even with a measurement bandwidth of [$b_w = 1$ GHz]. This should have been considered earlier in the proof. In single photon experiments this simplification might not work when the mean current is on the order of the electron charge.

Ultimately, it is a completely reasonable simplification to set:

$$B^2 \approx 0$$

A.4 Analysis

We thus wish the make the comparison to the PSD of the noise generated by the conventional balanced (ΔV) and dual balanced devices (ΔP). Here the shot noise power spectral density is given as follows:

$$S_{\Delta V}(f) = 4q\bar{I} \quad [A^2/Hz], \qquad S_{\Delta P}(f) = 16q\bar{I}^3 \quad [A^4/Hz]. \tag{A.9}$$

Here it should be noted that the PSD of the power difference case is not a direct square of the noise PSD of the voltage difference case. Rather the current is cubed and the units of the response are now proportional to the electrical power, squared.

A.4.1 Signal Model

To understand the magnitude of the shot noise when compared to the signal we first have to consider the power of the signal. I have defined the signal terms previously and will thus not

include the derivation in this proof. We assume the Faraday rotation signal electrical power k_i is proportional to the photocurrent as follows [2] :

$$k_{\Delta V} \propto \Delta\theta^2 \bar{I}^2 \quad [A^2] \qquad\qquad k^{\dagger}_{\Delta P} \propto \Delta\theta \bar{I}^2 \quad [A^2]$$

Conventional **Double Balanced**

Here we see the motivation for the problem. We knew that small signals of magnitude $<< 1$ would be greatly amplified if the $\Delta\theta$ term remained linear as is seen by the signal in the dual balanced case. We measured this experimentally and found the response slope to be correct however we found that the signal-to-noise ration (SNR) was much worse than expected.

In this it is important to note that the above expression are both given in units of power. However, it is only the conventional case where the noise PSD can be considered in these units. Because we are not considering what is fundamentally, a power signal the power spectral density of such a signal should be in units of power, squared. The resulting expression used for calculating the SNR of the dual balanced system should actually be:

$$k_{\Delta P} \propto \Delta\theta^2 \bar{I}^4 \quad [A^4]. \tag{A.10}$$

Here we lose the linear relationship to the Faraday rotation angle, that we have so desired. We should probably still see how the SNR reacts.

A.4.2 Signal To Noise Ratio (SNR)

SNR is defined as the ratio of the signal power P_s and the noise power P_n:

$$SNR = \frac{P_s}{P_n} = \frac{k_i}{S_i}.$$

I once again make the distinction that signal power is related to the square of the signal $P_s \propto s^2$, even if this leads to unconventional units like $[A^4]$. Knowing this statement we can define a minimum detectable polarization rotation as $SNR(\Delta\theta_{min}) = 1$.

[2] † represents that the units of the equation are not correct to represent power spectral density, and will be modified in the following section.

Conventional	**Double Balanced**
$SNR_{\Delta V}(\Delta\theta) = \frac{\Delta\theta^2 \bar{I}^2}{4q\bar{I}}$	$SNR_{\Delta P}(\Delta\theta) = \frac{\Delta\theta^2 \bar{I}^4}{16q\bar{I}^3}$
$\Delta\theta_{\min} = \sqrt{\frac{4q}{\bar{I}}}$	$\Delta\theta_{\min} = \sqrt{\frac{16q}{\bar{I}}}$

This concludes the proof, demonstrating that the sensitivities of the two systems are equal in magnitude. It was shown that taking the electrical power difference of optical signals increases the shot noise power by an amount equivalent to the increase in signal power, resulting in no net gain in sensitivity. ■